THE THERMAL EVOLUTION AND DYNAMICS OF PYROCLASTS AND PYROCLASTIC DENSITY CURRENTS

A Dissertation
Presented to
The Academic Faculty

By

Mary Catherine Benage

In Partial Fulfillment
of the Requirements for the Degree
Doctor of Philosophy in the
School of Earth and Atmospheric Sciences

Georgia Institute of Technology

August 2015

THE THERMAL EVOLUTION AND DYNAMICS OF PYROCLASTS AND PYROCLASTIC DENSITY CURRENTS

Approved by:

Dr. Josef Dufek, Advisor
School of Earth and Atmospheric Sciences
Georgia Institute of Technology

Dr. Zhigang Peng
School of Earth and Atmospheric Sciences
Georgia Institute of Technology

Dr. Christian Huber
School of Earth and Atmospheric Sciences
Georgia Institute of Technology

Dr. Heather Wright
Cascade Volcano Observatory
United States Geological Survey

Dr. Andrew Newman
School of Earth and Atmospheric Sciences
Georgia Institute of Technology

Date Approved: June 19, 2015

To my loved ones and the memory of Janet Bare

ACKNOWLEDGEMENTS

First, I would like to thank my advisor, Dr. Josef Dufek, for his support, encouragement, and guidance that enabled me to become a better scientist and an independent researcher. His advice, knowledge, patience, hard work, and the opportunities he provided me to be in the field are invaluable to me. Thank you to the Dufek group that has helped me throughout my PhD career, especially Ozge, Jenn, Cindy, Estep, Molly, Josh, Ryan, and Leah. A special thank you to Wim for being my second mentor and for his instrumental support and kind nudges. Thank you to Zach for the help with ArcMap even after he left and for his support throughout the years. Also, I am indebted to my dissertation committee who kindly agreed to review my work and have provided me feedback, advice, and support throughout my time here at Georgia Tech.

I would not have finished without the support and love of all my friends. Thank you especially to my beloved friends, Casey, Malia, Hallie, Angela, and Sami, though always far away, their support, encouragement, and love never wavered and gave me the confidence to keep pressing forward. Thank you to my Atlanta family, Keaton, Jessica, Nadia, Emily, Rebecca, Toby, Katie, John, and Colin, for making my time here full of laughter, friendship, and adventure.

Lastly, I would like to thank my parents for their unconditional love and support. I would not be here, have the opportunities I do, nor finish my degree without them. My parents have been my inspiration, role models, and my rock and I am forever grateful. Thank you to Becky, Drew, Jaime, and Lindsay for their support, love, and keeping me humble by always giving me a hard time in true sibling fashion.

Thank you to Georgia Tech and Earth and Atmospheric Sciences for the opportunity to pursue my research interests. The Department of Energy Computational Science Graduate Fellowship (DOE-CSGF) and the National Science Foundation Graduate Research Fellowship under Grant No DGE-1148903 supported this work.

TABLE OF CONTENTS

LIST OF TABLES

LIST OF FIGURES

LIST OF SYMBOLS AND ABBREVIATIONS

c_P	heat capacity
P	pressure
I	interphase momentum transfer
H	interphase heat transfer
h	heat transfer coefficient
g	gravity
T	temperature
$T_{g,o}$	glass transition temperature
k	thermal conductivity
σ	surface tension
q	heat flux
μ	viscosity
ε_g or α_g	volume fraction of gas
ε_p or α_p	volume fraction of particles
ρ	density
κ	thermal diffusivity
τ	stress tensor
δ_{ij}	Kronecker delta
BND	bubble number density
St	Stokes Number
Re	Reynolds Number
Ri	Richardson Number
Re_p	Reynolds Particle Number

Nu	Nusselt Number
PDC	pyroclastic density current
EEL	Eulerian-Eulerian-Lagrangian

SUMMARY

The thermal evolution of pyroclastic density currents (PDCs) is the result of entrainment of ambient air, particle concentration, and initial eruptive temperature, which all impact PDC dynamics and their hazards, such as runout distance. The associated hazards and opaqueness of PDCs make it impossible for in-situ entrainment efficiencies or concentration measurements that would provide critical information on the thermal evolution and physical processes of PDCs. The thermal evolution of explosive eruptive events such as volcanic plumes and pyroclastic density currents (PDCs) is reflected in the textures of the material they deposit. A multiscale model is developed to evaluate how the rinds of breadcrust bombs can be used as a unique thermometer to examine the thermal evolution of PDCs. The multiscale, integrated model examines how bubble growth, pyroclast cooling, and dynamics of PDC and projectile pyroclasts form unique pyroclast morphology. Rind development is examined as a function of transport regime (PDC and projectile), transport properties (initial current temperature and current density), and pyroclast properties (initial water content and radius). The model reveals that: 1) rinds of projectile pyroclasts are in general thicker and less vesicular than those of PDC pyroclasts; 2) as the initial current temperature decreases due to initial air entrainment, the rinds on PDC pyroclasts progressively increase in thickness; and 3) rind thickness increases with decreasing water concentration and decreasing clast radius. Therefore, the modeled pyroclast's morphology is dependent not only on initial water concentration but also on the cooling rate, which is determined by the transport regime.

The developed secondary thermal proxy is then applied to PDCs from the 2006 Tungurahua eruption to constrain the entrainment efficiency and thermal evolution of PDCs. A three-dimensional multiphase Eulerian-Eulerian-Lagrangian (EEL) model is coupled to topography and field data such as paleomagnetic data and rind thicknesses to study the entrainment efficiency and thus the thermal history of PDCs at Tungurahua volcano, Ecuador. The modeled results that are constrained with observations and thermal proxies demonstrate that 1) efficient entrainment of air to the upper portion of the current allows for rapid cooling, 2) the channelized pyroclastic density currents may have developed a stable bed load region that was inefficient at cooling and 3) the PDCs had temperatures of 600-800K in the bed load region but the upper portion of the currents cooled down to ambient temperatures. The results have shown that PDCs can be heterogeneous in particle concentration, temperature, and dynamics and match observations of PDCs down a volcano and the thermal proxies. Lastly, the entrainment efficiencies of PDCs increases with increasing PDC temperature and entrainment varies spatially and temporally. Therefore, the assumption of a well-mixed current with a single entrainment coefficient cannot fully solve the thermal evolution and dynamics of the PDC.

CHAPTER 1

INTRODUCTION

1.1 Introduction to Pyroclastic Density Currents

Pyroclastic density currents are volcanic gravity currents composed of hot magmatic gas, entrained ambient air, fragmented magma, and accidental lithics that propagate due to the difference in density between the gravity current and the ambient atmosphere. Pyroclastic density currents (PDCs) are one of the most dangerous local hazards from volcanic eruptions. Approximately fifty volcanoes erupt each year and many will produce PDCs that have the potential to harm nearby inhabitants [*Sigurdsson et al.*, 1999]. Since 1783, volcanic eruptions have caused 220,000 fatalities with 26.8% from pyroclastic density currents [*Tanguy et al.*, 1998]. In 1815, Tambora erupted in the East Indies and the PDCs that ensued killed 10,000 – 12,000 people [*Sigurdsson et al.*, 1999]. The 1883 eruption of Krakatau generated PDCs that killed approximately 1,000 people but significantly more were killed from the volcanic-generated tsunamis [*Carey et al.*, 1996; *Tanguy et al.*, 1998]. In 1902, Mount Pelee erupted and PDCs engulfed the city of St. Pierre, killing 28,000 people [*Lacroix*, 1904]. In 1930, the Merapi eruption killed ~1,400 people [*Van Bemmelen*, 1949] and the 1980 Mount St. Helens eruption killed 57 people [*Peterson*, 1988]. Although the fatalities from volcanic eruptions pale in comparison to those from other natural disasters, as population increases the probability for volcanic disasters increases. PDC hazard assessment and flow path prediction will thereby only increase in importance.

A better understanding of the complex physical processes of PDCs requires the integrative study of deposits, numerical models, and analog, scaled experiments and is

paramount to mitigating hazards of future PDC-producing eruptions. Hazard predictions are often based on numerical or analytical models whose inputs require inference from deposits and experiments due to our inability to observe the real-time internal dynamics of dangerous PDCs. Many factors are believed to affect the fluid dynamics of PDCs, such as particle concentration, air entrainment, interaction with topography, temperature, size of bed load region, degree of fluidization, substrate erosion and entrainment, and generation mechanism (e.g. column collapse, dome collapse, boiling over) [*Branney and Kokelaar*, 2002; *Burgisser and Bergantz*, 2002]. A variety of physical models (based on granular, turbulent, or fluidized flows) and experiments have been applied to elucidate the complex, unseen dynamics of PDCs. Additionally, the deposits of PDCs are a critical component to understanding PDCs processes, but provide an incomplete record of PDC processes. Deposits record the depositional conditions of the PDC that many believe only provide insight into the lower flow boundary rather than the entire current.

1.2 Depositional processes

Direct observations of sedimentation from PDCs is not possible, therefore interpretation of depositional processes has relied on observations of PDC transport and descriptions of PDC deposits [*Branney and Kokelaar*, 2002]. Early descriptions of eruptions and the observation of texturally distinct deposits gave rise to the definition of two types of currents representing end members in PDC transport and deposition, pyroclastic surges and pyroclastic flows. While the term pyroclastic density current is not dependent on the concentration of particles in the current, the terms surge and flow separate volcanic gravity currents into two distinct concentrations. A pyroclastic surge is described to have a particle concentration less than 1 vol%, transport particles in

suspended turbulent currents, and form planar, cross-bedded, or massive bedforms [*Wohletz and Sheridan*, 1979]. Pyroclastic flow refers to a current concentrated in particles that is thought to deposit more thick, massive (no structure) facies [*Sparks*, 1976; *Wilson and Houghton*, 2000]. It is well accepted that pyroclastic surge deposition is through progressive aggradation, which is incremental deposition from the base of the current [*Burgisser and Bergantz*, 2002]; however, the poor sorting and lack of stratification in massive deposits gave rise to two different depositional scenarios, progressive aggradation and en masse deposition [*Branney and Kokelaar*, 2002].

Whereas deposition from progressive aggradation is an incremental process, en masse is deposition when the entire, highly concentrated and coherent flow comes to rest [*Branney and Kokelaar*, 2002]. Early work suggested the massive and poorly sorted PDC deposits were the result of a density stratified pyroclastic flow with a higher particle concentration at the base that limited turbulence, traction, and sorting during deposition. The poorly sorted deposits were thought to be the result of progressive aggradation of particles from the base of a continuously depositing flow [*Fisher*, 1966]. Others explained the thick, poorly sorted deposits to be the actual flow structure right before it stopped en masse [*Sparks*, 1976; *Wilson*, 1984]. En masse deposition would allow insight into the internal structure of a PDC right before deposition. This would allow inferences of vertical concentration of particles within the PDC and insight into PDC dynamics from deposit structure.

However, evidence of variations in lithofacies, compositional changes in massive deposits, and welding characteristics suggest that PDCs progressively aggrade at the base of the current [*Branney and Kokelaar*, 1992; 1997], and supports the early hypothesis of

Fisher (1966) that these currents are density stratified and deposit incrementally. In most cases, a PDC deposit is not an image of the current but a record of the change in the basal part of the current with time. A progressively aggraded deposit only records the conditions of the flow at the flow boundary zone; therefore it is difficult to infer the particle concentration and transport dynamics of the overriding current. Interpretation of PDC dynamics based on deposits alone is further complicated by the unsteadiness of the current such that currents are not always depositional [*Branney and Kokelaar*, 2002]. Therefore, a complete understanding of the dynamics of the entire current relies on observations, experiments, and numerical models.

Pyroclastic density currents vary in velocity, concentration, temperature, and rheology in both space and time, and affects the depositional process at the flow-deposition boundary [*Branney and Kokelaar*, 2002]. Branney and Kokelaar provide an extensive memoir describing a variety of depositional processes and the associated facies of the resultant deposits. They further propose criteria for deposition versus non-deposition/erosion based on current steadiness and current uniformity. Current steadiness is taken from an Eulerian reference frame and describes variation in current parameters (example velocity, flux, composition, particle concentration, temperature) with time for a single point in space. Current uniformity is based on a Lagrangian reference frame and describes how current parameters vary over space with respect to a point that moves with the current. While a current might be close to steady at times, it is unlikely for a current to be uniform due to changes in slope, sedimentation, particle interaction, and entrainment of lithics or air along its flow path. These complicated, non-linear processes can give rise to different deposit lithofacies, geometries, and distributions. For example,

Branney and Kokelaar propose a current for which velocity increases in time at a fixed point (waxes) and velocity increases down current (accumulative) is likely to cause erosion or non-deposition. In contrast, a current that has velocity decrease with time (wanes) and velocity decrease down current (depletive) would be depositional and form a typical ignimbrite deposit. Thus determining current dynamics such as particle concentration, velocity, temperature, flux, or rheology from deposits is not straightforward. The coupling of experiments and models with deposits is critical to constraining current dynamics. In order to quantify the driving forces in the current, geologists conduct experiments and create numerical models constrained by observations and deposits [*Dufek et al.*, 2015].

1.3 Local Concentration and Forces

Experiments, theory, and numerical models have found that the local concentration of particles is a determining force in PDCs. Though currents likely exist with a continuous spectrum of particle concentrations, historical separation of the currents into dilute and concentrated regimes has separated models and experiments generally into the two end members. The models and experiments are also broken down into specific particle concentrations to separate out the driving physics of PDCs as the concentration of particles and turbulence determines the dominant momentum transfer in granular flows [*Savage*, 1998; *Iverson and Vallance*, 2001] .

For dilute PDCs, the fluid dynamics are approached through numerous gravity current experiments and theoretical studies [*Simpson and Britter*, 1979; *Huppert and Simpson*, 1980; *Bonnecaze et al.*, 1993; *Dade et al.*, 1994; *Hallworth et al.*, 1996]. For the dilute PDCs or pyroclastic surges, it is assumed that negligible particle-particle

interaction occurs and the currents are homogeneous in concentration due to the effects of turbulence [*Wohletz and Sheridan*, 1979; *Bursik and Woods*, 1996]. In this regime, the dominant force on particles is particle-gas drag (Figure 1), which can be analyzed by a non-dimensional number called the Stokes number. A Stokes number less than or equal to one means the particle is well coupled to the fluid [*Burgisser and Bergantz*, 2002; *Dufek and Bergantz*, 2007a; *Esposti Ongaro et al.*, 2008]. Pyroclastic surges (the dilute upper portion of a PDC) are turbulent currents that have the ability to entrain ambient air [*Dufek and Bergantz*, 2007a] and change the concentration, temperature, and dynamics of the current [*Bursik and Woods*, 1996; *Dufek and Bergantz*, 2007a].

Though dilute portions of a current can be turbulent, the more concentrated or dense portion of a current contains a significant amount of mass and momentum, therefore a different set of dynamics is assumed [*Iverson and Vallance*, 2001]. As the current becomes more concentrated, momentum transfer is assumed to be from particle-particle inelastic collisions (Figure 1). Each collision causes a loss of kinetic energy from particle deformation, thermal energy transfer, or particle breakage. At even higher concentrations, particle-particle friction and prolonged substrate contact (Figure 1) is important for loss of energy [*Dufek and Bergantz*, 2007a]. If the concentrated bed load region has a high amount of fines and low permeability, the interstitial gas can develop high pore pressure that can support the weight of particles and reduce friction, i.e. fluidize the flow [*Roche*, 2004; *Druitt et al.*, 2007] and can increase run-out distance [*Roche et al.*, 2010]. It has also been determined that the discrete nature of the granular bed-load may have large heterogeneities in stresses at the bed load region, which is currently not solved for in numerical models and can affect transport distance and

substrate erosion [*Estep and Dufek*, 2012]. The local concentration of particles, the non-linear interaction between particle settling and turbulence, and the distribution of particles within the flow affect the entire current dynamics.

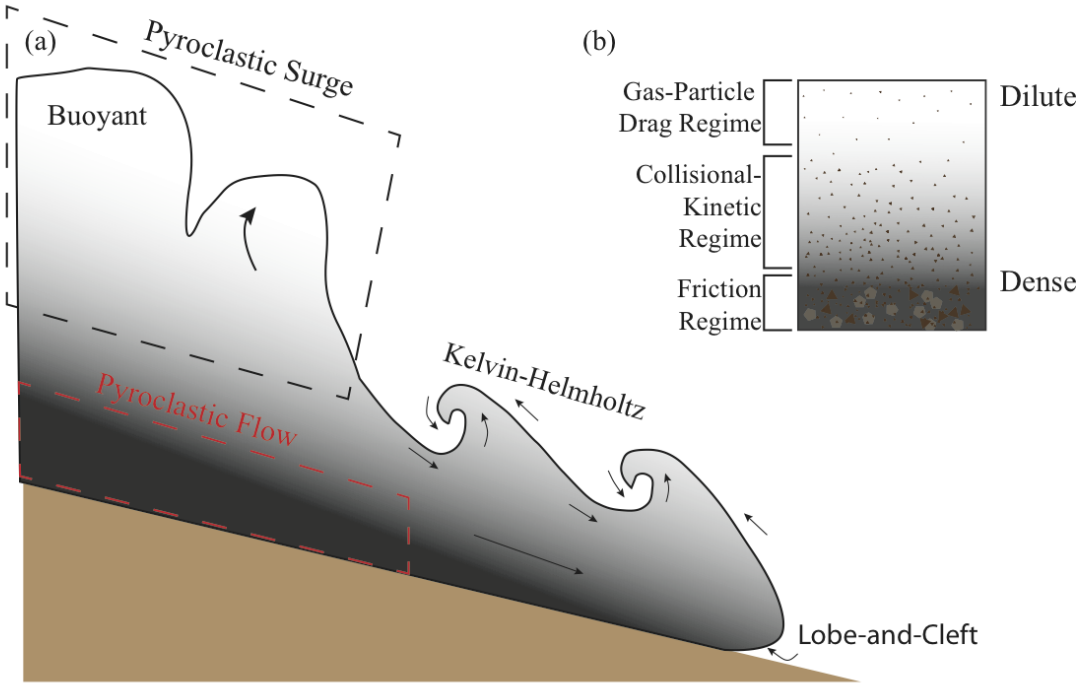

FIGURE 1: Pyroclastic Density Current Structure. (a) A cartoon of inferred internal structure of PDCs. The entrainment and cooling of the current is through the Kelvin-Helmholtz and Lobe-and-Cleft instabilities. The hypothesized particle concentration profiles is depicted with the color gradient (see (b) for more detail). The separate PDC end members, pyroclastic surge and pyroclastic flow, are outlined with dashed boxes. (b) The separation of different fluid mechanic regimes based on particle concentration. Figure adapted from *Dufek* [2016].

1.4 Entrainment and Thermal Evolution

Here we focus on the entrainment of ambient air and its control on the thermal evolution and thereby flow dynamics. The vertical concentration gradient in a PDC controls density stratification, which affects the entrainment of ambient air and the thermal evolution of the current. Although experiments, physics, and models give insight

into the general PDC structure and a vertical particle concentration gradient, the evolution of the gradient in PDCs is poorly constrained and remain controversial [*Sparks*, 1976; *Druitt*, 1998; *Branney and Kokelaar*, 2002]. A portion of the controversy resides in the debate that volcanic gravity currents occur as the two distinct end members, surge and flow, whereby a current does not have a continuous spectrum of particle concentration [*Wilson*, 1984; *Wilson and Houghton*, 2000; *Burgisser and Bergantz*, 2002]. However, models and field observations show that a single PDC is likely to have a range of particle concentration that vary in time and space [*Fisher*, 1966; 1983; *Valentine*, 1987; *Valentine and Wohletz*, 1989; *Neri and Macedonio*, 1996; *Druitt*, 1998; *Calder et al.*, 1999; *Fujii and Nakada*, 1999; *Burgisser and Bergantz*, 2002; *Douillet et al.*, 2013b; *Brand et al.*, 2014]. Through physical models, the gradient in particle concentration likely develops due to gravity (sedimentation) and suspension by turbulence of particles with Stokes number less than or equal to 1 [*Burgisser and Bergantz*, 2002; *Dufek and Bergantz*, 2007a]. These processes create a more concentrated base and a more dilute upper portion of the current (Figure 1) and are likely unsteady [*Fisher*, 1966]. The gradients of particle concentration are important as they influence other physical processes such as entrainment of ambient air, substrate erosion, and depositional processes [*Branney and Kokelaar*, 2002]. The entrainment of ambient air is an important physical process that is thought to affect the thermal evolution and dynamics of PDCs, such as the runout distance of the current.

Entrainment of ambient fluid (air) appears to occur through large scale eddies [*Turner*, 1986] via two instabilities of turbulence: the Kelvin-Helmholtz and Lobe and Cleft instabilities [*Dufek et al.*, 2015]. See Figure 1. Kelvin-Helmholtz instability occurs

when shear of the overriding fluid overcomes the stable density stratification of the current [*Dufek and Bergantz*, 2007a]. Lobe-and-Cleft instability is the result of friction at the base of the current allowing the nose of the current to overrun ambient air creating an unstable region of reversed buoyancy at the base of current [*Choux and Druitt*, 2002]. These complex non-linear phenomena are still not fully understood. In addition, turbulent mixing is a multiscale process that adds more complexity to the physics of this problem.

In order to understand the dynamics of a flow and the effects of ambient fluid entrainment into a current, gravity currents (in both water and gas) have been studied by numerous lab experiments and numerical models [*Hallworth et al.*, 1993; *Dade et al.*, 1994; *Hallworth et al.*, 1996; *Andrews*, 2014]. Gravity current experiments in a confined fluid flume with constant flow volume have shown that dilute currents can entrain ambient fluid in the head of the current through shear instabilities and by overriding the ambient fluid. In order to model the entrainment in these dilute gravity currents, a empirical constant entrainment coefficient based on a fraction of the surges velocity is assumed [*Turner*, 1986; *Dade et al.*, 1994]. The other method for modeling the entrainment of ambient fluid is through an empirical entrainment coefficient based on the Richardson number of the entire current [*Ellison and Turner*, 1959; *Bursik and Woods*, 1996].

However, very few studies have evaluated the effect a current with a temperature higher than the ambient fluid (or gas) has on entrainment efficiency and flow characteristics. PDCs are different from turbidity or granular flows due to their high temperatures and therefore the study of non-ambient currents and their entrainment efficiency is pertinent for PDCs. In an isothermal system, a turbulent gravity current

requires significant entrainment of ambient fluid in order to change the currents density [*Wells et al.*, 2010]. For high temperature PDCs, the entrained air is heated and can increase the current volume through adiabatic expansion, decrease particle concentration and current density, and eventually lead to buoyancy reversal affecting the runout distance of the current [*Bursik and Woods*, 1996; *Andrews*, 2014]. Through thermodynamic numerical and analytical models a dilute current that is supercritical and entrains ambient air would have a shorter run-out distance than a non-entraining current. [*Bursik and Woods*, 1996].

The entrainment efficiency of hot PDCs is not well known and traditionally the thermal evolution and PDC dynamics are inferred from deposit temperatures and observations. In recent years, Forward Looking Infrared Radiometer (FLIR) cameras have been used to record the relative temperature of an eruption and examine plume behavior [*Patrick*, 2007; *Steffke et al.*, 2010], but cannot penetrate all depths of a current or provide exact temperatures throughout the current. Direct measurements of deposits hours to days after an eruption are the most exact method to determine emplacement temperatures. For example, direct measurements at Soufriere Hills give pyroclastic density current emplacement temperatures between 638 – 913 K [*Cole et al.*, 2002] and measurement of the PDC deposits from the summer 1980 eruptions of Mount St. Helen range from 573 to 1003 K with near vent deposits emplaced at 1023 – 1123 K [*Banks and Hoblitt*, 1981]. However, direct measurements are done immediately after an eruption, which is not applicable to many current and historic eruptions. Paleomagnetic studies, where the acquired magnetization at temperature intervals is unblocked, can give ranges of depositional temperatures. A study of lithic and juvenile clasts from the 1883 Krakatau

eruption determined that the subaqueous pyroclastic density currents were deposited while still relatively hot, with an emplacement temperature around 748 – 823 K. This suggests that the PDC stayed as a coherent current upon entrance into the sea and had little entrainment of water and therefore little cooling [*Mandeville et al.*, 1994]. Thermoremanent demagnetization of juvenile and lithic clasts from PDC deposits at Tungurahua determined the current had hot juvenile pyroclasts [*Roperch et al.*, 2014; *Rader et al.*, 2015] but accidental lithic emplacement temperatures below 363 K suggesting the current was a warm current with hot juvenile pyroclasts [*Rader et al.*, 2015]. Another method to estimate the temperature of a pyroclastic density current is the presence and reflectance of charcoal [*Scott and Glasspool*, 2005]. However, none of these alone can describe the evolving temperature state of a current. This is where numerical thermal models coupled with deposits are vital to quantifying the thermal processes and entrainment efficiency of PDCs.

1.5 Overview of PDC Models

There are a variety of numerical models for the transport and dynamics of PDCs but generally the models can be broken down into concentration components. The three main categories are: 1) Box models for dilute currents, 2) Depth-average models for concentrated currents, and 3) multiphase models for continuous spectrum of concentration.

The dilute box model approach assumes a current is well mixed, dilute, and turbulent. Box models are commonly used for turbidity currents and were the first application of entrainment coefficients to study the effect of entrainment on dynamics such as runout distance or liftoff. Box models are a method to model a finite volume or

mass of a gravity current and are a simplified approach that models the currents as a "box". Many box models are based off scaling, experiments, and theoretical work of inviscid currents. A common assumption is to use the Froude number close to unity for the front velocity and solve for conservation of mass or volume [*Dade and Huppert*, 1995a; 1995b; *Dade*, 2003]. A box model that conserves thermal energy determined entrainment is a strong influence on runout distance of PDCs [*Bursik and Woods*, 1996]. Box models provide valuable insight into the dynamics of dilute turbulent currents but are not applicable for the more concentrated PDCs.

For a concentrated flow, a depth-averaged model is commonly employed. The models solve the average equations of motion for the flow height and the resulting bed shear stress based on rheology [*Iverson and Denlinger*, 2001]. A common assumption for these models is a coulomb friction rheology [*Iverson and Vallance*, 2001], but a plastic Bingham rheology has also been found to match deposits [*Kelfoun et al.*, 2009]. Additionally, some depth-averaged models solve for pore-pressure diffusion of a fluidized bed [*Iverson and Denlinger*, 2001]. Depth-averaged models have successfully modeled runout distance and are a powerful tool that couples models to topography to more effectively model PDCs [*Dufek et al.*, 2015].

In order to model the continuous concentration spectrum and flow transformation from dilute to dense or dense to dilute, multiphase models are needed. Multiphase models solve for separate dynamics based on different phases and concentrations through separate conservation equations for mass, momentum, and energy and closure assumptions. Multiphase models can account for turbulent interaction, concentrated collisions between particles, and frictional interaction [*Valentine and Wohletz*, 1989; *Neri*

and Macedonio, 1996; *Burgisser and Bergantz*, 2002; *Neri et al.*, 2007; *Dufek and Bergantz*, 2007a; 2007b; *Esposti Ongaro et al.*, 2008; 2012]. Multiphase models can be used to examine particle stratification, sorting, and air entrainment during PDC transport. However, one of the limiting factors for multiphase models compared to box model or depth-averaged models is that they are computationally expensive.

1.6 Multiphase Models

Multiphase models that are coupled with observations and deposits can quantify the driving forces in PDCs and improve our understanding of the unseen physical processes within the current. Multiphase models are based on first principle physics and model the non-linear dynamics of varying particle concentration, turbulence, and particle-particle interactions [*Raju and Meiburg*, 1995; *Burgisser and Bergantz*, 2002; *Dufek and Bergantz*, 2007a]. Much of the added physics to multiphase models come from fluid dynamics and granular flow theory. Multiphase models solve conservation of mass, energy, and momentum equations for each phase and the phases interact through drag and heat transfer. The thermal exchanges between hot gas, particles, and ambient air allows for an investigation of the thermal history of a PDC. For a dilute portion of the current, gas-particle drag is a driving force and the interaction of particles and gas can be evaluated through the Stokes number [*Burgisser and Bergantz*, 2002; *Dufek and Bergantz*, 2007a]. To solve the momentum transfer from particle-particle interaction, a similar kinetic theory for molecular collisions is applied to the particles [*Lun et al.*, 1984; *Dufek and Bergantz*, 2007a]. At more concentrated volumes, frictional stress is added to the kinetic and collisions stresses [*Syamlal et al.*, 1993; *Savage*, 1998; *Dufek and Bergantz*, 2007a]**.** The physics of the model allows the investigation of the feedback

between current velocity, bed shear stress, particle sorting/segregation, instabilities, and entrainment of ambient air.

A further addition to the multiphase model is the Lagrangian phase that allows the examination of a single particle transport history in the flow [*Dufek and Bergantz*, 2007b; *Dufek et al.*, 2009]. The Lagrangian equation of motion is derived from the Basset-Boussinesq-Oseen (BBO) equation to sum the various forces acting on a spherical particle [*Maxey and Riley*, 1983; *Burgisser and Bergantz*, 2002]. The change in particle velocity is from drag forces between particle and gas and particle-particle collisions and gravity. The momentum exchange between gas and particles depends on drag coefficient, which is a function of the particle Reynolds number. The particle Reynolds number is the ratio of fluid inertial forces to viscous forcing. Small particles with small drag response times are well coupled to the fluid through large drag forces. Large Stokes number particles do not follow fluid motion and therefore particle inertia dominates [*Dufek et al.*, 2015]. The Lagrangian phases allows quantification of the currents carrying capacity [*Dufek et al.*, 2009], the transition from dense to dilute [*Burgisser and Bergantz*, 2002], and can examine the thermal history of the particle and current.

1.7 Objectives

Due to the inability to measure the spatial and temporal variation in particle concentration, velocity, temperature, and particle sizes in a PDC in real-time and the inability of experiments to scale to all the necessary dynamics, multiphase models are essential to further our understanding of the internal physics and thermal evolution of pyroclastic density currents. Through concerted numerical models and deposit analysis a better understanding of PDCs dynamics is possible. My thesis research focuses on the

dynamics and thermal evolution of PDCs, specifically from the 2006 eruption of Tungurahua volcano, Ecuador. The first objective (Chapter 2, published in 2014) is analysis of a potential secondary thermal proxy, breadcrust/cauliflower bombs. Numerous cauliflower bombs are found at Tungurahua and other volcanoes. A breadcrust bomb is a pyroclast (diameter greater than 6.4 cm) that has a dense rind and a vesicular interior. The low-vesicularity of the rind is hypothesized to be a result of cooling [*Walker*, 1969; *Wright et al.*, 2007] but it has not been quantified.

Hypothesis: Breadcrust bombs with a rind developed on all sides are a result of the pyroclasts cooling history and the associated rind thickness is a proxy for the thermal and transport history of the pyroclast.

Questions: How are cauliflower/breadcrust bombs formed? Are they useful thermal proxies to better understand PDC dynamics?

Objective: To understand the flow dynamics and thermal history of pyroclasts that develop a non-vesicular rind and determine if breadcrust bombs can be used as secondary thermal proxies to resolve the temperature of a PDCs.

The second goal of my research (Chapter 3, manuscript in preparation for submission) is to constrain the entrainment efficiency and thermal state of the PDCs from the 2006 eruption of Tungurahua volcano. Field observations, thermal proxies, and multiphase models are applied to elucidate the current temperatures, dynamics, and entrainment efficiency.

Hypothesis: The PDCs at Tungurahua develop a dense bed load region and stable particle stratification during propagation that does not allow sufficient entrainment of ambient air and therefore the dense bed load region maintains a steady temperature.

Questions: How much and where does ambient air entrain in PDCs? Does entrainment alter dynamics? Does particle concentration affect entrainment efficiency?

Objective: To constrain the thermal history of the PDCs at Tungurahua using numerical models, thermoremanent magnetization, and secondary temperature proxies in order to further understand PDC dynamics and to quantify entrainment efficiency of 3D currents.

The thesis is concluded with a review of the chapter results and the direction for future research.

CHAPTER 2

TYING TEXTURES OF BREADCRUST BOMBS TO THEIR TRANSPORT REGIME AND COOLING HISTORY

Note: The results of this thesis chapter, presented here, have been published in Benage, M. C., Dufek, J., Degruyter, W., Geist, D., Harpp, K., & Rader, E. (2014). Tying textures of breadcrust bombs to their transport regime and cooling history. *Journal of Volcanology and Geothermal Research*, *274*, 92-107.
DOI:10.1016/j.jvolgeores.2014.02.005

2.1 Introduction

Pyroclastic density currents (PDCs) are some of the most destructive volcanic phenomena and understanding the many physical processes associated with these flows has proven difficult. Inherent opacity limitations and hazardous conditions have resulted in relatively poor constraints on flow dynamics, in particular on the thermal evolution. One mechanism that changes the thermal state of the current is entrainment of colder, ambient air [*Sparks*, 1986; *Bursik and Woods*, 1996]. The extent to which a current will entrain ambient air depends on the particle concentration and concentration gradient, particle size distribution, current shear, and current temperature [*Dufek and Bergantz*, 2007a]. These temporally and spatially variable conditions control the thermal evolution of a PDC, directly influence the total run out distance, and determine deposit characteristics [*Hallworth et al.*, 1993; *Bursik and Woods*, 1996; *Wilson and Houghton*, 2000; *Branney and Kokelaar*, 2002; *Clarke et al.*, 2002; *Neri et al.*, 2003; *Scott et al.*, 2008]. To improve our knowledge of the thermal evolution of PDCs, a better understanding and application of thermal proxies in these flows must be developed.

Hot pyroclasts that are deposited from explosive volcanic eruptions, either from ballistic trajectories or PDCs, have the potential to be used as thermal proxies. Each pyroclast has a unique transport path that samples a portion of the volcanic environment [*Kaminski and Jaupart*, 1997; *Vanderkluysen et al.*, 2012]. A breadcrust bomb (see Figure 2a) may be an especially useful thermal proxy due to its unique texture [*Wright et al.*, 2007; *Giachetti et al.*, 2010]. A breadcrust bomb is a pyroclast that has many surface cracks, a dense rind, and a vesicular interior. The surface cracks likely develop as a product of the continual growth of gas bubbles in the hot interior, which causes expansion of the clast and subsequent cracking of the brittle rind [*Walker*, 1969; *Wright et al.*, 2007]. Some surface cracks may also be from thermal contraction or from the stress of impact [*Wright et al.*, 2007]. Breadcrust bombs are found in deposits from basaltic to rhyolitic explosive eruptions, typically of Vulcanian style [*Walker*, 1982; *Morrissey and Mastin*, 2000; *Wright et al.*, 2007]. Some volcanoes that have generated breadcrust bombs are Montserrat [*Giachetti et al.*, 2010], Mayon [*Moore and Melson*, 1969], Cerro Galan [*Wright et al.*, 2011], Lascar [*Calder et al.*, 2000], Panum Dome [*Anderson et al.*, 1994], Cotopaxi [*Pistolesi et al.*, 2011], Guagua Pichincha [*Wright et al.*, 2007], Tungurahua [*Hall et al.*, 1999; *Le Pennec et al.*, 2008; *Douillet et al.*, 2013a], Vulcano [*Walker*, 1969], and Ngauruhoe [*Morrissey and Mastin*, 2000]. Breadcrust bombs are found as ballistically emplaced clasts in the crater or on the flank of volcanoes [*Wright et al.*, 2007; *Giachetti et al.*, 2010], but some are also found in PDC deposits (Figure 2b) kilometers away from the vent [*Hall et al.*, 1999; *Hall and Mothes*, 2008; *Giachetti et al.*, 2010; *Samaniego et al.*, 2011; *Douillet et al.*, 2013a]. The vesicularity gradient of a breadcrust bomb is hypothesized to be the result of syn-eruptive bubble

nucleation and growth, and the quick cooling of the bomb's edge during transport [*Walker*, 1969; 1982; *Giachetti et al.*, 2010].

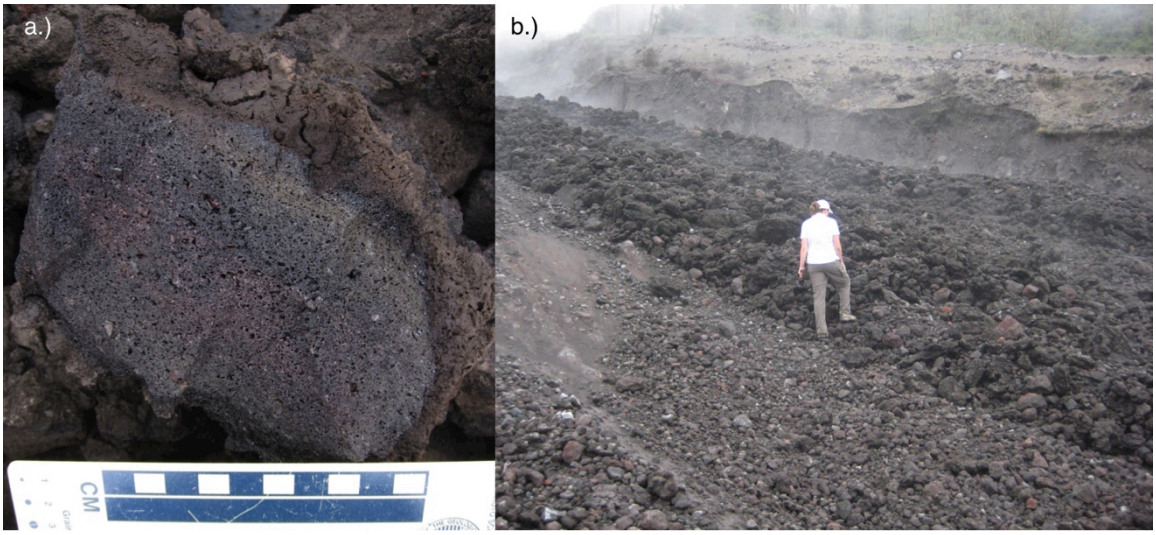

FIGURE 2: Breadcrust Bombs. a) An example of a breadcrust bomb with a dense rind from Tungurahua volcano, Ecuador. b.) PDC deposit of breadcrust bombs at Tungurahua volcano, Ecuador.

The radial distribution of bubble sizes in the clasts can provide insight into each bomb's thermal history. Bubbles grow through diffusion of volatiles into the bubble, where growth and expansion is limited by magmatic viscosity, which changes by orders of magnitude during cooling and solidification [*Sparks*, 1978; *Prousevitch et al.*, 1993; *Proussevitch and Sahagian*, 1996; *Blower et al.*, 2001]. Bubble nucleation in breadcrust bombs is thought to happen after fragmentation because of the small, isolated bubbles or the lack of bubbles in the rind [*Giachetti et al.*, 2010]. Immediately after eruption and fragmentation, breadcrust bombs are often above the glass transition temperature, which is the kinetic limit at which the material transitions from a viscous liquid to a glass [*Gottsmann et al.*, 2002; *Giordano et al.*, 2005]. As the clast cools, viscosity increases

and parts of the clast will cross the glass transition temperature. The increase in viscosity slows bubble growth, and bubble growth is terminated at high viscosities or when the temperature crosses the glass transition temperature. Therefore, the preserved radial bubble size distribution in the bomb provides a textural indicator of the relative timing between fragmentation and quenching [*Giachetti et al.*, 2010]. The radially dependent bubble size distribution within a given breadcrust bomb is proposed to be a function of bubble nucleation delay, bubble growth rate, cooling rate, and viscosity [*Walker*, 1969; 1982; *Hoblitt and Harmon*, 1993; *Giachetti et al.*, 2010]. Examining textural features of breadcrust bomb rinds after an eruption, when the depositional location of the pyroclast is known, provides an opportunity to retrace the thermal history of the pyroclast and of the eruption itself.

A combination of physical and mathematical models have been used to look at the cooling of pyroclasts that fell vertically [*Thomas and Sparks*, 1992], had ballistic trajectories [*Capaccioni and Cuccoli*, 2005; *Wright et al.*, 2007], or were entrained within an eruption column [*Kaminski and Jaupart*, 1997; *Hort and Gardner*, 2000]. Previous cooling models of falling pyroclasts have used convective and radiative heat transfer boundary conditions and conductive cooling in the clast interior [*Thomas and Sparks*, 1992]. More recent models expanded on this by adding a ballistic transport model with flight path and velocity to calculate the cooling of pyroclasts on a parabolic trajectory [*Capaccioni and Cuccoli*, 2005; *Wright et al.*, 2007]. *Wright et al.* (2007) compared known rind thicknesses of breadcrust bombs from field data to their cooling model to determine the time required for the rind to cool below the glass transition temperature. The time for the rind to cool below the glass transition temperature was used as an

approximation for rind formation time. The comparison suggests that rinds form relatively quickly (less than 45 seconds) after eruption and that some rinds on finely breadcrusted bombs form before impact.

A limited number of studies examine the interaction between cooling rates and syn-eruptive bubble growth. The model by *Hort and Gardner* (2000) on pumice cooling and bubble growth showed that water loss in pumice depends on the cooling rate. Pumice was almost completely degassed if the ratio of the cooling timescale to the degassing timescale was greater than approximately 50 [*Hort and Gardner*, 2000]. A pumice clast was less vesicular at the edge compared to its interior because of rapid cooling and viscous quenching on clast margins [*Kaminski and Jaupart*, 1997]. The impact of these timescales on textures stresses the need to couple numerical models of cooling and bubble growth to better interpret pyroclast textures. The pyroclast's transport path through the local environment will influence its final texture. All of these previous cooling models focus on either a parabolic path with no collisions or a collision-free fall through a uniform temperature environment. The examination of pyroclast cooling while entrained in a PDC has not been studied. No existing numerical model compares how different travel paths, such as ballistic versus PDC transport, affect a pyroclast's cooling history and, therefore, its texture.

In this study, a model of the thermal history and rind thickness of breadcrust bombs is developed to determine if path- and temperature-dependent textural information is imparted on multiple pyroclasts when transported either as projectiles in a buoyant eruption plume or within the body of a PDC. Throughout the text, pyroclasts entrained in PDCs will be referred to as PDC pyroclasts or PDC. The pyroclasts that are ballistically

ejected out of a buoyant plume will be referred to as projectile pyroclasts or projectile. To evaluate how the cooling history influences rind thickness, we build on the pyroclast cooling models presented in [*Thomas and Sparks*, 1992; *Capaccioni and Cuccoli*, 2005; *Wright et al.*, 2007] by adding a detailed transport system and a coupled model of cooling, viscosity, and bubble growth for individual pyroclasts. In each pyroclast, the radial change in bubble size allows for an explicit definition of rind thickness, where the rind contains the smallest bubbles. We also examine how varying the initial water concentration in the pyroclast affects the rind thickness. In this work, we focus on the end-member conditions of projectile pyroclasts ejected primarily through a cool, ambient atmosphere and pyroclasts transported in hot PDCs with variable entrainment histories. Here we do not focus on a specific eruption, but rather evaluate general trends in textural development associated with variable transport histories.

2.2 Methods

A coupled, multi-scale model is constructed to assess the effect transport path has on a breadcrust bomb's rind thickness and radial bubble size distribution. Development of the breadcrust bomb is modeled by combining three models of different scales that affect its evolution: 1) macro-scale: pyroclast transport in a multiphase current; 2) pyroclast-scale: surface heat loss and interior conductive cooling; and 3.) micro-scale: bubble growth. A model schematic is shown in Figure 3.

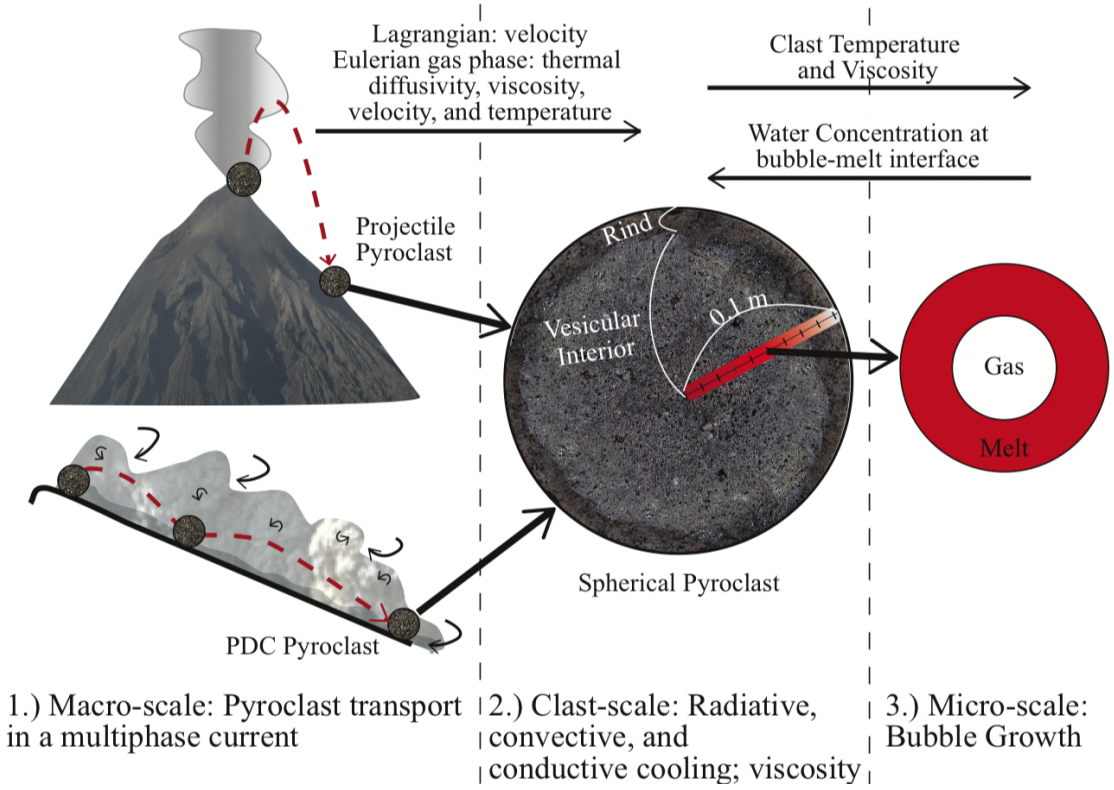

FIGURE 3: Model schematic (not to scale). 1.) Macro-scale: transport of pyroclasts as either projectile pyroclasts that erupt from a buoyant plume or as pyroclasts entrained in a PDC. 2.) Pyroclast-scale: the cooling of the isotropic, spherical clast from convective and radiative heat transfer to the surrounding environment and conductive cooling in the interior. The clast composition, water content (changing due to bubble growth) and temperature (changing due to cooling) are used to calculate viscosity and glass transition temperature. 3.) Micro-scale: The bubble growth model in which growth is limited by viscosity and diffusion, and is halted once the temperature is lower then the calculated glass transition temperature.

2.2.1. Macro-scale model

We apply a two-dimensional multiphase Eulerian-Eulerian-Lagrangian (EEL) model, modified from MFIX (Multiphase Flow with Interphase eXchanges [*Syamlal et al.*, 1993]), for volcanic currents [*Dufek and Bergantz*, 2007a] to simulate evolving particle concentration, thermal environment, physical dynamics, and the relative motion of clasts in two end-member currents: projectile pyroclasts from buoyant plumes and

pyroclasts entrained in PDCs. The EEL model has previously been used to model PDCs and their deposits [*Dufek and Bergantz*, 2007a; 2007b; *Dufek et al.*, 2009] and has been validated by comparison to direct numerical simulations (DNS) of gravity currents and experiments [*Dufek and Bergantz*, 2007a]. This multiphase model solves the continuum equations for mass, momentum, and energy, as well as related constitutive equations. For the PDC simulations, the resolution is 20 meters by 5 meters and the simulation domain is 8,070 meters by 2,000 meters, respectively along the horizontal and vertical axis. For the buoyant eruption with projectiles, the resolution is 20 meters by 20 meters and the simulation domain is 8,070 meters by 6,000 meters, respectively along the horizontal and vertical axis. For the two transport regimes, the same topography of a gentle, smooth slope is used (See Figure 4 and 5 for an example of the topographic profile).

The model uses two continuum (Eulerian) phases: a particle phase that represents the fine particles (particle diameter is 5.0×10^{-5} m for PDC simulations and 1.0×10^{-4} m for the buoyant plume simulations) and a gas phase. The particle diameters for PDC and buoyant plume ash are selected to have a Stokes number less than ~0.1 so that the fine particle phase will act as tracers of the fluid flow. The ash phase here approximates particles generated both from the initial fragmentation event as well as those generated by post-fragmentation conduit processes [*Dufek et al.*, 2013] and during transport [*Dufek and Manga*, 2008]. The particle and gas phases are two-way coupled by drag forces. The particle phase can interact with the gas phase, internally within its phase as a result of collisions or frictional interaction, and with the substrate. The collisional transfer of momentum is assumed to be binary and inelastic, and frictional stresses are assumed when the local volume fraction of particles exceeds close packing (here assumed to be

0.5 volume fraction) [*Dufek and Bergantz*, 2007a]. The conservation equations are solved by finite volume methods.

The governing equations are the conservation of mass for both phases,

$$\frac{\partial}{\partial t}\left(\alpha_g \rho_g\right) + \frac{\partial}{\partial x_i}\left(\alpha_g \rho_g u_{g,i}\right) = 0 \quad (1)$$

,

$$\frac{\partial}{\partial t}\left(\alpha_s \rho_s\right) + \frac{\partial}{\partial x_i}\left(\alpha_s \rho_s u_{s,i}\right) = 0 \quad (2)$$

,

the conservation of energy for both phases,

$$\alpha_g \rho_g c_{P,g}\left(\frac{\partial T_g}{\partial t} + u_{g,i}\frac{\partial T_g}{\partial x_i}\right) = \frac{\partial q_g}{\partial x_i} - \overline{H}_{gs} \quad (3)$$

,

$$\alpha_s \rho_s c_{P,s}\left(\frac{\partial T_s}{\partial t} + u_{s,i}\frac{\partial T_s}{\partial x_i}\right) = \frac{\partial q_s}{\partial x_i} + \overline{H}_{gs} \quad (4)$$

,

and the conservation of momentum for both phases,

$$\frac{\partial}{\partial t}\left(\alpha_g \rho_g u_{g,i}\right) + \frac{\partial}{\partial x_i}\left(\alpha_g \rho_g u_{g,i} u_{g,j}\right) = \frac{\partial P_g}{\partial x_i}\delta_{ij} + \frac{\partial \tau_{g,ij}}{\partial x_j} + I_i + \alpha_g \rho_g g_i \delta_{i2} \quad (5)$$

,

$$\frac{\partial}{\partial t}\left(\alpha_s \rho_s u_{s,i}\right) + \frac{\partial}{\partial x_i}\left(\alpha_s \rho_s u_{s,i} u_{s,j}\right) = \frac{\partial P_s}{\partial x_i}\delta_{ij} + \frac{\partial \tau_{s,ij}}{\partial x_j} - I_i + \alpha_s \rho_s g_i \delta_{i2} \quad (6)$$

.

See Table 1 for definition of symbols.

TABLE 1: Physical Properties*

Parameter	Description	Units
c_P	heat capacity	J/(kg·K)
P	pressure	Pa
I	interphase momentum transfer due to drag	Pa/m^3
T	temperature	K
u	velocity	m/s
q	heat flux	J/(m^2·s)
α	volume fraction	
τ	stress tensor	Pa
ρ	density	kg/m^3
g	gravity	m/s^2
δ_{ij}	Kronecker delta operator	
$\bar{H}$	mean interphase heat transfer	J/(m^3·s)
F_g	gas drag	m/s^2
F_s	particle-particle drag	m/s^2

*Subscripts s and g in the equations refer to the solid and gas phase, respectively. *i* and *j* refer to spatial dimensions (Dufek et al., 2009).

In addition to the two Eulerian phases, a Lagrangian phase is modeled to simulate the path and environment of a pyroclast during an eruption. Each individual Lagrangian particle is influenced by its local environment, which changes temporally and spatially. To track the particles, the equation of motion of each particle,

$$m_s \frac{du_{s,i}}{dt} = F_{g,i} + F_{s,i} + g\left(m_s - m_f\right)\delta_{i2}, \qquad (7)$$

is solved and is coupled to the Eulerian phases through the drag terms, where F_g is the drag force from the gas phase, F_s is the force from the collision of small particles, m_s is the mass of the particle, m_f is the mass of the gas displaced by the particle, and the *i* terms are index notation [*Maxey and Riley*, 1983; *Burgisser et al.*, 2005; *Dufek et al.*, 2009]. See Table 1 for further explanation of symbols. We examine 1,000 Lagrangian particles (i.e., pyroclasts) per simulation. The Lagrangian particles are the same size to facilitate comparison between simulations (acknowledging that real eruptions have complex distributions of large clasts). The EEL model calculates and records the environmental

information the Lagrangian particle experiences by interpolating the velocity, gas viscosity, gas heat capacity, gas density, and mean-temperature fields simulated through the Eulerian component to the specific particle location. To model breadcrust bomb morphology, these environmental conditions are used to calculate the cooling of the clast.

2.2.2 Clast-scale

2.2.2.1 Clast Cooling

The cooling of individual pyroclasts is modeled by solving for heat loss due to convective and radiative heat transfer at the surface and conductive cooling within the clast. Convective and radiative cooling is assumed to only take place at the surface and is not calculated radially within the clast. This assumption has been determined to be appropriate for cooling of pumiceous pyroclasts, where it was determined that interior convective and radiative heat transfer is negligible [*Thomas and Sparks*, 1992; *Tait et al.*, 1998; *Hort and Gardner*, 2000]. Clasts are assumed to be spherical, isotropic, uniform in composition, and constant in size (i.e. we assume no radial expansion due to bubble growth). We further assume the bulk material properties of the clasts are unaffected by bubble growth and keep the clast density, heat capacity, and thermal conductivity constant. Previous cooling models have also assumed a constant thermal diffusivity, as the interest is in the bulk cooling of the clast [*Hort and Gardner*, 2000; *Capaccioni and Cuccoli*, 2005; *Wright et al.*, 2007]. The spherically symmetric 1D heat equation is solved to model the spatial and temporal temperature change of the clast:

$$\rho_c c_{p_c} \frac{\partial T}{\partial t} = \frac{k_c}{r^2} \frac{\partial}{\partial r}\left(r^2 \frac{\partial T}{\partial r} \right) \qquad (8)$$

where ρ_c is clast density, $c_{p,c}$ is clast heat capacity, r is the radial coordinate, and k_c is thermal conductivity of the clast (See Table 2 for values). The heat equation is solved implicitly with finite difference methods (second order in space and time, unconditionally stable) [*Patankar*, 1980]. A 10^{-2} second timestep is used, and the 1D profile has a 10^{-4} meter resolution. The numerical solution for conduction and convection is verified against an analytical solution [*Eckert and Drake*, 1987; *Incropera and DeWitt*, 1996].

The surface cooling of the clast is modeled by calculating the heat flux. This allows the calculation of the clast temperature as a result of its interaction with the surrounding environment through forced convection and radiation. The surface heat flux is

$$k_c\left(\frac{\partial T}{\partial r}\right)_{r=R} = -q_R - q_c \quad , \tag{9}$$

where

$$q_R = \gamma\left(T_\infty^4 - T_{c_s}^4\right) \tag{10}$$

is the radiative heat flux, and

$$q_c = h\left(T_\infty - T_{c_s}\right) \tag{11}$$

is the convective heat flux, γ is black body emissivity, T_{cs} is surface temperature of the clast, T_∞ is the surrounding gas temperature, and h is the heat transfer coefficient. The heat transfer coefficient,

$$h = \frac{Nu\ k_g}{2r_c} \quad , \tag{12}$$

is calculated using the Nusselt number (Nu), the thermal conductivity of the surrounding gas (k_g), and the clast radius (r_c). The Nusselt number is determined from empirical

equations acquired from experiments on spheres [*Achenbach*, 1978] and small volcanic pyroclasts [*Stroberg et al.*, 2010]. The equations are dependent on the particle Reynolds number and Prandtl number. The particle Reynolds number,

$$\mathrm{Re}_p = \frac{2\left|\left(v_g - v_c\right)\right| r_c \rho_g}{\mu_g}, \qquad (13)$$

is the ratio of inertial forces to viscous forces and is determined by the velocity difference between the clast (v_c) and gas (v_g), clast radius (r_c), gas density (ρ_g), and gas viscosity (μ_g). The Prandtl number,

$$\mathrm{Pr} = \frac{c_{p_g}\mu_g}{k_g}, \qquad (14)$$

is the ratio of momentum diffusion to thermal diffusion and is dependent on the gas phase, where c_{Pg} is gas heat capacity, μ_g is gas viscosity, and k_g is gas thermal conductivity. For ambient air, Pr is ~ 0.71, which is the value used in the experiments on spheres to find the Nusselt number [*Achenbach*, 1978]. Our simulations include more diverse environments that result in Prandtl numbers varying from approximately 0.3 to 0.9. This variation of the Prandtl number results in a 30-40% difference in Nusselt numbers for the low particle Reynolds number ($\mathrm{Re_p} < 2.0 \times 10^5$) and we assume the deviation from Pr = 0.71 for the higher particle Reynolds numbers is similar in magnitude.

For low particle Reynolds number ($\mathrm{Re_p} < 2.0 \times 10^5$),

$$Nu = 2 + x\,\mathrm{Re}_p^{1/2}\,\mathrm{Pr}^{1/3}, \qquad (15)$$

where x=ρ_c [(2.2 ± 0.3) x 10^{-4}] + (0.31 ± 0.04), and ρ_c is the density of the volcanic clast [*Stroberg et al.*, 2010]. For mid-range particle Reynolds number 2.0 x $10^5 \leq \mathrm{Re_p} \leq$ 4.0 x 10^5,

$$Nu = 473.94 \log\left(\mathrm{Re}_p\right) - 5436.4 \quad (16)$$

Equation (16) is from a fit of the data of *Achenbach* (1978). For high particle Reynolds number 4.0 x $10^5 < \mathrm{Re_p} <$ 5.0 x 10^6,

$$Nu = 430 + a_1 \mathrm{Re}_p + b_1 \mathrm{Re}_p^2 + c_1 \mathrm{Re}_p^3, \quad (17)$$

where a_1 = 5 x 10^{-4}; b_1 = 0.25 x 10^{-9}; c_1 = -3.1 x 10^{-17} [*Achenbach*, 1978]. There is an error reported in *Achenbach* (1978) for a_1; see Appendix A for further details.

2.2.2.2 Clast Viscosity

The melt viscosity is calculated at each grid point along the 1D radial profile of the pyroclast with the *Giordano et al.* (2008) viscosity model. For the input composition, we use whole rock composition of TUNG-PS-48A scoria bomb (See Appendix C) from Tungurahua volcano [*Samaniego et al.*, 2011] and vary initial water concentration. The viscosity profile of individual pyroclasts varies throughout the simulation as a result of the changing temperature from cooling and changing water concentration from bubble growth. Vesicularity and crystal content also influence the absolute viscosity [*Kaminski and Jaupart*, 1997; *Llewellin and Manga*, 2005; *Caricchi et al.*, 2007]. The presence of crystals increases the viscosity, which restricts bubble growth. To incorporate the effect that fine-grained crystals (i.e., microlites) have on viscosity, the Einstein-Roscoe correlation is applied. The Einstein-Roscoe correlation is,

$$\mu_{m+c} = \mu_m \left(1 - R\phi\right)^{-2.5}, \quad (18)$$

where μ_m is the melt viscosity calculated by the *Giordano et al.* (2008) model, R=1.67, ϕ is the volume fraction of crystals, and μ_{m+c} is the new viscosity. This correlation has been found to be consistent with crystal volume fractions less than or equal to 30% [*Dobran*, 2001]. In all the models, crystal volume fraction is assumed to be 30%, which is a reasonable value for breadcrust bombs [*Burgisser et al.*, 2010; *Giachetti et al.*, 2010; *Samaniego et al.*, 2011].

The viscosity model enables the calculation of physical properties that are dependent on melt composition, temperature, and viscosity. One such property is the glass transition temperature, T_g [*Giordano et al.*, 2008]. The glass transition temperature is the transition of melt from a relaxed viscous liquid to an unrelaxed glass. It depends on composition and thermal history of the material [*Gottsmann et al.*, 2002; *Giordano et al.*, 2005]. The glass transition temperature is higher with faster cooling rates and with decreasing water concentrations [*Giordano et al.*, 2005]. As many rinds are glassy and non-vesicular, the glass transition is an important property for rind formation and is coupled with our clast- and micro-scale model. If the clast temperature drops below the calculated glass transition temperature, the bubble growth is terminated and the bubble is frozen in place. The glass transition temperature is calculated in the model as the temperature at which the specific melt composition would have a viscosity of 10^{12} Pa·s [*Giordano et al.*, 2008]. The assumption is that the melt has a relaxation timescale of ~15 minutes and a cooling rate of ~ 10 K/min. Traditionally, the glass transition viscosity is treated as independent of composition and is found to be around 10^{12} Pa·s for cooling rates on the order of several K/min [*Gottsmann et al.*, 2002; *Giordano et al.*, 2005].

2.2.3. Micro-scale (Bubble Growth)

The calculation of bubble growth within a viscous melt [*Prousevitch et al.*, 1993] is used to model the rind thickness of the breadcrust bomb. Bubble growth is calculated radially along the 1D profile of the pyroclast. Radially, all the bubbles start with the same size and the same porosity of ~ 10^{-7} %. Using the final radial bubble size distribution, we define the interior boundary of the rind as the point at which the spatial gradient of bubble size is maximized.

The *Prousevitch et al.* (1993) bubble growth model is isothermal, and water diffusivity and viscosity are held constant. To modify this bubble growth model, the changing temperature and viscosity of the melt calculated on the clast-scale model is coupled to the bubble growth model. We assume the melt surrounding the bubble is in thermal equilibrium with the temperature of the clast-scale model. The water concentration at the bubble-melt boundary is used to calculate the viscosity, as the viscous resistance to bubble growth is strongly controlled by the melt nearest the bubble [*Blower et al.*, 2001]. The bubble growth model accounts for growth due to the changing volatile concentration profile, the bubble growth resistance from high viscosities, the changing pressure of the bubble (ambient pressure, surface tension, and dynamic pressure), changes in saturation concentration at the bubble-melt interface, and the growing bubble radius. Bubble growth is most affected by the diffusion rate, viscosity of the melt, surface tension, initial water concentration, ambient pressure, and bubble separation [*Prousevitch et al.*, 1993]. We do not consider coalescence, multiple nucleation events, ripening, or irregular spacing of bubbles. We tested our model with

results from *Prousevitch et al.* (1993) and [*Forestier-Coste et al.*, 2012] and find good agreement.

In the model, the bubbles are each surrounded by a finite volume of melt that is closely packed in a polygonal matrix (see *Prousevitch et al.* (1993) for further explanation). For the bubbles to grow, the initial bubble radius must be greater than a critical radius,

$$R_{cr} = \frac{2\sigma}{\frac{c_o^2}{K_h} - p_m}. \qquad (19)$$

See Table 2 for explanation of symbols and the corresponding values. This results in a critical radius of 0.071 μm. For all simulations, the initial bubble radius is 0.3 μm with a bubble number density of 10^{10} m^{-3} [*Hurwitz and Navon*, 1994]. The maximum size a bubble can grow,

$$R_{final} = R_o \left[\frac{\rho_m}{\rho_g} \frac{S_o^3 - R_o^3}{R_o^3} \left(c_o - \left(K_h p_m \right)^{1/2} \right) + \frac{2\sigma}{R_o p_m} + 1 \right]^{1/3}, \qquad (20)$$

is calculated *a priori* based on the initial bubble radius, shell radius, pressure, and density, as well as constant conditions in Table 2. Equations 19 and 20 are from *Prousevitch et al.* (1993). If bubble number density is increased, R_{final} and the time for complete bubble growth will decrease (Prousevitch et al., 1993), which will result in smaller rinds. With this bubble growth model, we can examine how bubble growth is restricted as a result of an increase in viscosity from the cooling of the pyroclast. This allows us to calculate rind thickness and examine its correlation with a pyroclast's cooling history.

TABLE 2: Clast and Bubble Properties*

Parameter	Symbol	Value	Units	Reference
		Pyroclast Parameters		
density	ρ_c	2400	kg/m^3	
heat capacity	c_{Pc}	1095	$J/(kg \cdot K)$	[*Bacon*, 1977]
thermal conductivity	k_c	1.5	$W/(m \cdot K)$	[*Clauser and Huenges*, 1995]
radius	r	0.1	m	
initial temperature	T_o	1200	K	
thermal diffusivity	κ_c	5.71×10^{-7}	m^2/s	[*Whittington et al.*, 2009]
black body emissivity	γ	5.67×10^{-8}	$W/(m^2 \cdot K^4)$	
initial glass transition temperature	$T_{g,o}$	818	K	[*Giordano et al.*, 2008]‡
		Bubble Parameters		
melt pressure	p_m	10^5	Pa	
surface tension	σ	0.35	N/m	[*Walker and Mullins*, 1981]
diffusivity H_2O	D	9.0×10^{-11}	m^2/s	[*Behrens et al.*, 2004]
Henry's constant	K_h	10^{-11}	Pa^{-1}	[*Burnham*, 1975]
initial conc. H_2O	c_o	0.01		
Bubble Number Density	BND	10^{10}	m^{-3}	[*Hurwitz and Navon*, 1994]
initial bubble pressure	P_o	10^5	Pa	
initial bubble radius	R_o	0.3	μm	
a priori final bubble radius	R_{final}	1420	μm	
critical bubble radius	R_{cr}	0.071	μm	
initial shell radius	S_o	288	μm	
melt density	ρ_m	2400	kg/m^3	

*All values are constant except for the initial values c, R, S, T, Tg, and P, which will change with time.

‡ The initial glass temperature is from Giordano et al. (2008) viscosity model using the composition of a bomb from Tungurahua (Samaniego et al., 2010) and an initial water concentration of 1 wt. %.

2.2.4. Model Compilation

Our simulations explore a range of initial conditions with this multi-scale, coupled model (Table 3) to determine whether transport and thermal history influence the rind thickness. At one-second intervals, the macro-scale model records the velocity of each Lagrangian particle (1,000 per simulation) and the interpolated Eulerian gas information

around the particle (such as velocity, viscosity, heat capacity, density, and mean-temperature) in a data file. The clast- and pore-scale models are run concurrently, reading in the data from the 1,000 Lagrangian particles that are tracked in each macro-scale simulation. The heat loss of each particle is determined with the clast-scale model. Viscosity and glass transition temperature are calculated using the *Giordano et al.* (2008) model with the temporally changing temperature from the clast-scale model and the temporally changing water concentration profile from the pore-scale model. The temperature, glass transition temperature, and viscosity are applied to the pore-scale model for bubble growth. If the temperature is less than the glass transition temperature, the bubble growth model is stopped at that radial position and the bubble is frozen in place. Each calculation simulates 450 seconds of eruptive activity.

We first assess how particle trajectories and transport regimes (i.e., projectile vs. PDC entrained) influence the thermal history and rind development in the clast. To more easily discern how path affects the rind thickness, most of the initial conditions are kept the same for each simulation and transport occurs in two primary scenarios, a buoyant eruptive plume with projectile bombs or a PDC propagating laterally with entrained bombs. Run conditions pertinent to each simulation, PDC 1 – 6 and Projectile 1 – 6, are included in Table 3. The initial gas temperature for each transport regime is varied between 900 K, 700 K, and 500 K to approximate conditions in a flow with variable near-vent air entrainment. Variable initial entrainment of cold air cools the current and is likely an important component for PDCs that generate breadcrust bombs [*Rader et al.*, 2015]. For each initial gas temperature, a dense and dilute current for each transport regime is analyzed (see Table 3). The dense and dilute terms are used in relation to our

simulations and are not meant as actual end member values for all eruptions. Runs 1 and 2 have the highest initial gas temperature and have a dense (Run 1) and dilute (Run 2) end member. The naming scheme is the same for both the Projectile and PDC runs. An increase in run number correlates to a decrease in initial gas temperature.

TABLE 3: Initial Conditions of Simulations

Model Name	**Initial Gas Temp. (K)**	**Volume Fraction of Gas**	**Exit Velocity (m/s)**	**Pyroclast Radius (cm)**	**Initial H_2O (wt. %)**
		Transport & Thermal History			
Projectile 1	900	0.998	139.0	10.0	1.0
Projectile 2	900	0.9999	399.4	10.0	1.0
Projectile 3	700	0.998	137.5	10.0	1.0
Projectile 4	700	0.9999	368.2	10.0	1.0
Projectile 5	500	0.998	135.0	10.0	1.0
Projectile 6	500	0.9999	326.8	10.0	1.0
PDC 1	900	0.6	20.0	10.0	1.0
PDC 2	900	0.8	20.0	10.0	1.0
PDC 3	700	0.6	20.0	10.0	1.0
PDC 4	700	0.8	20.0	10.0	1.0
PDC 5	500	0.6	20.0	10.0	1.0
PDC 6	500	0.8	20.0	10.0	1.0
		Initial Water			
Projectile 4a	700	0.9999	368.2	10.0	0.8
Projectile 4b	700	0.9999	368.2	10.0	0.9
Projectile 4c	700	0.9999	368.2	10.0	1.25
Projectile 4d	700	0.9999	368.2	10.0	1.5
Projectile 4e	700	0.9999	368.2	10.0	2.0
Projectile 4f	700	0.9999	368.2	10.0	3.0
PDC 3a	700	0.6	20.0	10.0	0.8
PDC 3b	700	0.6	20.0	10.0	0.9
PDC 3c	700	0.6	20.0	10.0	1.25
PDC 3d	700	0.6	20.0	10.0	1.5
PDC 3e	700	0.6	20.0	10.0	2.0
PDC 3f	700	0.6	20.0	10.0	3.0

TABLE 3 CONTINUED

		Pyroclast Size			
Projectile 7	700	0.9999	368.2	2.5	1.0
Projectile 8	700	0.9999	368.2	5.0	1.0
Projectile 9	700	0.9999	368.2	50.0	1.0
PDC 7	700	0.6	20.0	2.5	1.0
PDC 8	700	0.6	20.0	5.0	1.0
PDC 9	700	0.6	20.0	50.0	1.0

The varying density of the buoyant plumes is coupled to the initial ejection velocities. The initial ejection velocity of the current is based on the assumption that the flow is choked at the vent, and we assume a bomb's initial velocity is the same as the current. The exit velocities for the buoyant eruption with projectiles range from ~135-400 m/s and ejection angles are random. The PDC eruptions all start with an initial pyroclast and gas velocity of 20 m/s. In the first 5 seconds of the simulation, only the continuum model is run to allow the PDC to propagate down the slope; after 5 seconds the Lagrangian particles start to be introduced in both the interior of the current and slightly above the current. This is done to give pyroclasts an opportunity to distribute throughout the current. We assume a small background wind field (2 m/s) after deposition, to simulate post-depositional cooling. All 1,000 Lagrangian pyroclasts per simulation have an initial magmatic temperature of 1200 K, a radius of 10 cm (a bomb radius is > 3.2 cm), and a density of 2400 kg/m^3. For the pyroclast-scale, the material properties of the clasts are held constant (see Table 2), and 1 wt. % H_2O is used as the initial water content for the viscosity and bubble growth model. The pore-scale model has the same initial bubble values for all the simulations (see Table 2 for a list of the constant and initial values). We hold constant initial bubble conditions and many of the clast properties in

order to focus on how transport regime and transport properties influence rind thickness and breadcrust bomb morphology.

After thermal history is assessed, we investigate how water content and clast size affect the rind thickness. To determine how initial water concentration influences the rind thickness, all initial parameters and transport histories for Projectile 4 and PDC 3 are the same and only initial water concentration is varied from 0.8, 0.9, 1.0, 1.27, 2.0 and 3.0 wt. % H_2O (see section *Initial Water* in Table 3). For the clast size variation study, all initial parameters are the same as model runs Projectile 4 and PDC 3, except the pyroclasts within the macro- and clast-scale models now vary in radius size from 2.5 cm to 50 cm (see section *Pyroclast Size* in Table 3). This will cause different transport paths because of variations in size, and will cause different cooling regimes owing to new conductive cooling length scales and heat transfer coefficients.

2.3 Results

The multiphase simulations predict textural and cooling differences in pyroclasts due to different transport paths. Here we discuss separately three issues: 1) the distinct paths experienced by particles under each condition; 2) the role of transport path and thermal environment on the cooling profiles experienced in the different scenarios; and 3) radial bubble variations and rind thicknesses that are preserved in deposited clasts.

2.3.1 Transport History (Macro-Scale Results)

Particles in the multiphase simulations travel along distinct paths that result in different cooling histories and rind thicknesses. For the buoyant plume eruptions, projectiles mostly travel through cooler ambient air. The pyroclasts exit the hot eruption column within seconds and the remainder of the simulation time experience

environments close to that of ambient air (Figure 4). The denser, low velocity plume eruptions (Projectile 1, 3, and 5) eject clasts that travel a shorter distance by approximately 2 km than those erupted from dilute, high velocity plumes (Projectile 2, 4, and 6). The pyroclast transport time, $\tau_{transport}$, for Projectile 1, 3, and 5 (dense plume eruption) is on average 20 seconds and for Projectile 2, 4, and 6 (dilute plume eruption) is 33 seconds. $\tau_{transport}$ is the time the particle is moving and includes the time the particle is in flight and the time it saltates along the ground until it comes to a stop. Some of the pyroclasts do not follow a parabolic trajectory (Figure 4c) but rather have trajectories that deviate slightly from these parabolic paths as a result of drag between fine particles within the column and recirculating wind currents that develop as the plume ascends. The trajectories of the projectiles are similar to trajectories observed by *Vanderkluysen et al.,* (2012).

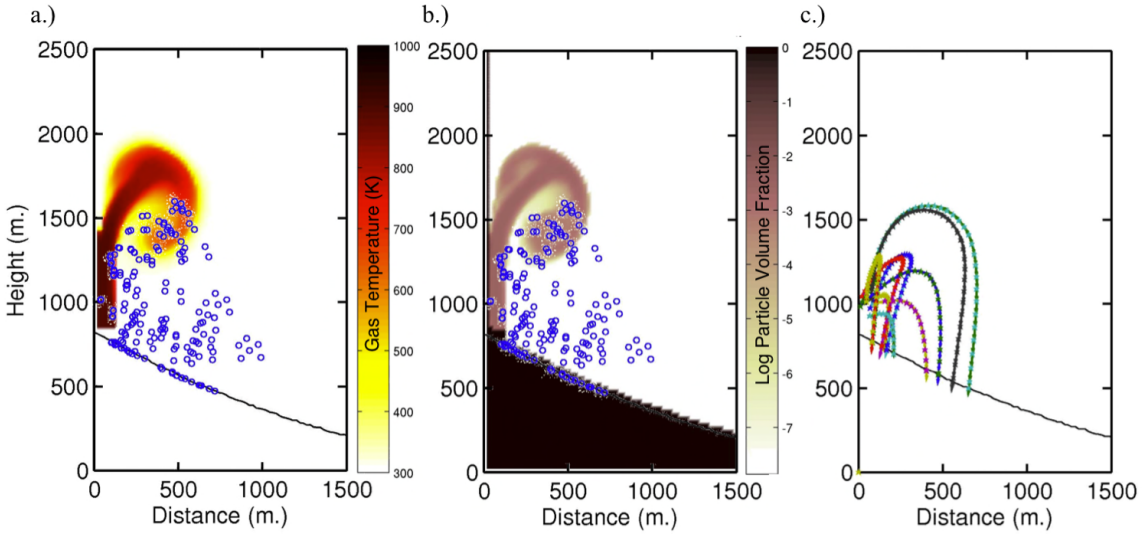

FIGURE 4: Projectile 1 model snapshot (not showing total simulation area). a.) Gas temperature contour of the dense Projectile 1 model at 18 seconds. The initial gas temperature is 900 K. The blue circles are the Lagrangian particles at 18 seconds. The buoyant plume entrains ambient air and cools along the outer edges. As the figure depicts, the projectiles travel mostly through ambient air. b.) Contour of the volume fraction of particles on a log scale at 18 seconds and blue circles are the same Lagrangian

particles. c.) The complete trajectory path of 10 Lagrangian particles. Note the non-parabolic trajectory for some of the particles.

The model of PDC results in pyroclasts that travel for longer durations in hot environments compared to projectile pyroclasts. The variation of initial current density results in different run out distances for the large clasts. The pyroclasts in the dense currents (PDC 1, 3, and 5) travel about 1 km further than the pyroclasts in the dilute currents (PDC 2, 4, and 6). For the majority of their transport, the large pyroclasts travel by saltation and through frictional interaction with the body of the current, primarily in the hot, dense bed load region. The bed load region stays the hottest and has the largest volume fraction of particles (Figure 5). The average $\tau_{transport}$ of the pyroclasts in the dense currents (PDC 1, 3, and 5) is 61 seconds and 26 seconds for the dilute currents (PDC 2, 4, and 6).

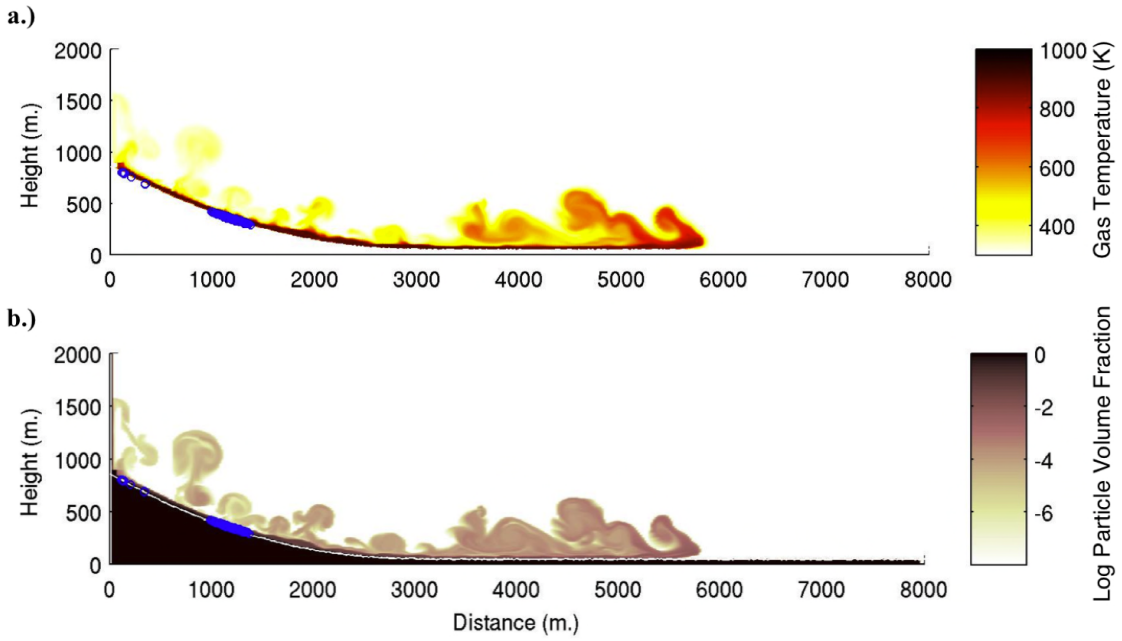

FIGURE 5: PDC 1 model snapshot (not showing total simulation area). Lagrangian particles are blue circles. a.) Gas temperature contour for PDC 1 at 68 seconds. The initial gas temperature is 900 K. Note the cooling of the current by entrainment of ambient air at the top of the current. The bed load region of the current still stays reasonably hot (700-

900 K) and is where the larger particles (Lagrangian) are located. b.) Particle volume fraction contour in log scale that depicts higher volume fraction of particles located in the bed load region.

2.3.2 Pyroclast Cooling History (Clast-Scale Results)

The large thermal gradients between the clast and the atmosphere immediately after eruption lead to rapid cooling at the surface of the clast. This is particularly true for the clasts following projectile trajectories. In the first 60 seconds, the surfaces of the clasts rapidly cool (Figure 6) and in general cool more efficiently in buoyant plume simulations. Here we compare the clast temperature to the initial temperature (relative temperature). At 60 seconds, all 3,000 projectile pyroclasts in Figure 6a cool to a relative temperature of 55-77%, with an average relative temperature of 70%. The clasts that travel dominantly in the core of the plume (and typically land closer to the vent) cool more slowly than those following lower angle trajectories. The lower angle trajectories travel for longer times, deposit furthest from the vent, and the majority of their travel is in the cooler, ambient atmosphere. These clasts have larger particle Reynolds numbers and therefore higher heat transfer coefficients. The surface temperature kink in Figure 6a (around 40-45 seconds) is the result of higher conductive heat flux within the clast compared to the overall surface heat flux. This causes the surface of the clast to heat up again and happens after deposition. Clasts entrained in PDCs typically have more similar transport paths and less variation in their surface temperature than the projectile clasts. An increase in surface temperature variation and cooling corresponds with a decrease in the initial PDC gas temperature (Figure 6b). At 60 seconds, the clast surfaces of PDC 1 (900 K initial gas temperature) cool to 85% relative temperature. PDC 3 (700 K initial gas temperature) clast surfaces cool on average to ~82% relative temperature and PDC 5

clasts (500 K initial gas temperature) cool to ~79% relative temperature. PDC 5 does have more variation in surface cooling, covering the entire range of 66-87% relative temperature.

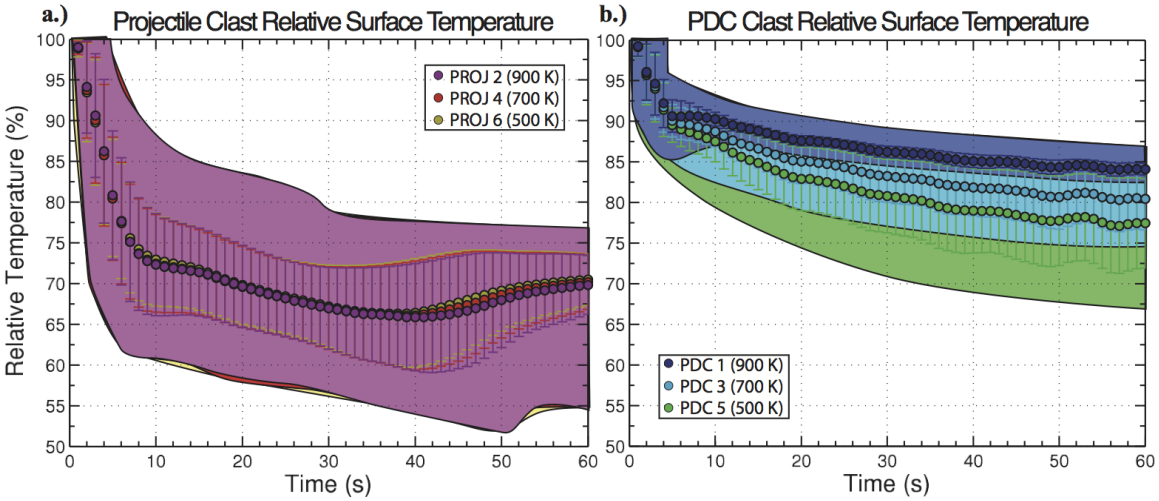

FIGURE 6: Relative surface temperature of pyroclasts. The relative surface temperature is the surface temperature of a pyroclast divided by its initial temperature of 1200 K. A relative surface temperature of 65 % means the surface has cooled to 780 K. The shaded polygon is the relative temperature area covered by the 1,000 particles per simulation for the first 60 seconds of cooling. The circles are the average of all 1,000 particles at each 1-second interval. The error bars are the standard deviation of the average at each 1-second interval. a.) Relative pyroclast surface temperature for the projectile simulations, Projectile 2, 4, and 6. All the projectile pyroclasts experience similar cooling histories, despite varying the initial gas temperature (shown in parentheses in the legend). The kink in the average temperature is the result of surface heat flux being less than the conductive heat flux inside the clast. This occurs after deposition. b.) Relative pyroclast surface temperature for the PDC simulations, PDC 1, 3, and 5. PDC 1 (initial gas temperature = 900 K) has the least variability and smallest amount of cooling for the surface of the clast. As the initial gas temperature decreases (or there is greater entrainment of ambient air), there is more variability in surface temperatures and greater cooling. PDC 5 (initial gas temperature = 500 K) has the greatest amount of surface cooling (~ 67-87% by 60 seconds). Even at the lower initial gas temperatures, the PDC pyroclasts do not cool as much as the projectile pyroclasts in the first 60 seconds.

Another useful comparison is the time it takes to cool the pyroclast 200 K throughout specific radial segments of the clast, specifically at the surface and the rind-

interior boundary. Although arbitrary, the timescale associated with a 200 K decrease in temperature encompasses the initial fast cooling rates as well as the more gradual temperature changes with diminished thermal gradients. The average cooling times for the projectiles are shorter than the average cooling times for the PDCs. The projectiles' cooling times change with initial density of the current. The dense plumes (Projectile 1, 3, and 5) cool more slowly than the dilute plumes (Projectile 2, 4, and 6). The dilute plume pyroclasts cool more quickly because a dilute current has a higher initial velocity under the choked flow assumption. Higher velocities result in higher particle Reynolds numbers and therefore greater heat transfer. The changes in initial gas temperature make less of a difference on the cooling times (Table 4). For the projectiles, the average cooling rate for the rind to cool 200 K ranges from 400 - 520 K/min. For 10 mm in from the edge of the clast, the average cooling rate is greater than 50 K/min. The time it takes to cool the temperature by 200 K for the PDC pyroclasts varies more with initial gas temperature than with initial current density (Table 4). The average rate to cool the rind 200 K ranges from 80 - 330 K/min, with the rate increasing with decreasing initial gas temperature (or greater initial air entrainment). For 10 mm in from the surface of the clast, the average cooling rate is greater than 30 K/min.

TABLE 4: Rind Thickness and Timescales

Model	Initial Gas Temp. (K)	Rind* Thick-ness (mm)	$\tau_{transport}$* (s)	τ_{rind}* (s)	τ_{Tg}* (s)	Cool* Surface 200 K (s)	Cool* Rind 200 K (s)	Cool* Outer 10 mm 200 K (s)
				Projectile Pyroclasts				
1	900	2.27 ± 0.46	20.80 ± 7.71	28.00 ± 18.02	129.01 ± 49.67	11.61 ± 11.76	27.92 ± 21.07	214.79 ± 29.55
2	900	3.11 ± 0.46	34.62 ± 11.58	21.44 ± 4.23	95.06 ± 48.24	5.86 ± 2.46	29.63 ± 9.99	182.93 ± 17.22
3	700	2.47 ± 0.33	20.25 ± 7.51	27.85 ± 8.68	133.48 ± 25.55	9.46 ± 3.29	31.72 ± 10.49	211.39 ± 10.86
4	700	3.16 ± 0.42	32.45 ± 10.81	22.12 ± 4.70	105.16 ± 45.88	5.40 ± 2.17	27.18 ± 9.30	185.27 ± 15.11
5	500	2.64 ± 0.26	19.49 ± 6.93	29.40 ± 8.76	139.34 ± 16.20	8.05 ± 2.44	32.00 ± 9.64	210.28 ± 7.67
6	500	3.14 ± 0.37	31.35 ± 10.37	23.33 ± 5.10	113.22 ± 42.95	5.24 ± 1.91	28.75 ± 7.43	188.54 ± 12.98
				PDC Pyroclasts				
1	900	1.24 ± 0.22	61.99 ± 20.90	122.14 ± 15.44	290.62 ± 40.16	78.58 ± 19.66	137.90 ± 14.49	368.83 ± 26.77
2	900	1.17 ± 0.23	26.64 ± 14.48	91.34 ± 14.12	216.56 ± 44.53	90.21 ± 8.70	106.17 ± 14.40	317.15 ± 31.06
3	700	1.95 ± 0.17	61.98 ± 19.20	39.11 ± 7.51	199.72 ± 12.62	18.24 ± 4.94	49.87 ± 9.80	268.51 ± 4.68
4	700	1.96 ± 0.19	26.63 ± 15.30	55.26 ± 5.27	178.08 ± 17.39	22.40 ± 8.75	68.31 ± 10.12	258.99 ± 7.34
5	500	2.24 ± 0.13	60.38 ± 21.41	28.65 ± 7.19	115.56 ± 29.79	12.36 ± 3.37	38.20 ± 9.62	213.93 ± 9.21
6	500	2.29 ± 0.17	26.88 ± 14.97	35.22 ± 8.74	148.89 ± 4.16	11.36 ± 5.24	46.01 ± 13.10	226.87 ± 4.34

*Values are the average result for the 1,000 pyroclasts (Lagrangian particles) per model. The smaller font number after '±' is the standard deviation of the average.

2.3.3 Rind Thickness and Bubble Growth

2.3.3.1 Thermal History

The variation in the thermal history of the pyroclast affects its final rind thickness. For the simulations with projectiles, there is little variation in rind thickness with varying

initial gas temperature and more variation as a result of initial current density (Figure 7 and Table 4). The projectiles from the dilute (faster velocity) eruptions, Projectile 2, 4, and 6, have an average rind thickness of 3.11 – 3.16 mm over the 900 – 500 K erupting gas temperature range. The dense (lower velocity) buoyant plumes, Projectile 1, 3, and 5, have pyroclasts with more variation in the average rind thickness, 2.27 – 2.64 mm, over the 900 – 500 K gas temperature range. The pyroclasts entrained in the PDC simulations have rinds that are sensitive to the initial gas temperature but not to the initial current density (Figure 7 and Table 4). At an initial gas temperature of 900 K, the PDC pyroclasts develop rind thicknesses that are on average 1.17 and 1.24 mm for the dilute and dense currents, respectively. As the initial gas temperature decreases (or there is greater air entrainment), the rind thickness on the pyroclasts increases. For both projectile and PDC pyroclasts, the distribution in rind thickness narrows as the initial erupting gas temperature decreases (Figure 7 d, e, and f).

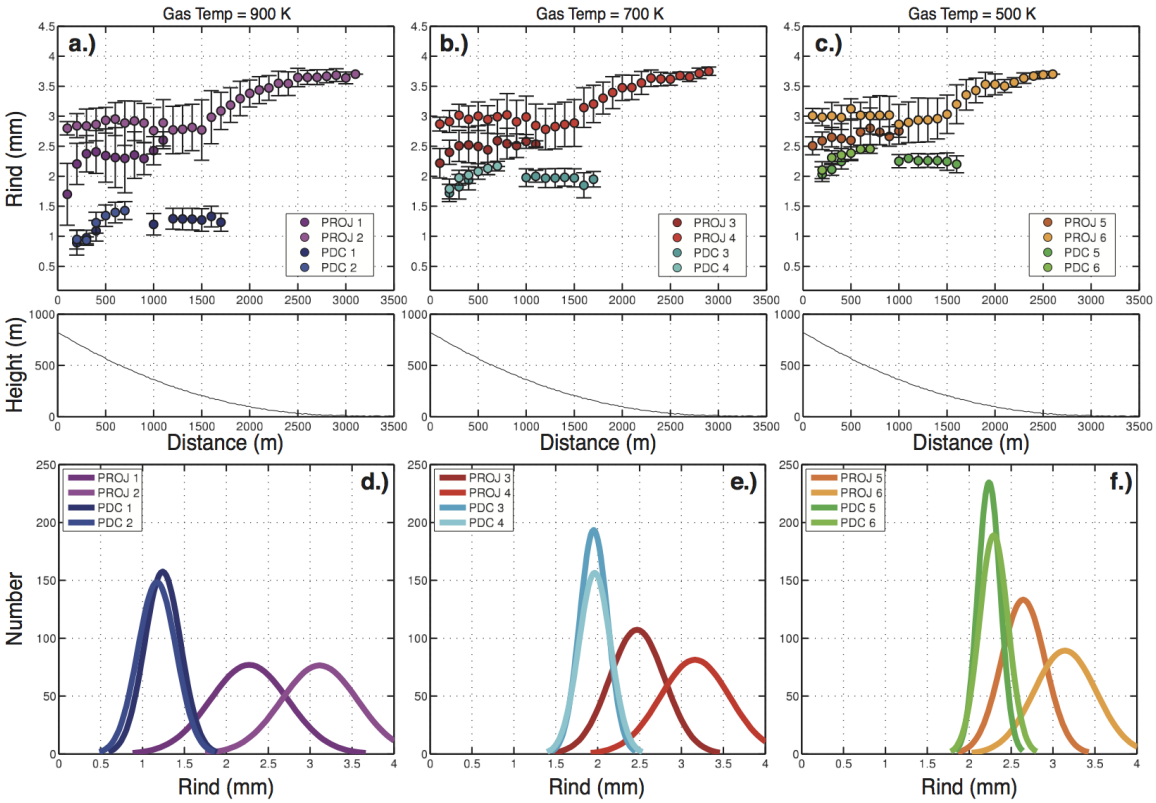

FIGURE 7: Rind Thickness. a-c.) Binned averages of rind thickness with depositional distance away from the vent for each initial gas temperature (900 K, 700 K, and 500 K). All pyroclasts start with a uniform initial temperature of 1200 Kelvin and 1.0 wt. % H_2O. Each point is an average of all particles within the 100-meter horizontal distance bin and the error bars are the standard deviation of all rind thicknesses in that particular bin. The bottom portion of the figure is the topographic profile for the simulation. As gas temperature decreases (greater initial entrainment of air), there is less difference between the rind thickness of projectiles and PDC pyroclasts. Also note the pyroclasts in the dense PDCs travel further than the pyroclasts in the dilute PDCs. The dilute, higher velocity projectile pyroclasts travel the furthest horizontal distance and have the largest rinds. The kink in the projectile rind distribution is an effect of ejection angle. Before the kink, the particles are mostly ejected at higher angles and have lower particle Reynolds and Nusselt numbers than the particles after the kink. d-f.) Distribution of rind thickness for each simulation. Initial gas temperature decreases from left to right. As the initial gas temperature decreases (or as entrainment of air increases), the distribution in rind thickness narrows for all simulations. The distribution of rind thickness illustrates how the rinds of PDC pyroclasts approach similar thicknesses to the rinds of projectile pyroclasts for the 500 K case. It also shows that the initial PDC current density made little difference in rind thickness, but initial current density did affect the rind thickness for the projectile pyroclasts.

The rinds on the projectile and PDC pyroclasts also differ in bubble size. The projectile pyroclasts with the thickest rinds have exceptionally small bubbles (bubble radius < 10 μm) near the clast edge and increase in bubble size towards the rind-interior boundary (Figure 8a). The smallest rinds (PDC runs with initial gas temperature of 900 K) have the largest bubbles at the clast edge. Rind thickness and minimum bubbles sizes are correlated; the thickest rind has the smallest bubbles at the edge. The PDC pyroclasts generally have larger bubbles at the edge of the clast than projectile pyroclasts. The minimum bubble radius for the PDC pyroclasts is greater than 10 μm. However, at equivalent rind thicknesses (where rind thicknesses of PDC and projectile clasts intersect in Figure 7 e-f), the PDC and projectile pyroclasts can have similar minimum bubble sizes in the rind. This only occurs for PDC runs with initial gas temperatures less than or equal to 700 K. The radial bubble profiles for the PDC pyroclasts show a distinct trend with decreasing initial gas temperature. As the current temperature decreases, the rind increases in thickness and the bubbles at the edge of the clast decrease in size (Figure 8b).

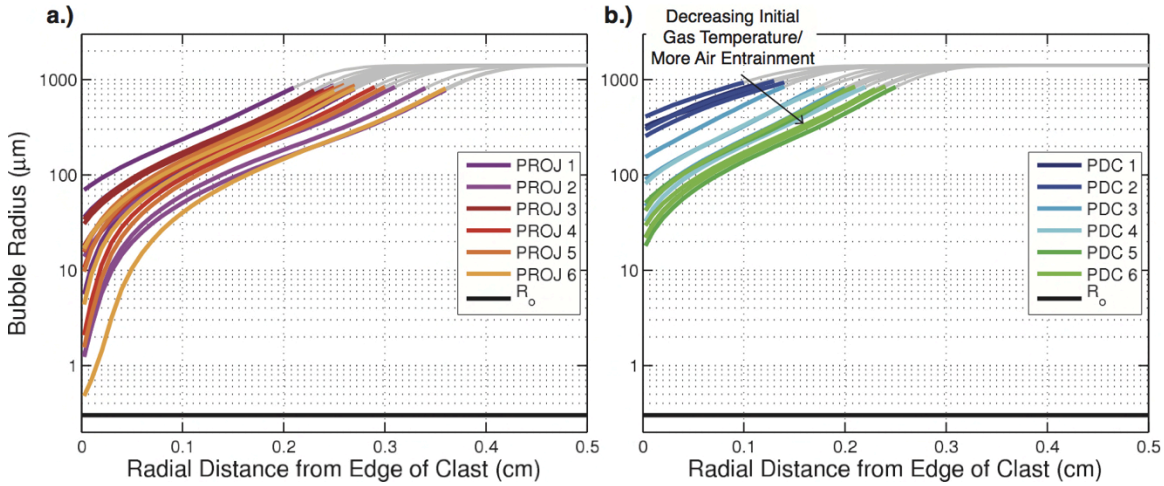

FIGURE 8: Bubble radius profiles at clast edge. A small fraction of the particles from each model are plotted. The colored lines are the rinds calculated for the clast. The gray lines show the rest of the bubble sizes in the interior of the clast, which grow to a

predetermined size and coalescence is not taken into account. R_o is the initial bubble radius. a.) Bubble radius profiles for the outer 5 mm of the clast for the buoyant plume models. The projectile pyroclasts have a greater size range of bubbles in the rind than the PDC pyroclasts but show no correlation with the initial gas temperature. Some of the projectile pyroclasts have bubbles at the outer edge of the rind that are quickly restricted from growing and therefore close to the size of R_o. b.) Bubble radius profiles for the PDC pyroclast models. The pyroclasts can have bubble sizes that are at least an order magnitude larger than the projectile pyroclasts at the very edge (~0.5 mm). The bubble radius profile within the rind of the PDC pyroclasts shows a distinct trend with initial gas temperature, where the bubble sizes at the edge decrease with decreasing initial gas temperature. The bubble sizes and rind thicknesses of PDC pyroclasts is correlated with the surrounding gas temperature.

The radial distribution of bubble sizes in the pyroclasts can also be compared using porosity. The final bubble size, R, and shell of melt around the bubble, S, allows the calculation of porosity at each radial point in the clast using $(R^3/S^3)\cdot 100$. The bubble geometry is closely packed cells that each contains a bubble in the middle and a finite volume of melt surrounding the bubble (Prousevitch et al., 1993). The interior of the bomb will have a final porosity of nearly 100 %, because the bubble grows to the equilibrium value determined by Henry's law of water solubility in magmas. At ambient pressure and the initial bubble conditions in Table 2, Henry's law gives a final porosity of 99 % (e.g., [*Prousevitch et al.*, 1993; *Koyaguchi*, 2005]). The bulk interior porosities are an overestimate since the bubbles are allowed to grow to the final equilibrium state at atmospheric pressure, which does not occur in nature. For example, Wright et al. (2007) has bulk interior porosities between 32 – 71 % and Burgisser et al. (2010) has vesicularities in the core between 8 – 44 % for Soufriere Hills. However, estimates of porosity with this model should be accurate in the rind where the distance between bubbles is more pronounced and the spherical shell assumption more robust.

To compare the rind porosities, average rind porosity for each clast is calculated using all the individual bubble porosities in the rind. The PDC runs with an initial gas temperature of 900 K have average rind porosities of 75 – 95 %. The remaining PDC and projectile clasts have average rind porosities between 20 – 65 %. The porosity decreases with increasing rind thickness for the PDC and projectile pyroclasts (Figure 9). The minimum porosity in the rind or the porosity at the edge of the clast for the PDC runs with an initial gas temperature of 900 K is between 30 – 90 %. The PDC pyroclasts with initial gas temperature of 700 K have minimum porosities less than 20 % and the PDC pyroclasts with an initial gas temperature of 500 K have minimum porosities less than 5 %. All the projectile pyroclasts have minimum porosities less than 20 % and also decrease to 0 % with decreasing initial gas temperature. At equivalent rind thickness, the projectile pyroclasts have similar minimum porosity to PDC pyroclasts, when the initial gas temperature of the PDC is less than or equal to 700 K. There is more overlap in rind thickness and minimum porosity for the PDC and projectile pyroclasts when the projectiles are from the dense buoyant plume (i.e. Projectile 3 and 5).

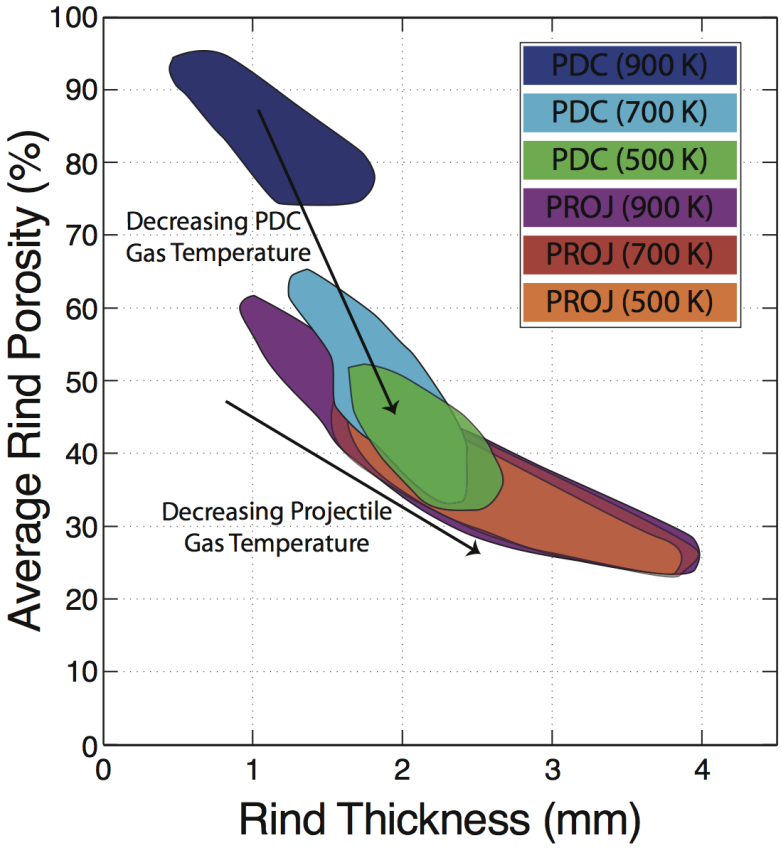

FIGURE 9: Average porosity in the rind. Porosity is calculated with the final bubble and shell radius, $(R^3/S^3)\cdot 100$, at 450 seconds. The average rind porosity is the average of all individual bubble porosities in the rind. As initial gas temperature decreases, the rind thickness increases and the average rind porosity decreases for the PDC pyroclasts. The projectile pyroclasts decrease slightly in average rind porosity with decreasing initial gas temperature. The projectile pyroclasts have the thickest and least vesicular rinds. If there is significant entrainment initially into the PDC, the rind thicknesses and porosities of PDC pyroclasts begin to collapse onto the projectile pyroclast region.

The cooling history of the pyroclast affects the amount of time it takes to restrict the growth of bubbles within the rind. We define, τ_{rind}, as the characteristic timescale for the bubble at the rind-interior boundary to reach 99% of its final, restricted size. It is a timescale that is used to quantify the time it takes the low-vesicular rinds to form. Viscous effects in the micro-scale model restrict and terminate bubble growth. The time it takes the melt surrounding the bubble at the rind-interior boundary to cross the calculated glass transition temperature is defined as τ_{Tg}. For all the pyroclasts, τ_{rind} is 2 – 5 times

faster than τ_{Tg}. The calculated glass transition temperature using *Giordano et al.* (2008) is based on a slower cooling rate, 10 K/min, than the cooling rates the modeled rinds experience, which exceed 80 K/min. The timescales for the projectile pyroclasts are correlated with initial current density and relatively poorly correlated with the initial gas temperature. The PDC pyroclasts' τ_{rind} and τ_{Tg} are correlated with initial gas temperature and poorly correlated with current density (Table 4), similar to the rind thickness results.

2.3.3.2 Rind Thickness due to Water Concentration

The initial water concentration and transport path of pyroclasts have a first order impact on rind thickness (Figure 10). For both PDC 3f and Projectile 4f, the highest water concentration of 3.0 wt. % in the molten pyroclast results in the thinnest rinds with an average thickness of 0.42 mm and 1.14 mm, respectively. The lowest initial water concentration of 0.8 wt. % in the molten pyroclast results in the largest rinds with an average rind thickness of 2.53 mm for PDC 3a pyroclasts and 3.87 mm for Projectile 4a pyroclasts (Figure 10). Around 0.5 wt. % dense bombs form because the bubbles are unable to grow. As initial water is increased the rind thickness decreases and rind porosity increases along the same trend in Figure 10. The threshold for when a dense bomb or a vesicular bomb with no rind forms depends on the initial bubble conditions and bomb composition. Transport regime is a factor in rind thickness for all water concentrations. For the lowest initial water concentration, there is relative change of 34.63% in rind thickness between the PDC and projectile pyroclasts and for the highest initial water concentration there is a relative change of 63.16% in rind thickness between the two transport paths.

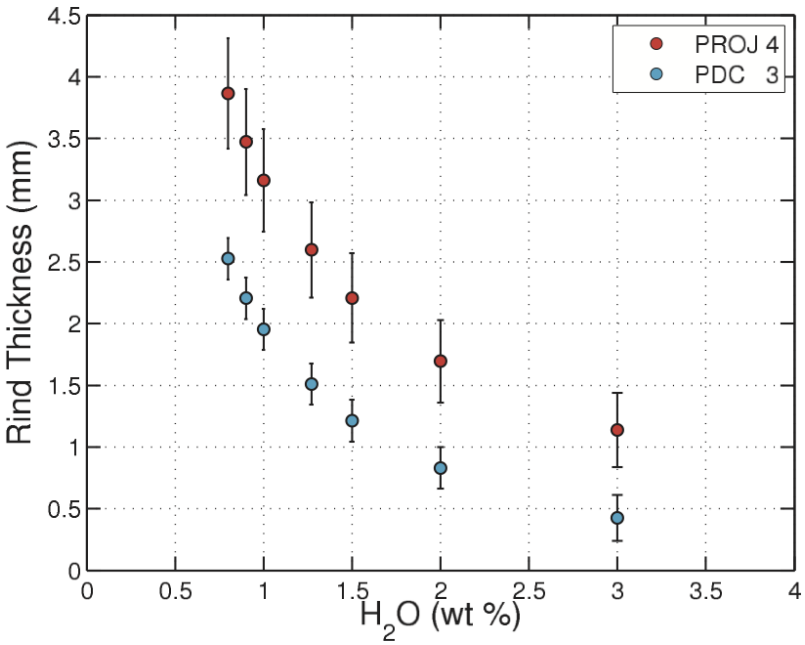

FIGURE 10: Rind thickness dependence on initial water and transport path. The comparison uses the thermal history of 1,000 particles in the Projectile 4 and PDC 3 simulations, but the initial water concentration is varied. The initial gas temperature is 700 K for these models. Each point is the average rind thickness of 1,000 particles and the error bar is the standard deviation for those particles. As initial water concentration is increased, the resultant rind thickness decreases. In the figure, focusing on a rind with a thickness of roughly 1.25 mm shows that the thickness is the result of a PDC pyroclast with 1.5 wt. % H_2O or a projectile pyroclast with 3 wt. % H_2O, thus illustrating how rind thickness is dependent on both water concentration and transport path.

In addition to variations in rind thickness based on initial water concentration, there is also a difference in the radial bubble size distributions within the rind. The minimum bubble radii in the rind are at the very edge of the clast. For Projectile 4a (0.8 wt. % H_2O), the minimum bubble radius in the rind varies from 0.34 – 17 μm and the minimum bubble radius in the rinds of Projectile 4f (3.0 wt. % H_2O) pyroclasts varies from 17 – 450 μm. For the pyroclasts of PDC 3a (0.8 wt. % H_2O), the minimum bubble radius in the rind varies from 2.3 – 72 μm, and for PDC 3f the minimum bubble radius varies from 390 – 1,360 μm. For both PDC and projectile pyroclasts, the 3.0 wt. % H_2O rinds have a larger average bubble size than the 0.8 wt. % H_2O rinds.

2.3.3.3 Rind Thickness due to Clast Radius

The simulations with varying clast radii result in different particle Reynolds numbers and heat transfer coefficients because of the change in radius. The PDC simulations also result in different paths travelled and environments experienced because of the change in particle radius. The smaller pyroclasts for the PDC case travel the furthest distance, around 3.4 km (Figure 11d). The distance travelled does not vary significantly for the projectile clasts because the particle Reynolds number is high ($Re_p > 3 \times 10^4$) for all cases, and therefore the drag force on these large clasts only varies slightly. Both the projectile and PDC pyroclasts show the same trend, whereby cooling is fastest for the smaller clasts. This results in increasing rind thickness with decreasing clast radius (Figure 11).

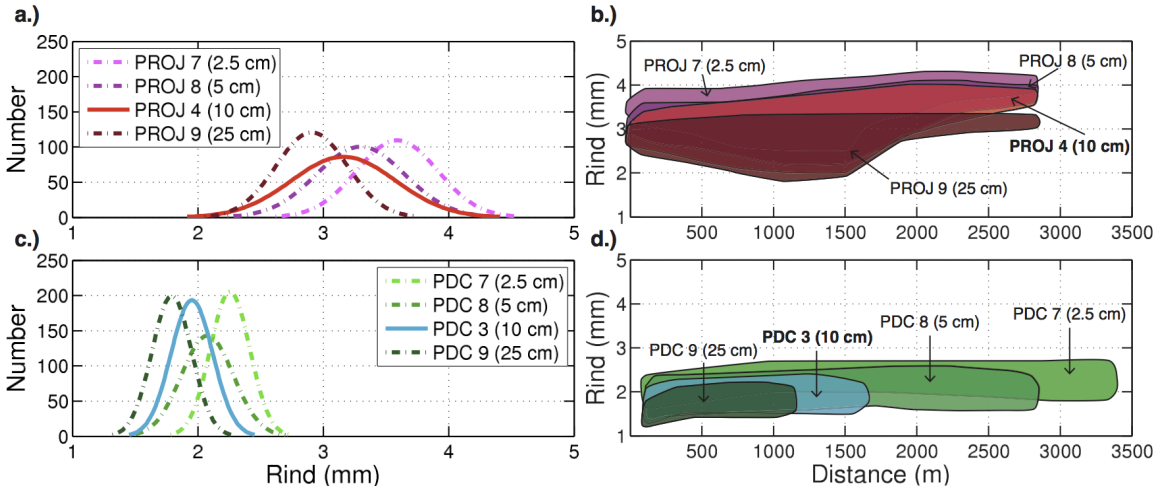

FIGURE 11: Variation in rind thickness as a result of clast radius. Both transport paths give the same result, decreasing rind thickness with increasing clast radius. a.) Distribution of rind thickness for projectiles with varying clast radius. b.) Rind thickness versus depositional distance from the vent for projectile pyroclasts of varying radius. The pink (2.5 cm) clasts have the thickest rinds. The magenta (5 cm) and red (10 cm) pyroclasts are the most similar in rind thickness, and the 25 cm pyroclasts have distinctly smaller rinds. c.) Distribution of rind thickness for PDC pyroclasts with varying radius. d.) PDC pyroclast rind thickness versus depositional distance from vent. Note the smallest clasts travel the furthest horizontal distance and have the thickest rinds.

2.4 Discussion

2.4.1 Thermal History Influence on Rind Thickness and Timescales

The transport regime (projectile or PDC) of a pyroclast has a first order influence on the rind thickness. Projectile pyroclasts in general develop thicker and less vesicular rinds than the PDC pyroclasts (Figure 9). Thicker rinds develop on the high velocity pyroclasts due to high heat fluxes. The high heat fluxes are a result of higher particle Reynolds number and greater temperature differences between the air and clast. The rind thickness of pyroclasts entrained in PDCs depends strongly on the thermal history of the current. The PDC pyroclasts develop thicker and less vesicular rinds as the initial gas temperature decreases. The decrease in initial gas temperature is a proxy for greater entrainment of ambient air during the collapse phase that forms the PDC. A PDC with limited ambient air entrainment retains heat, thus does not maintain enough of a temperature difference between the pyroclast and current to cool the pyroclast fast enough to restrict bubble growth. The thicker rinds are a result of the cooling rate of the pyroclast being faster than the growth rate of the bubbles. Thus the thermal environment (and initial air entrainment) affects the development and thickness of rinds in PDCs.

In all the PDC simulations, the 20 cm diameter clasts are concentrated in the bed load region of the current, which is the hotter part of the current in the simulation. This implies that the pyroclasts are not sampling the entire thermal environment of the PDC with equal fidelity and are biased toward sampling the thermal information from the bed load region. We did not incorporate the entrainment of colder substrate and subsequent cooling of the current from the bed load region. This lack of erosion could bias our currents to hotter conditions [*Eichelberger and Koch*, 1979; *Marti et al.*, 1991].

A regime diagram that compares transport regime and rind thicknesses (Figure 12) shows the distinction between the two transport paths and thermal environments. The vertical axis is the rind thickness (mm), $L_{rind,}$ over the conduction length scale (mm), $L_{conduction}$. The conduction length scale (in mm) is calculated using the total travel time of each pyroclast and the constant thermal diffusivity of the pyroclasts, where

$$L_{conduction} = \left(\sqrt{\tau_{transport} \cdot \kappa_c}\right) \cdot 1000 \quad (21)$$

The horizontal axis is τ_{rind} over $\tau_{transport}$. The regime diagram depicts that for some of the projectile and PDC pyroclasts, the conductive cooling during transport is not the determining factor but rather the heat flux from radiative and convective cooling is most significant in determining rind thickness. This occurs for pyroclasts that fall above the value of one on the vertical axis. Above this value, the rind thickness is greater than the length scale that is conductively cooled during the time the pyroclast travels.

On the horizontal axis, the pyroclasts with values greater than one have rinds that are still forming after they have been deposited. Such clasts are common in PDC deposits, but some projectile clasts also fall past one on the horizontal axis. It should be noted; however, that while some bubbles grow in these clasts after deposition, the majority of bubble growth (and rind formation) is during transport, as bubbles grow initially very quickly from diffusion-limited growth and then slowly reach their final size by viscous-limited growth. In the rind, all the bubbles stop growing and do not reach the *a priori* R_{final} (Equation 20) because viscosity of the melt surrounding the bubble terminates growth. Field observations suggest that rinds form during transport because some bombs are found abraded with both thick and thin rinds on a single clast. Field observation also indicates that some bombs are plastic at the time of deposition and

expand after deposition. Many bombs are found intact in deposits, but in their cool, expanded state they are exceedingly fragile [*Walker*, 1969; 1982; *Wright et al.*, 2007; *Giachetti et al.*, 2010]. The cooling model of *Wright et al.* (2007) determine that some of the thinner rinds on the ballistic clasts form before impact but the thicker rinds may have still grown after impact.

The regime diagram illustrates that pyroclasts entrained in PDCs develop rind thicknesses that are dependent on the surrounding gas temperature, which supports the hypothesis that the rind thickness in breadcrust bombs is a useful thermal proxy for the thermal history of PDCs. The diagram shows that with decreasing initial gas temperature, the PDC pyroclasts begin to collapse onto the projectile region (see Figure 12). With decreasing initial gas temperature (i.e., greater ambient air entrainment), PDC pyroclasts begin to develop thicker rinds due to faster cooling and higher viscosities at the edge of the clast. The faster cooling of a pyroclast restricts bubble growth more quickly and therefore causes τ_{rind} to decrease. All these changes cause the collapse of PDC pyroclasts onto the projectile pyroclast region.

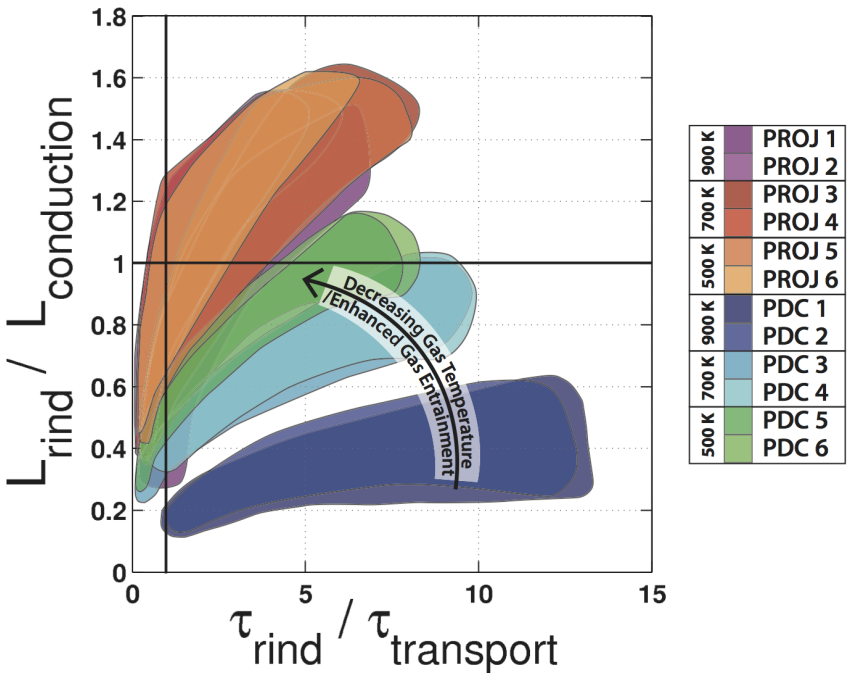

FIGURE 12: Regime diagram. As the initial gas temperature decreases the PDC pyroclasts develop thicker rinds and begin to collapse onto the projectile pyroclast area. Most of the PDC pyroclasts fall below 1 on the vertical axis; implying conductive cooling is more important for PDC pyroclast rind formation and heat flux cooling is more critical for projectile pyroclast rind formation. The projectile pyroclast area varies very little with the changing initial gas temperature. This is a result of the quick exit out of the eruptive column into the cool, ambient air environment. There are a few outliers for the projectiles from the general shaded area of each simulation. 99.4% of the projectile pyroclasts fall within their respective shaded areas and 100.0% of the PDC pyroclasts fall in their respective shaded areas. Pyroclasts that are greater than 1 on the horizontal axis still have bubbles growing in the rind after deposition. Even though the bubbles are still growing after deposition, the majority of bubble growth is almost complete before deposition and the growth after deposition is very slow with very little change in size.

The model developed here and the comparison between timescales, τ_{rind}, τ_{Tg}, and $\tau_{transport}$, for the projectiles and PDC pyroclasts provides insight into the timing of rind formation. In these calculations, τ_{rind} suggests that the first two minutes after eruption is critical for rind formation for this general case of homogeneous and instantaneous nucleation of bubbles with the onset of eruption (Table 4). For colder eruption environments, such as enhanced air entrainment or transport through ambient air, the time

for the rind to form is less than a minute. The pyroclasts transported in a hot PDC (initial gas temperature 900 K) take one to two minutes longer to cool, which causes thinner rinds to form. The rinds of pyroclasts from hot PDCs have larger average bubble sizes than the other pyroclast rinds. For initial gas temperatures of 900 and 700 K, the PDC pyroclasts with rind thicknesses similar to projectile pyroclasts are generally more vesicular than the projectile rinds (Figure 9). In the field, it may be possible to distinguish a PDC and projectile pyroclast from each other not only by rind thickness but also by the vesicularity of the rind.

2.4.2 Physical insights and assumptions from the model

An interesting detail that emerges from the coupled model is that viscous effects ultimately limit bubble growth in the rinds of breadcrust bombs. The coupled model should develop thicker rinds if the initial viscosity is increased either by using more silicic compositions or having a higher crystal volume fraction. The temperature range that bubble growth is terminated is higher than the glass transition temperature that is calculated under the cooling rate assumption of 10 K/min [*Giordano et al.*, 2005; 2008]. *Kaminski and Jaupart* (1997) found a similar result where the rinds on pumice formed from viscous quenching and before crossing the implied glass transition temperature. The initial glass transition temperature for our model is about 820 K (see Table 2), but it fluctuates in our model because of water loss through diffusion into bubbles. The assumption of a 10 K/min cooling rate for the glass transition temperature may not be realistic because the calculated cooling rate for all modeled rinds is greater than 80 K/min and often much faster. The viscous restriction of bubble growth at high cooling rates may be at the glass transition temperature applicable for higher cooling rates (> 10 K/min),

although this is difficult to access with the current model for glass transition with these compositions [*Giordano et al.*, 2008]. Therefore, this result suggests that faster cooling rates (and higher implied glass transition temperatures) may be required to predict final rind thicknesses if explicit bubble growth is not considered.

When constructing this model, several simplifying assumptions were made and here we evaluate the impact of these assumptions on cooling rate and rind formation. The assumption that particles are spherical and isotropic results in slower cooling compared to more jagged or oblong clasts because of their lower surface area. Experiments on particles over lower Reynolds numbers, $1.1 \times 10^4 < Re < 5.2 \times 10^4$, found that the cooling of spheroids (aspect ratios < 0.67) increased the Nusselt number by 40% or less compared to spherical clasts [*Zheng and List*, 1996]. We also used the black body emissivity for the radiative heat transfer and are therefore calculating the maximum radiative heat transfer. Radiative heat transfer is only important for the initial few seconds when there is a large temperature difference between the surface and surrounding air. Therefore, the black body assumption likely does not have a large effect on the cooling history. We do not examine the spinning and potentially faster cooling of the pyroclasts or the abrasion of the clasts as they travel, which might be important to the cooling history of individual clasts [*Vanderkluysen et al.*, 2012]. The same experiments of Zheng et al. (1996) found that spinning between 5-22 Hz made only a small difference in the total Nusselt number and this difference was within their experimental error.

An improvement of our model compared to previous efforts is the ability to take into account the differential velocity between the moving particle and the moving current of hot gases with heterogeneous temperatures. Furthermore, we use the correct empirical

Nusselt number from the experiments of *Achenbach* (1978) to calculate the heat transfer coefficient. As reported in the Appendix A, the Nusselt number from the *Achenbach* (1978) empirical equation for $Re_p > 4.0 \times 10^5$ is up to six times larger than their experimental results and the Nusselt value we calculate. The result of this correction is a lower Nusselt number and slower cooling of pyroclasts at high particle Reynolds number ($Re_p > 4.0 \times 10^5$). Consequently, though we have simplified the problem to better understand the sensitivity of the cooling to physical parameters, the simplification of assuming a sphere results in less than a 40% lower Nusselt number compared to non-spherical clasts. By comparison, our correction to the empirical equation for convective cooling [*Achenbach*, 1978] yields a Nusselt number that is up to six times smaller than the reported value for high Reynolds numbers.

2.4.3 Rind thickness as a result of initial water

Similar to previous studies [*Hort and Gardner*, 2000; *Wright et al.*, 2007], the rind thickness is found to decrease with increasing water concentration for both projectile and PDC models (Figure 10). This trend has been noted in ballistic breadcrust bombs at Guagua Pichincha where increasing rind thickness correlates to decreasing water content trapped in the glass of the rinds [*Wright et al.*, 2007], see Appendix B for comparison of results to samples. Breadcrust bombs at Guagua Pichincha are described as "finely breadcrusted" and "thickly breadcrusted". The finely breadcrusted bombs have rinds less than 3 mm, 1.4 - 3.1 wt. % H_2O, and 30-54 % vesicularity. The thickly breadcrusted bombs have rinds greater than 3 mm, 1.0 - 1.3 wt. % H_2O, and 0-13 % vesicularity [*Wright et al.*, 2007]. The small rind thickness and larger average bubble size in the rind

for the 3.0 wt. % rinds (Projectile 4f) could be described as finely breadcrusted and the 0.8 wt. % rinds (Projectile 4a and PDC 3a) could be classified as coarsely breadcrusted.

In our simulations, the thickest rinds develop around 1 wt. % H_2O, which parallels the findings of *Wright el al.,* (2007), see Appendix B. Some of the reasons rinds get thicker with decreasing water concentration is greater bubble nucleation delay [*Wright et al.*, 2007], composition, slower bubble growth rates, or slower flux of water. In our model it is the last two (see Appendix B for a comparison of compositional affect on rind thickness). With lower water concentration, the viscosity will be higher and will more effectively restrict and slow bubble growth. Lower water concentrations have slower growth rates and do not generate as steep of a concentration gradient as higher water contents. Therefore, the flux of water is slower for lower water concentrations. This results in slower growth rates [*Prousevitch et al.*, 1993]. A comparison of the two cooling schemes with variable water concentration reveals that the initial water concentration and transport regime are both first order influences on rind thickness. Modeling the formation of rind thickness using a better-constrained initial water concentration will likely provide clues to the thermal history of the clast.

2.4.4 Pyroclasts as a thermal proxy for PDCs

The model developed here provides a guideline for the interpretation of textural features of pyroclasts. As Figure 13 illustrates, pyroclasts ejected into material with higher gas temperatures have a wider variance of rind thicknesses once deposited. A small distribution in rind thickness is the result of a cooler current or a homogeneous transport history. A distal projectile pyroclast should have a thicker rind than the majority of the proximal projectiles. Analysis of water content in the rinds should also be

considered when comparing different projectile distances, as different rind thicknesses may also result from different fragmentation depths [*Wright et al.*, 2007]. If rind thicknesses are similar at one depositional area but the morphology of the clasts (i.e., radial bubble size distribution) are different, this may indicate variations in transport mechanisms or initial water concentrations. The radial bubble size distribution provides key information about a clast's thermal history and initial water concentration. In our model, generally a pyroclast that has a more vesicular and thinner rind indicates transport in a PDC, an abnormally hot thermal history, or high initial water concentration. The thinner, more vesicular rinds match the description of finely breadcrusted bombs from both *Wright et al.* (2007) and *Giachetti et al.* (2010) even though the descriptions for the Guagua Pichincha breadcrust bombs are for ballistic bombs. A coarsely breadcrusted bomb in our model is the result of low water concentration, low environment temperatures, or high transport velocities.

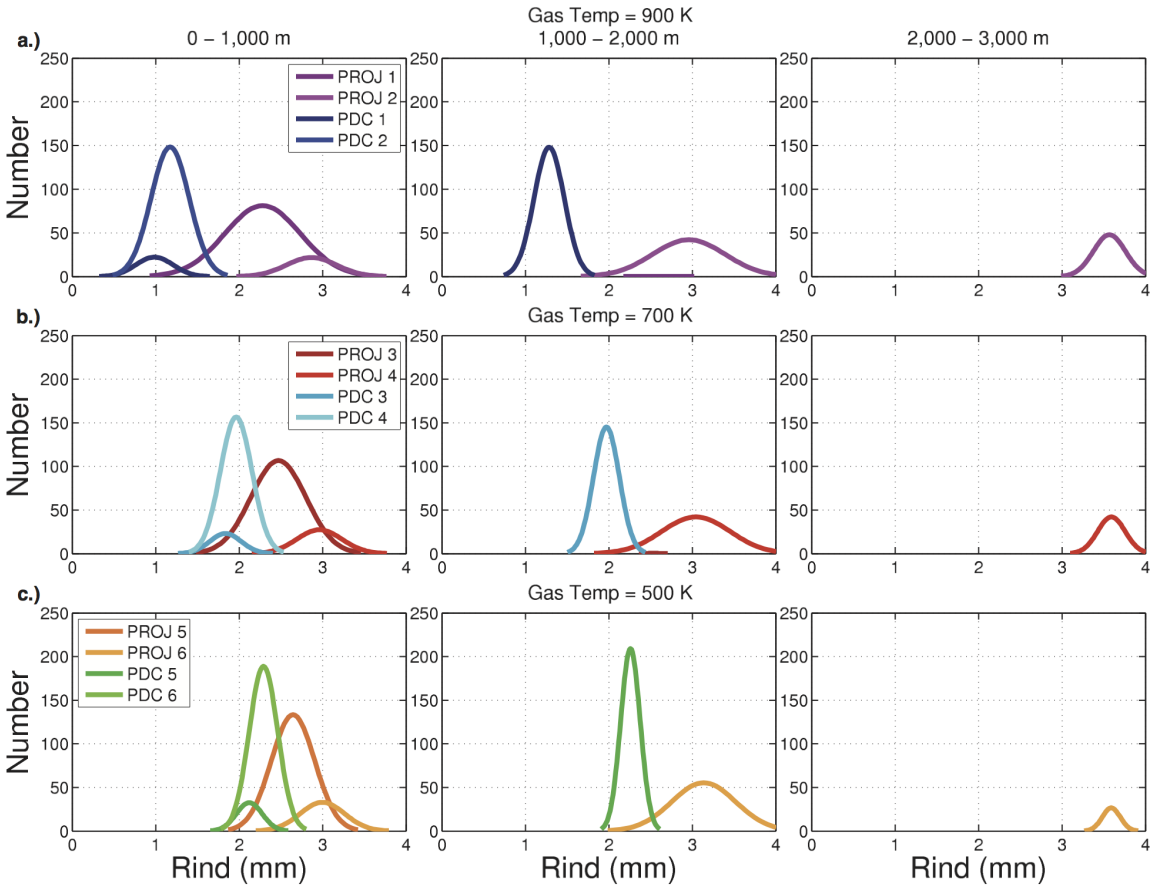

FIGURE 13: Distribution of rind thickness based on distance away from vent. From left to right are the binned deposit distances of 0 – 1,000 m., 1,000 – 2,000 m., and 2,000 – 3,000 m. a.) Distribution of rind thickness for an initial gas temperature of 900 K. b.) Distribution of rind thickness for an initial gas temperature of 700 K. Notice the increase in rind thickness for the PDC pyroclasts. c.) Distribution of rind thickness for an initial gas temperature of 500 K gas. The PDC pyroclast rind thickness distribution now overlaps more with the projectile rind thickness distribution. As the initial gas temperature is decreased (or the transport temperature is more homogeneous and similar to ambient air), the distribution in rind thickness becomes tighter for all the simulations. For the 2,000 – 3,000 m box at all gas temperatures, the high velocity projectiles have the mode with the largest rind thickness.

2.5 Conclusions

Breadcrust bombs are deposited not only as projectiles but are commonly found in PDC deposits. Our results show that systematic textural variation will develop in bombs transported by different means. The thickness and texture of the rinds in breadcrust

bombs reflect the influence of transport regime, transport properties, and clast properties. These affect the cooling rate, viscosity, and bubble growth rate that ultimately control the rind thickness. The simulations also provide insight into the timing of rind formation. For the general initial conditions postulated here, it takes < 2 minutes for the rinds to form. The integrated model compares how a rind develops in a pyroclast that is transported by the two end members of transportation, projectiles out of the buoyant plume and entrainment in PDCs. For clasts entrained in a hot PDC (gas temperature > 900 K), the developed rind thickness is noticeably thinner than those in ballistic projectiles. Clasts entrained in colder PDCs produce similar rind thicknesses as projectile pyroclasts. Thickly breadcrusted bombs found in the field are the result of fast cooling rates (low surrounding gas temperatures or high velocities) and slow bubble growth rates (low initial water concentration or high viscosities due to quick cooling). A finely breadcrusted bomb is indicative of a hot thermal environment, slow transport velocity, or high initial water concentration.

In summary, breadcrust rind thickness and porosity provide insight into the individual cooling history of pyroclasts. Under most conditions, the distribution of porosity and rind thickness for PDC and projectile clasts are distinct. The textural variations in PDC pyroclasts are typically indicative of variable amounts of current cooling from entrainment and initial water contents.

CHAPTER 3

THERMAL HISTORY OF PYROCLASTIC DENSITY CURRENTS AND PYROCLASTS AT TUNGURAHUA, ECUADOR

3.1 Introduction

Pyroclastic density currents (PDCs) are multiphase gravity currents composed of a mixture of volcanic particles and gas that propagate due to density differences between the current and the ambient air. The concentration of volcanic particles exist in a continuous spectrum from high to low within a PDC [*Fisher*, 1979; *Valentine*, 1987; *Druitt*, 1998; *Branney and Kokelaar*, 2002; *Burgisser and Bergantz*, 2002]. The concentration of particles is important for particle-particle collision stress, pore-pressure [*Roche et al.*, 2001; *Druitt et al.*, 2007; *Roche*, 2012] and gas-particle drag forces [*Valentine*, 1987; *Valentine and Wohletz*, 1989]. The internal physics of a PDC depend on the particle concentration gradient, basal friction, turbulence, degree of fluidization, temperature, and entrainment of ambient air [*Sparks*, 1976; *Bursik and Woods*, 1996; *Druitt*, 1998; *Branney and Kokelaar*, 2002; *Burgisser and Bergantz*, 2002; *Roche*, 2012]. Specifically, the entrainment of atmospheric air into PDCs influences a variety of non-linear internal processes, including 1) thermal expansion of the entrained gases, 2) changes to the density and particle concentration of the current, and 3) temperature variations, all of which can cause buoyancy reversal and liftoff, convection and destabilitization of the density stratification, and an increase in the size of the current [*Bursik and Woods*, 1996; *Freundt*, 2003; *Dufek and Bergantz*, 2007a]. However, the

entrainment efficiency and its effect on the thermal history and associated hazards of PDCs is not well constrained.

There are relatively few constraints on the entrainment rate of ambient air in hot PDCs [*Bursik and Woods*, 1996; *Andrews*, 2014], although there has been significant work examining the entrainment coefficient for volcanic plumes [*Morton et al.*, 1956; *Turner*, 1986; *Suzuki*, 2005; *Plourde et al.*, 2008; *Suzuki and Koyaguchi*, 2009; 2010; *Saffaraval et al.*, 2012]. For gravity currents, such as PDCs, previous models assume a well-mixed, homogeneous current and apply an empirical entrainment coefficient to examine runout distance, volume, and structure of the current [*Turner*, 1986; *Dade et al.*, 1994; *Bursik and Woods*, 1996]. Gravity current experiments are usually carried out in a fluid and/or in 2D channels [*Hallworth et al.*, 1993; 1996; *Bursik and Woods*, 2000; *Wells et al.*, 2010; *Andrews and Manga*, 2011; 2012], and cannot elucidate the complex relationship between a hot current, thermal expansion, and entrainment efficiency for a 3D current. The thermal expansion and buoyancy effects from entrainment of ambient air into a dilute PDC decrease the runout distance of a current compared to a non-entraining current [*Bursik and Woods*, 1996]. Additionally, the initial temperature of a current affects the amount and location of entrainment. A dilute PDC with temperature above ambient temperature is more efficient at lateral entrainment than ambient temperature currents. Non-ambient temperature currents also disperse over a shorter distance and more narrowly than ambient temperature currents [*Andrews*, 2014]. Understanding how ambient air entrainment into non-ambient temperature PDCs affects the thermal history, expansion, and runout distance of PDCs is therefore central to improving our understanding and prediction of flow behavior.

Currently, the methodology used to provide insight into the thermal history and characteristics of the associated PDC is through the direct temperature measurements of deposits [*Banks and Hoblitt*, 1981; *Cole et al.*, 2002], paleomagnetic studies of deposits [*Mandeville et al.*, 1994; *Cioni*, 2004; *Roperch et al.*, 2014; *Rader et al.*, 2015], and measurements of the abundance and reflectance of charcoal [*Scott and Glasspool*, 2005]. Additionally, the Forward Looking Infrared Radiometer (FLIR) camera can be used to measure the relative surface temperature of currents, examine plume behavior, eruptive style, and identify eruption duration [*Patrick*, 2007; *Steffke et al.*, 2010]. However, sample-based measurements provide limited spatial coverage and deposit-based measurements are time-integrated such that it can be difficult to unequivocally link bulk measurements with specific structures in the current. Large-scale multiphase numerical models of PDCs provide the needed link between these measurements and the spatial and temporal variations in entrainment efficiency, thermal history, and concentration gradients. An ideal eruption to bridge the observations with numerical models is the 2006 eruption of Tungurahua volcano, Ecuador. The 2006 eruption of Tungurahua had eye-witness observations of the eruption [*Hall et al.*, 1999; 2013], FLIR measurements [*Steffke et al.*, 2010; *Hall et al.*, 2013], PDC velocity estimates from seismometers [*Kelfoun et al.*, 2009; *Hall et al.*, 2013], paleomagnetic studies of deposits [*Roperch et al.*, 2014; *Rader et al.*, 2015], the presence of charcoal in PDC deposits, and detailed descriptions of field and deposits shortly after the cessation of the eruption [*Hall et al.*, 2013] that can constrain numerical models and allow the quantification of entrainment efficiency and the thermal evolution of a PDC.

Here, we present a novel approach to constrain the thermal history of PDCs using a 3D model validated by field and lab data. We use initial estimates of clast temperature, composition, and dissolved water content [*Samaniego et al.*, 2011; *Myers et al.*, 2014] in an Eulerian-Eulerian-Lagrangian (EEL) multiphase 3D model that is used to calculate pyroclast rind thickness and temperature of deposition [*Benage et al.*, 2014]. Pyroclasts with a dense rind and vesicular interior are called cauliflower/breadcrust bombs [*Walker*, 1969; *Wright et al.*, 2007]. The texture of cauliflower bombs provide data on the conduit stratigraphy before eruption [*Wright et al.*, 2007; *Giachetti et al.*, 2010] and the transport and cooling path of the bombs after eruption [*Benage et al.*, 2014]. The calculated cauliflower bomb rind thickness and temperature of deposition can be compared to rind thicknesses and paleomagnetic estimated emplacement temperatures [*Rader et al.*, 2015] of collected pyroclasts. The model and deposit comparison constrains the thermal history of the PDC. The purpose of this work is to study how entrainment efficiency affected the thermal history of the PDCs produced by the 2006 eruption at Tungurahua volcano.

3.2 Geological Setting

Tungurahua is a 5,023 m high andesitic stratovolcano (Lat. 01°28'S; Long. 78°27'W) located on the Eastern Cordillera in Ecuador and is currently in an eruptive phase that began in 1999 [*Hall et al.*, 2008; 2013]. In 2006, Tungurahua had two large eruptive sequences, July 14 – 16th and August 16-17th [*Barba et al.*, 2008; *Hall et al.*, 2013]. The whole-rock erupted products are andesitic (58-59 SiO_2) and have estimated magmatic temperatures ranging from 1,223 - 1,288 K [*Samaniego et al.*, 2011]. Melt inclusions hosted in olivine and pyroxene phenocrysts preserve two distinct magma

compositions: a basaltic-andesite that is volatile rich (~3.4 wt% H_2O) and a degassed andesite (~1.0 wt% H_2O), respectively [*Myers et al.*, 2014].

The July and August 2006 eruptions produced approximately 50 PDCs that destroyed homes, caused fatalities, and traveled up to 8.5 km form the vent to the base of the volcano [*Barba et al.*, 2008; *Kelfoun et al.*, 2009; *Hall et al.*, 2013]. The August 16-17th eruption generated about 30 PDCs with the larger currents estimated to have velocities around 20 - 33 m/s [*Kelfoun et al.*, 2009; *Hall et al.*, 2013]. The PDCs are associated with a range of particle concentrations based on massive to cross-stratified depositional structures [*Hall et al.*, 2013; *Douillet et al.*, 2013a]. The later PDCs from the August eruption formed lobes and levees that contain elevated concentrations of larger (>6.4 cm diameter) pancake clasts (cauliflower bombs) [*Douillet et al.*, 2013a], which are commonly found within the PDC deposits of Tungurahua [*Kelfoun et al.*, 2009; *Hall et al.*, 2013; *Douillet et al.*, 2013a].

The August 2006 PDCs are further analyzed to constrain the temperatures of the PDCs. Thermal images of Tungurahua's crater in August 2006 give a minimum temperature of 973 K at the time of the eruption [*Hall et al.*, 2013]. Thermoremanent demagnetization experiments determined the emplacement temperature of juvenile material from the PDCs was greater than 573 K [*Roperch et al.*, 2014; *Rader et al.*, 2015] and likely greater than 773 - 863 K [*Rader et al.*, 2015]. In contrast, most analyzed lithic clasts were found to be heated to less than 363 K (two lithics were heated above 483 and 813 K) before emplacement, which suggests that the August PDCs were not hot enough to heat most lithics above 363 K [*Rader et al.*, 2015]. Carbonized wood is ubiquitous in the PDC deposit area [*Hall et al.*, 2013] and from the experimental work of Pollock et al

[2010], a PDC temperature must be greater than 573 K to carbonize the local wood. Additionally, the lack of wooden structures igniting has led to the interpretation that the upper part of the PDCs remained below 573 K. At the lower end of the Juive Grande fan, temperatures of the PDC were estimated to be 373 - 573 K based on observations such as dead livestock and deformed plastic [*Hall et al.*, 2013].

3.3 Methods

The detailed thermal state of a PDC down the Juive Grande quebrada is quantified here using field data including rind thicknesses, paleomagnetic data, observed PDC velocities, and eruption and deposit descriptions together with a three-dimensional multiphase Eulerian-Eulerian-Lagrangina (EEL) model (Figure 14). The EEL model is applied to quantify the entrainment and cooling efficiency of the PDC and to link PDC dynamics to thermal proxies.

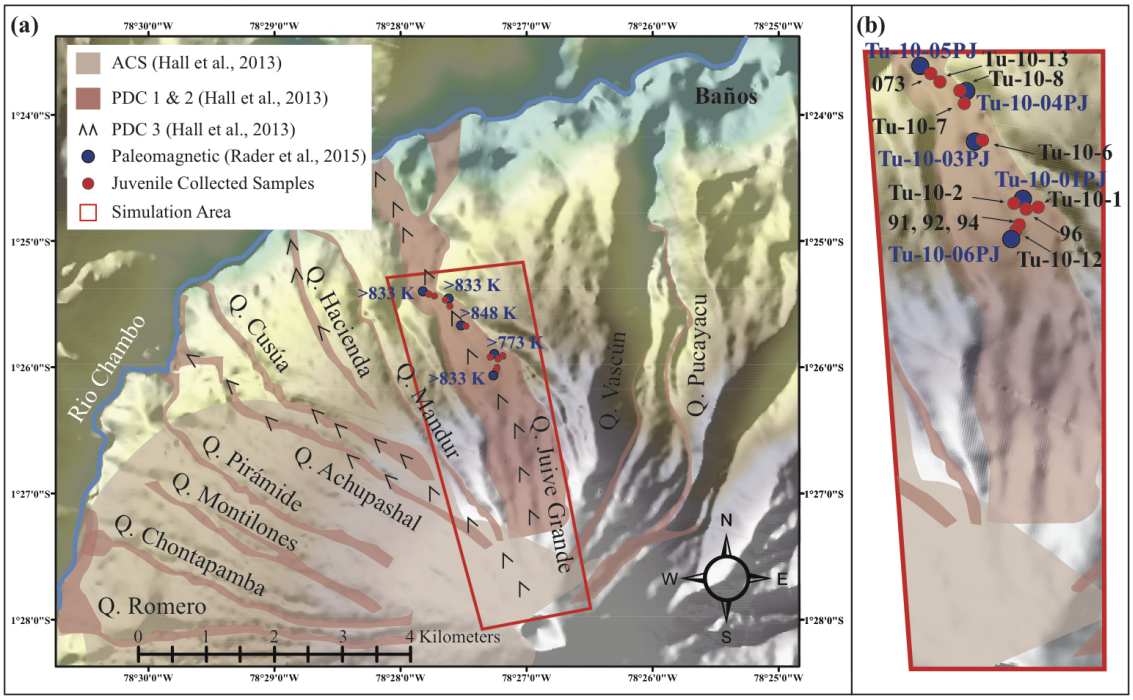

FIGURE 14: Tungurahua Map (a) Map of Tungurahua volcano with the pyroclastic density current deposits from the 2006 eruption (from Hall et al., 2013). The red box

outlines the simulation area. Blue symbols are the location of the sample collection for the paleomagnetic study of Rader et al. (2015) and minimum emplacement temperatures of the outer 1 cm^3 of the pyroclast. Red symbols denote the collection location of juvenile clasts and granulometry data. (b) Zoomed in simulation area with sample names.

3.3.1 Field Observations and Data

Juvenile pyroclasts, including cauliflower bombs, were collected for paleomagnetic studies [Rader et al., 2015], petrology [Myers et al., 2014], and for rind thickness measurements after the August 2006 eruption. The types and locations of the collected pyroclasts in the Juive Grande quebrada can be found in Figure 14. For rind thickness measurements, the sizes of all the collected pyroclasts were measured and density measurements were made on a subset following the methodology of Houghton and Wilson [1989]. The pyroclasts were cut into multiple sections to provide a range of surfaces from which to measure rind thicknesses. High-resolution photographs (1 pixel ≅ 20 μm) were taken of each surface with an oblique light that allowed for image processing using ImageJ (ImageJ Software [Schneider et al., 2012]) to calculate vesicle area and size distribution. The change in porosity (area of vesicles/total clast area) was binned at 1 mm distances from the edge of the clast to the interior. The change from a low porosity (~10-19%) to a consistently higher porosity was used to define the rind boundary (Figure 15). A minimum and maximum estimate was made for each analysis, as rind thickness can be irregular. For each pyroclast, at least 4 different surfaces were analyzed and one to five profiles were examined from each surface. The average of all the rind thickness calculations for each clast was then used as the rind thickness for each respective pyroclast.

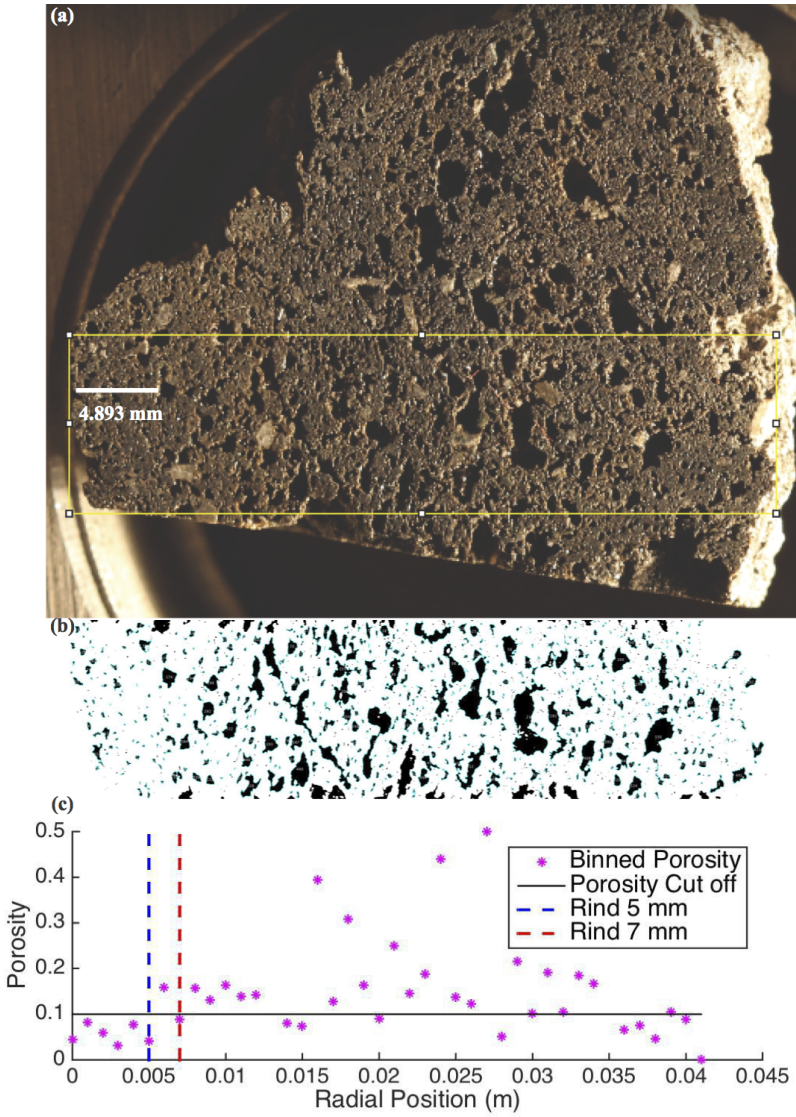

FIGURE 15: Rind calculation of pyroclast. (a) A cut section of a cauliflower bomb. The selection for analysis is outlined in yellow. A rind thickness estimate of 4.893 mm is made by the visual change from dense to vesicular. (b) The binary vesicle size and distribution of the outlined section in (a). Vesicles that touched the edge of the outline were disregarded for the porosity calculation. (c) Porosity binned every 1 mm to determine change from dense to vesicular texture in the pyroclast. A min and max estimate of rind thickness is 5 and 7 mm, respectively, for this clast.

3.3.2 Multiphase model

The multiphase model is applied to examine the entrainment of ambient air and thermal evolution of a PDC as it interacts with topography. The multiphase EEL model

was coupled to a 40-meter resolution DEM of Tungurahua volcano through a no-slip boundary condition. The multiphase model treats the PDC as a continuum fluid with 3 Eulerian phases where the continuum equations for mass, momentum, and energy are solved for gas and two solid particle phases [*Dufek and Bergantz*, 2007a]. The separate phases interact through drag forces and thermal exchanges [*Burgisser and Bergantz*, 2002; *Dufek and Bergantz*, 2007a; 2007b; *Dufek et al.*, 2009]. The thermal evolution of individual large pyroclasts transported in the PDC is examined through the Lagrangian component of the EEL model [*Benage et al.*, 2014]. The Lagrangian equation of motion includes terms for drag between the Eulerian gas and particle phases based on kinetic-collisional and frictional stresses [*Burgisser and Bergantz*, 2002; *Dufek and Bergantz*, 2007b; *Dufek et al.*, 2009]. When particle concentration exceeds 30 % of the current volume, the frictional regime dominates and the individual particles follow the concentrated portion of the current. Through the Lagrangian tracking, we model the formation of a rind and the subsequent temperature of deposition [*Benage et al.*, 2014], which are then compared to measured cauliflower rind thickness and paleomagnetic temperature results, respectively. The spatially variable thermal profile inside each clast is modeled in order to make these comparisons. A more detailed description of the rind and temperature of deposition model and initial conditions can be found in Chapter 2 [Benage et al., 2014]. The resolution of the model is 40 meters in both horizontal directions and 7 meters in the vertical direction, and the domain is 5.52 x 2.8 x 2.24 km.

3.3.3 Entrainment and Mixing Efficiency

The evolving temperature of a PDC is primarily the result of entrainment of ambient air through instabilities, particularly the Kelvin-Helmholtz instability and the

lobe-and-cleft instability. The Kelvin-Helmholtz instability occurs in a PDC when shear at the surface of the flow overcomes the density stratification of the fluid and air is entrained into the current. The lobe and cleft instability occurs at a no slip boundary where friction at the bed load region restricts the leading basal part of the flow and allows the upper portion of the leading edge to overrun and entrain the ambient air [*Simpson and Britter*, 1979]. In the EEL model, the conservation equations and constitutive relations solve mixing and entrainment of air through these instabilities. To evaluate entrainment of ambient air into the current, we define a current surface based on the volume fraction of particles, ε_p. We defined the PDC surface to be the transition from a dilute current to ambient air (i.e. no ash), which is near $\varepsilon_p \approx$ 1e-6 (or $-\log(\varepsilon_p) = 6$). The entrainment ratio has been defined as the velocity of air into the current over the characteristic or mean velocity within the current [*Wells et al.*, 2010; *Andrews*, 2014]. The dot product of the unit normal to the surface, $\hat{G}$, and velocity, U, at each grid point of the surface quantifies the proportion of the velocity field into or out of the dilute surface. The unit normal for the dilute surface is calculated using the flux of particles through the surface. We define the entrainment efficiency to be

$$Entrainment_{eff} = \frac{\left(\left\langle \hat{G} \right\rangle \bullet \left\langle U \right\rangle\right)}{\bar{U}_o} < 0 \qquad (22)$$

.

In addition to entrainment, another PDC dynamic is expansion of the current through thermal expansion of entrained air, added volume and buoyancy, and advection of material. Therefore, we define the expansion efficiency as

$$Expansion_{eff} = \frac{\left(\left\langle \hat{G} \right\rangle \bullet \left\langle U \right\rangle\right)}{\bar{U}_o} > 0 \qquad (23)$$

,

where $\bar{U}_o$ is the characteristic velocity. We define $\bar{U}_o$ to be 30 m/s since all the simulations begin with an initial velocity of 30 m/s and the mean, non-turbulent portion of the current fluctuates around 30 m/s. This method quantifies the entrainment or expansion efficiency along the entire 3D surface of the PDC and demonstrates where the current entrains ambient air and where the current expands through advection or buoyancy. A local gradient Richardson number is calculated throughout the current to examine where stable density stratification occurs within the current. The gradient Richardson number,

$$Ri = \frac{\left(\frac{-g}{\rho_{amb}}\right)\frac{\partial \rho_c}{\partial y}}{\left(\frac{\partial U}{\partial y}\right)^2}, \qquad (24)$$

is used to measure the stability of the density stratified flow compared to the overriding shear of the flow. A Richardson number less than 0.25 indicates a current has an unstable density gradient generating a Kelvin-Helmholtz instability [*Dufek and Bergantz*, 2007a]. The local Richardson number and entrainment/expansion efficiency quantify the heterogeneity and mixing efficiency within the current.

3.3.4 Simulation Parameter Space

The parameter space we explore for the model includes PDCs with a range of initial gas volume fraction and gas temperatures. The first set of simulations (Sim1A-C) have initial gas temperatures of 1,000 K to match the FLIR crater temperature [*Hall et al.*, 2013]. The second set of simulations (Sim2A-C) have initial gas temperatures of 800 K, and the third set simulations (Sim3A-C) have initial gas temperatures of 600 K. The lower temperatures are proxies for significant air entrainment during column collapse,

before the PDCs were generated. Simulations with initial volume fraction of gas $\varepsilon_g = 0.8$ are represented with an 'A', $\varepsilon_g = 0.7$ with a 'B', and $\varepsilon_g = 0.6$ with a 'C'. For all nine simulations, the initial current velocity is 30 m/s in agreement with observations [*Kelfoun et al.*, 2009; *Hall et al.*, 2013]. The simulations examined two distinct continuum particle phases, one with a relative concentration of 60% and particle diameter of 100 μm (Stokes number less than 1) and a second with a relative concentration of 40% and a diameter of 1000 μm (Stokes number greater than 1). The relative concentrations were obtained from the average of 8 granulometry measurements at Juive Grande quebrada that were separated into two bins with grain size equivalent to a Stokes number less than and greater than 1. These relative amounts were used as a best approximation to model the PDCs down the Juive Grande quebrada.

The Lagrangian particles begin with an initial temperature close to magmatic (1190 K [*Samaniego et al.*, 2011]), an initial water concentration of either 0.8, 1, or 2 wt% [*Myers et al.*, 2014], and andesite composition (Tu-10-06 PJ [*Myers et al.*, 2014], see Appendix C and location in Figure 14). The density used for the thermal properties of the pyroclasts was determined from the collected juvenile pyroclasts. The cauliflower bomb density ranged from 1250 – 1540 kg/m^3. An upper limit of 1500 kg/m^3 was used for the thermal calculations since we assumed the pyroclasts initially had ~0 porosity (initial bubble radii were 0.3 μm based on bubble growth model conditions). Heat capacity, $c_P = 1095$ Ws/kgK [*Bacon*, 1977], and thermal conductivity, k = 2.0 W/mK [*Clauser and Huenges*, 1995], were held constant. For the cauliflower bomb model, we assume one bubble nucleation event and bubble growth begins when the pyroclasts reach

the surface and are at ambient pressures. The thermal history and rind thickness of the Lagrangian tracked particles was calculated for pyroclasts with radii of 5 and 8 cm.

3.4 Results

The results of the measured field data, modeled current heterogeneities, such as entrainment efficiency and temperatures, and the modeled pyroclast depositional temperatures and rind thicknesses are presented here.

3.4.1 Field Data and Observations

The juvenile pyroclasts collected from the Juive Grande quebrada were emplaced at temperatures greater than 773 K at distances greater than 3.5 km from the vent (Figure 14 and 17). The thermoremanent demagnetization experiments were performed on 1 cm^3 cubes that moved from the rim of the pyroclast into the interior (personal comm. with Rader 2015). The 1 cm^3 rim of the pyroclasts in Juive Grande quebrada have emplacement temperatures from proximal to distal locations that are greater than 833, 773, 848, 833, 833 K (See Figure 14 for locations) and see Rader et al. (2015) for a full description of the paleomagnetic results. The juvenile clasts were collected from levees composed of cauliflower bombs atop an ash-rich matrix and from within the interior flow deposit. Many of the cauliflower bombs were unabraded in deposit but very fragile in their cooled state. The cauliflower bombs are oblong and generally have rinds developed on all sides. A few were found draping over older topography or the base of trees. The grain-size distribution of Juive Grande was fines-skewed, except Tu-10-12B and Tu-10-13B, which had a large fraction (>0.24) of coarse grains. A more detailed description of the deposits, stratigraphy, and sorting can be found in Douillet et al. [2013] and Hall et al. [2013]. The average rind thickness of the collected juvenile pyroclasts from Tungurahua

is 3.72 mm for an average clast radius of 4.63 cm (green point in Figure 18). The average rind thickness of the juvenile bombs varies from 1 mm to 6 mm and there is no clear trend in rind thickness with distance away from the vent (Figure 18a). The average radius of the collected pyroclasts varied from 3 to 9 cm (Figure 18b) with density varying between 1250 – 1540 kg/m^3.

3.4.2 Current Heterogeneity and Entrainment Efficiencies

The multiphase simulations produced heterogeneous currents that travelled down the flanks of the volcano (Figure 16) with the more concentrated portion of the current following the surface water drainage network. The heterogeneity of particle concentration affected the entrainment, mixing ability (Ri number Figure 16d-f), and therefore thermal evolution of the current. For all nine simulations, a distinct, stable bed load region developed at the base of the current and did not generate a well-mixed homogenous current. The bed load region had volume fraction of particles greater than 1% and lagged behind the dilute expanding portion of the current (Figure 16a & b). The dense bed load region was a small volume of the current and developed a strong density stratification (Ri >5) that inhibited mixing with the overlying more dilute and cooler part of the current. The dense bed load region (volume fraction of particles greater than 1%) cooled less than 50 K from the original temperature. The upper portion of the current, with a volume fraction of particles less than 1%, made up most of the current volume. The upper portion of the current had heterogeneous local gradient Richardson numbers and was unstable at locations that exhibited entrainment of ambient air. From proximal to distal locations, entrainment and mixing cooled the upper part of the current ~200 to 500 hundred Kelvin (Figure 16c-d) through the developed Kelvin-Helmholtz instabilities. The most exterior

part of the current approached ambient temperatures. The leading edge of the currents developed lobe and cleft instabilities, which cooled the leading nose of the current ~200 to 500 Kelvin (Figure 16e).

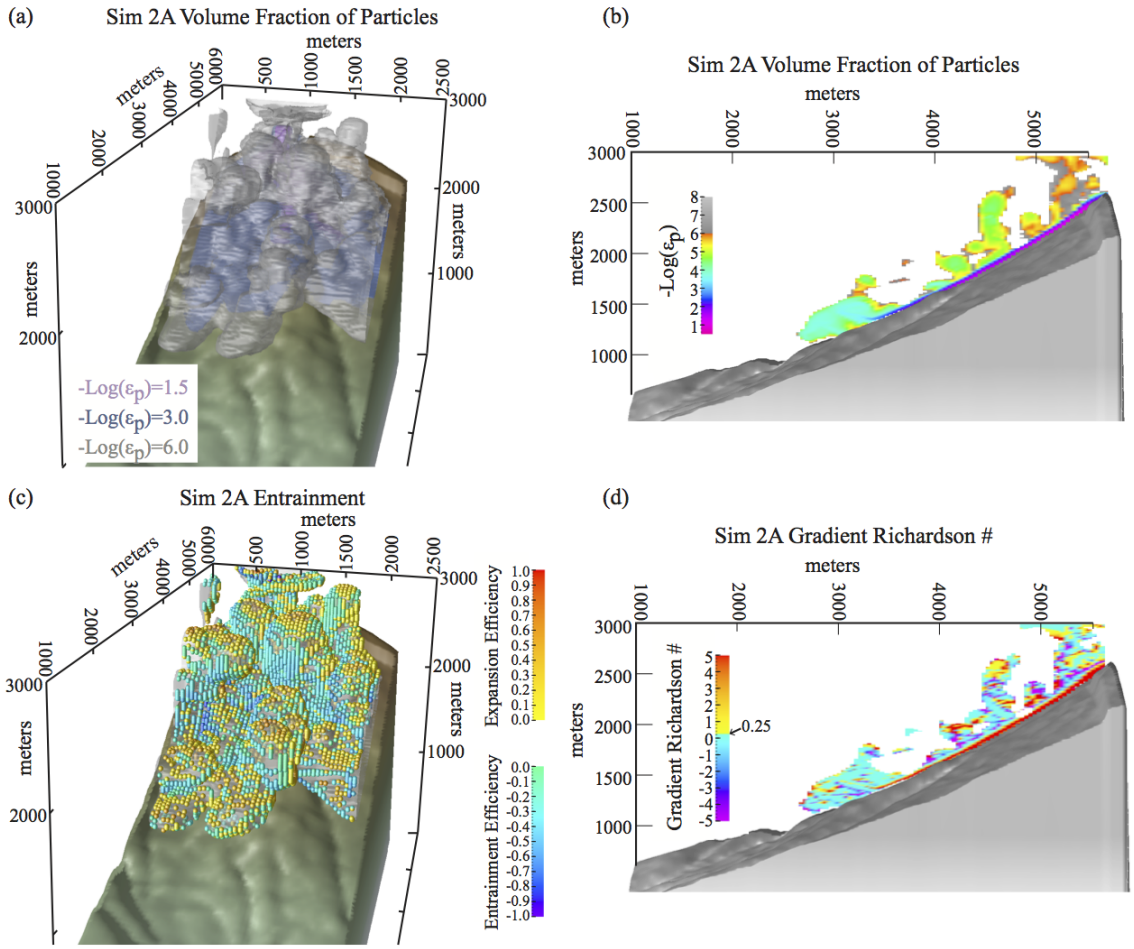

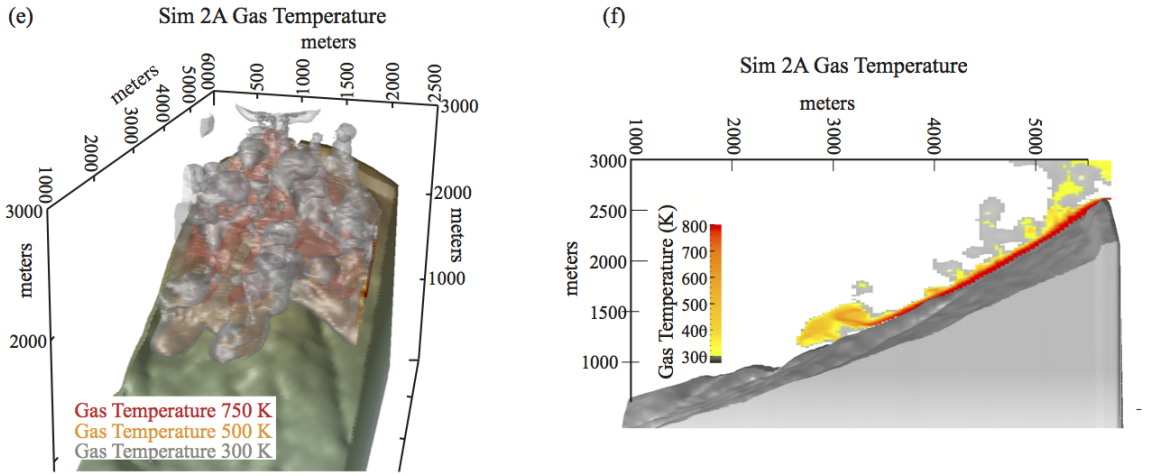

FIGURE 16: Snapshot of 3D simulations. Examples of concentration gradient, entrainment efficiency, and temperature heterogeneity. A snapshot at 80 seconds of Sim2A down the Juive Grande quebrada of Tungurahua volcano, Ecuador. The initial condition for the simulation is gas volume fraction, $\varepsilon_g = 0.8$ and initial gas temperature, $T_g = 800$ K. (a) The isosurface of three different volume fractions of particles (denoted by legend with similar colors for $-\log(\varepsilon_p) = 1.5$, 3.0, and 6.0 isosurfaces) highlights the more dilute ($-\log(\varepsilon_p) = 6$, gray isosurface) portion of the current is a significant volume of the current and where the turbulent regime occurs as seen by the billows resulting from Kelvin-Helmholtz instabilities and buoyancy effects. The more concentrated portion of the current is closer to the substrate and forms a smaller volume of the current. (b) A profile of the particle volume fraction through the current reveals the complex heterogeneity of the current. (c) The entrainment efficiency of ambient air into the dilute, turbulent portion of the current is around -0.2. The expansion efficiency denotes where the current is expanding due to advection and buoyancy effects. (d) A profile of the local gradient Richardson number. A current with a $Ri > 0.25$ is found to be stable such that no entrainment of the surrounding fluid occurs. When $Ri < 0.25$ or negative, Kelvin-Helmholtz instabilities form and the surrounding fluid is being entrained. The dense bed load region of the current has a $Ri >> 0.25$. (e) Three temperature isosurfaces of 750, 500, and 300 K (marked by similar color text in legend) show the dilute portion of the current cools close to ambient temperature but there is still a significant portion of the current that stays relatively hot. The isosurfaces show the leading toe edges cool more than the interior due to entrainment of ambient air from the lobe and cleft instabilities. (f) A temperature profile shows the 500 K temperature range within the current.

The overall entrainment efficiency for the upper portion of the PDC was more dependent on the initial temperature of the current than the initial concentration. In all simulations, with entrainment efficiency averaged over space, the entrainment efficiency fluctuated with time around -0.2. Only after about 60 seconds did the entrainment

efficiencies begin to separate according to current temperature. At 100 seconds, the overall entrainment efficiency (efficiency averaged over space and time) of Sim1A-Sim1C (initial gas temperature of 1,000K) was -0.24 to -0.27. Sim2A-Sim2C (initial gas temperature 800 K) had overall entrainment efficiencies of ~-0.2 to -0.21 and Sim3A-Sim3C (initial gas temperature 600 K) had efficiencies near -0.19. However, entrainment is very time dependent and not a steady value through time. Entrainment occurred along the front of the Kelvin-Helmholtz instabilities and the sides of the leading edge of the current (Figure 16c). The negative value for entrainment indicates ambient air is being entrained into the current and is opposite the PDC flow direction. The current expanded or was buoyant along the top of the leading nose and top of the billows. The hotter currents had the highest entrainment and expansion efficiencies and the largest current volume, whereas the colder (initial gas temperature 600 K) PDCs had the lowest entrainment and expansion efficiencies as well as the smallest current volume.

3.4.3 Depositional Temperatures

The tracked Lagrangian pyroclasts in the EEL model all initially had a temperature of 1190 K. To compare the depositional temperature to the 1 cm^3 rim results of the paleomagnetic study [*Rader et al.*, 2015], the results are presented as the average temperature of the 1 cm rim of the pyroclasts at deposition (Figure 17). The depositional temperature of the 1 cm rim of the Lagrangian particles decreased with increasing distance from the vent (Figure 17). In the simulation, the Lagrangian particles concentrated in the dense bed load region of the PDC and travelled through the hotter parts of the current with little exposure to cold ambient air. The particles travelling in a PDC with an initial temperature of 1,000 K (Sim1A-Sim1C) remained very hot with

depositional temperatures of the 1 cm rim greater than 940 K. The second set of simulations (Sim2A-2C), with initial gas temperature of 800 K, have pyroclasts 1 cm rim depositional temperatures greater than 850 K. The third simulation set (Sim3A-Sim3C), with an initial gas temperature of 600 K, have particle rims that cooled more efficiently and down to ~825 K for the 8 cm pyroclasts and down to ~800 K for the 5 cm pyroclasts at a distance of 3.5 – 4.5 km away from the vent.

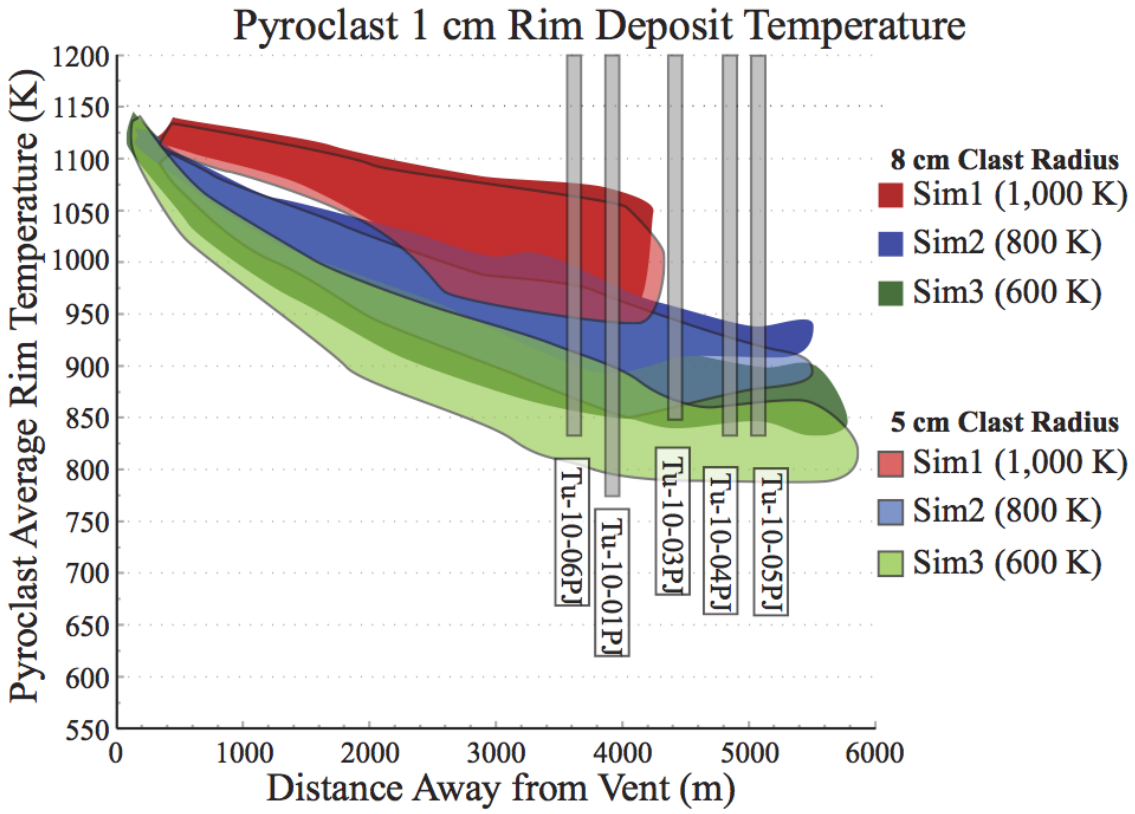

FIGURE 17: Depositional Temperature. The figure shows the depositional temperature of the outer 1 cm of the modeled pyroclasts and locations of paleomagnetic samples where the minimum emplacement temperature of the 1cm^3 rim from Rader et al. (2015) are denoted with the bottom of the gray rectangle. For the modeled pyroclasts, the initial clast temperature was 1190 K and the clast radius of 8 cm and 5 cm is denoted by simulation color and either no outline or outline, respectively. The parentheses with the simulations denote the PDCs initial gas temperature. None of the modeled pyroclasts for Sim1 and Sim2 lie below the lower bound of the paleomagnetic results. For Sim3, the 5 cm radius pyroclasts entrained in a 600 K current fall below the paleomagnetic minimum emplacement temperature, except for sample Tu-10-01PJ.

3.4.4 Rind Thicknesses

The gas temperature of the PDC and the initial dissolved water concentration of the pyroclasts affect the modeled thickness of the rind in pyroclasts carried within the PDC (Figure 18a). For PDCs with initial gas temperature of 1,000 K (Sim1A-1C), the majority of the 8 cm radius pyroclasts with 1 wt% water developed no rinds and a small fraction developed up to a 1.2 mm rind. For pyroclasts of Sim1 with water concentrations of 0.8, 1.0, and 2.0 wt% water, the rind thickness ranged from 0 – 2.4 mm (Figure 18a). The 8 cm pyroclasts carried in the 800 K PDCs (Sim2A-2C) developed rinds with thicknesses of 1.36 to 2 mm, 3.12 to 3.68 mm, and 4 to 4.64 mm, for initial dissolved water concentration of 0.8, 1.0, and 2.0 wt%, respectively. The 5 cm pyroclast and 1 wt% water had rind thicknesses of 3.55 to 3.95 mm. For the PDCs with initial gas temperature of 600 K (Sim3A-3C), the 8 cm pyroclasts had rind thicknesses of 1.68 – 2.08, 3.68 to 4.16 mm, and 4.64 to 5.36 mm, for initial dissolved water concentration of 0.8, 1.0, and 2.0 wt%, respectively. The 5 cm radius pyroclasts had rind thicknesses of 4.0 to 4.4 mm (Figure 18a). In all the simulations, the rind thickness did not vary with distance away from the vent. For the PDCs with initial gas temperature of 800 or 600 K, the rind thickness at emplacement was within ±0.25 mm of the final quenched thickness. The rinds were mostly quenched within the first 20-30 seconds of transport. For the 1,000 K PDCs, not all the pyroclasts were fully quenched at deposition and either continued to form a small rind or continued volatile exsolution and formed a vesicular pyroclast. The transport times for the pyroclasts carried in the PDCs varied from 20 seconds up to the final model simulation time of ~ 3 minutes.

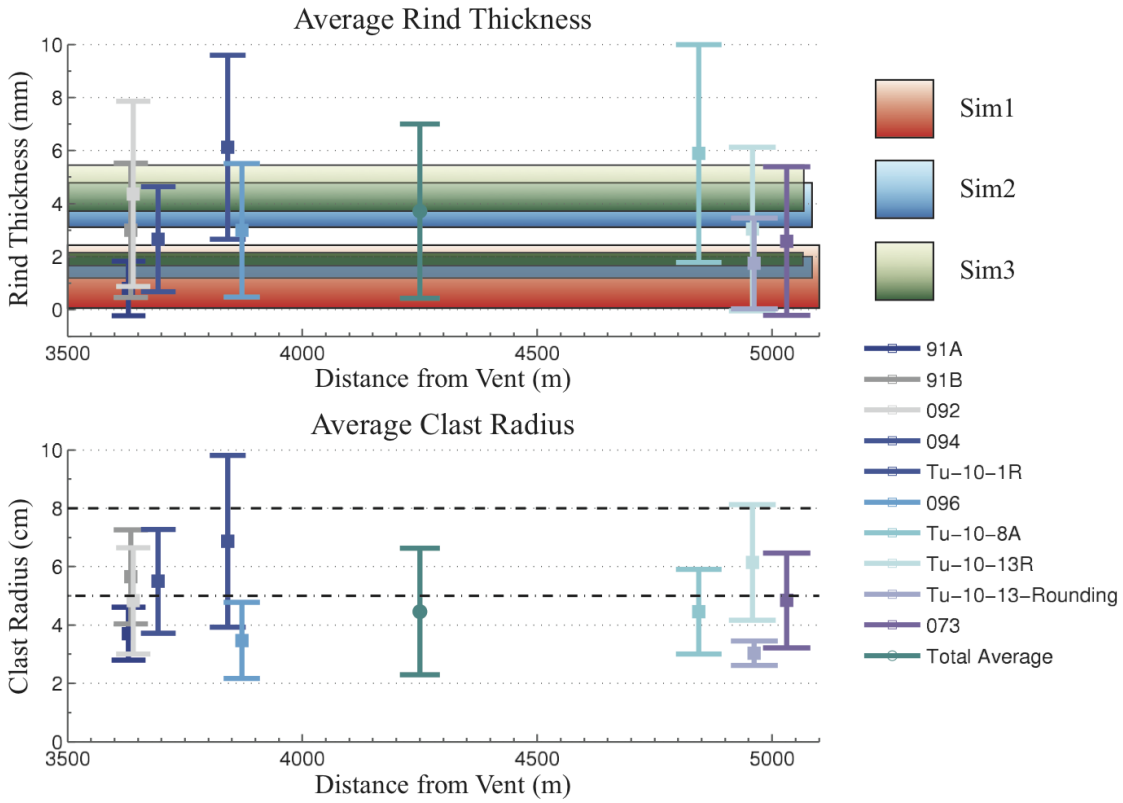

FIGURE 18: Comparison of Rind Thicknesses for sampled and modeled pyroclasts (a) The simulation rind thicknesses for Sim1 – Sim3 are depicted by the colored rectangles and contain rind thicknesses for 8 cm pyroclasts with initial dissolved water of 0.8, 1.0, and 2.0 wt% and 5 cm pyroclasts with initial dissolved water of 1.0 wt%. The rectangles are offset near 5,000 m to help distinguish the different rind thicknesses for each set of simulations. This offset does not signify the final travel distance of the modeled pyroclasts. The smaller rectangles of Sim2 and Sim3 falling within the Sim1 rectangle are for the 8 cm pyroclasts with 2.0 wt% water. Sim3 developed the thickest rinds and Sim1 has either no rind or a rind less than 2.4 mm. The average rind thickness of collected juvenile clasts from the 2006 eruption of Tungurahua are depicted with the scattered points and standard deviation bars. The average of all collected pyroclast rind thicknesses is denoted with the green point and error bar near 4,250 m. The clasts from Tungurahua have average rind thicknesses of 1 – 6 mm and fall within the range of Sim2 and Sim3 rinds but the smaller rind thickness clasts do fall within Sim1. (b) The average clast radius of the three axes measured for each collected juvenile clast.

3.5 Discussion

The thermal proxies, emplacement temperature, and rind thickness provide bounds to the thermal state of the Juive Grande PDCs and fit within the view of the PDC observations. For the PDC simulations with an initial gas temperature of 800 or 1000 K, the average depositional temperature of the outer 1 cm of 5 or 8 cm radius pyroclasts was greater than the paleomagnetic minimum emplacement temperature of the rims (Figure 17). The paleomagnetic results provide a lower bound for the PDC depositional temperature. The minimum emplacement temperature is the temperature at which the juvenile pyroclast magnetization was fully unblocked for the Juive Grande samples and was around 773 – 848 K [*Rader et al.*, 2015]. The modeled 5 cm pyroclasts with a PDC initial temperature of 600 K have emplacement temperatures above 790 K. This is below the minimum emplacement temperatures determined from paleomagnetic data, expect for Tu-10-01PJ (Figure 17). The 8 cm pyroclasts transported in a PDC with an initial temperature of 600 K approach or fall below the paleomagnetic emplacement temperature. This suggests the Juive Grande PDCs likely had a temperature above 600 K, as a PDC temperature around or less than 600 K would result in depositional temperatures less than the paleomagnetic minimum emplacement temperature. The rind thickness results provide a rough upper bound on PDC temperature. The tracked pyroclasts with varying initial dissolved water concentration in the 1000 K PDCs (Sim1A-Sim1C) developed no rind or a rind thickness less than 2.4 mm. However, the 800 and 600 K PDCs are able to have pyroclasts that developed rind thicknesses similar to those observed in the deposits (Figure 18). The presence of a rind on all sides of the oblong cauliflower bombs found in deposit suggests at least a portion of the rind developed while in transport and from cooling. The inability of the 1,000 K PDCs

(Sim1A-C) to develop the thicker rinds similar to the deposits and the high depositional temperature of the clasts suggest the base of the Juive Grande PDCs had temperatures less than 1,000 K. An uncertainty in the cooling history and depositional temperature of the modeled pyroclasts is the initial clast temperature. However, the initial eruptive temperature of pyroclasts is unknown and the only constraint is that the pyroclasts are near magmatic temperature.

The thermal proxies constrained within the observations allow the EEL multiphase models to link thermal observations with specific structures and dynamics. In all the simulations, the PDCs develop a concentration bed load region (Figure 16a-b) that has the carrying capacity to carry larger pyroclasts kilometers away from the vent. However, the bed load has limited mixing with the upper portion of the flow due to the large, stable concentration gradients. The gradient Richardson number for the bed load region quantifies the inefficient mixing (and consequent lack of cooling) of the basal part of the PDC. For the pyroclasts in the bed load region, an initial gas temperature greater than 600 K is required to deposit pyroclasts above the minimum emplacement temperature (773-848 K). At Juive Grande, PDCs were hot enough to kill animals, and form fumaroles in dammed rivers, but not hot enough to ignite wooden structures [*Hall et al.*, 2013]. The presence of carbonized wood in the deposits [*Hall et al.*, 2013] suggests the currents were above 573 K [*Pollock et al.*, 2010] while the lack of melted plastics near deposits suggest the exterior of the current was less than 573 K [*Hall et al.*, 2013]. The modeled PDCs and associated pyroclasts suggests the bed load region where the larger clasts were congregated was greater than 600 K and less than 1000 K but the upper part of the current and distal regions approached temperatures of 300 K or less, which

agrees with the observations of Hall et al. [2013]. To have a bed load temperature less than magmatic temperature suggests the PDCs initiated much cooler than magmatic temperatures as the lower region of the current cannot efficiently cool once the PDC develops. This suggests that (1) the flows initiated from an unstable spatter collapse, or (2) mixing in the low eruptive column already ingests/entrains sufficient air (25-90%) in the collapse phase to start the PDC near these temperatures. Though these findings suggest the base of the current was inefficient at mixing and cooling, the exterior part of the current is dynamically and thermally different.

The PDCs are heterogeneous both thermally and in concentration of particles, which dictates different dynamics throughout the currents. The dilute, upper portion of the PDCs cooled efficiently and entrained enough ambient air to approach ambient temperatures. This dilute portion of the current cooled 200 - 500 K from the original temperature. The efficient cooling was from entrainment and mixing of colder ambient air through Kelvin-Helmholtz and lobe-and-cleft instabilities. The three-dimensional entrainment efficiencies for the dilute, turbulent current were ~-0.2 and similar to the results of the dilute PDC experiments of Andrews [2014]. The hotter PDC (1,000 K) had the higher entrainment efficiency and developed more coherent, larger billows in the upper part of the current. Similar to the findings of Andrews [2014], the initial temperature of the PDCs affects the thermal history, entrainment efficiency, and structure of the PDC. The simulations suggest PDCs are complex, heterogeneous currents with varying particle concentration and mixing abilities throughout the current.

The link of thermal proxies with modeled PDC dynamics improves our understanding of PDC structure. Pyroclastic density currents have been assumed to vary

in concentration of particles due to gravity, settling velocities, turbulence scales and varying stokes numbers, but our inability to measure or see into the currents limits our knowledge of structure and dynamics in PDCs [*Druitt*, 1998; *Branney and Kokelaar*, 2002; *Burgisser and Bergantz*, 2002; *Dufek and Bergantz*, 2007a]. We have shown here that PDCs heterogeneous in particle concentration, temperature, and dynamics can match observations of PDCs down a volcano and the resultant thermal proxies collected in the field. This illuminates that PDCs do not have to be homogeneous well-mixed currents and that a single current can have varying concentration of particles, density stratification, and mixing efficiencies. This illuminates that PDCs can exist as a continuous spectrum of particle concentration [*Fisher*, 1979; *Druitt*, 1998; *Branney and Kokelaar*, 2002] The entrainment efficiencies highlight that a PDCs entrainment varies spatially and temporally and the assumption of a well-mixed current with a single entrainment coefficient [*Turner*, 1986; *Dade et al.*, 1994; *Bursik and Woods*, 1996] does not apply for these slower, more dense PDCs and might not fully solve the thermal evolution of the PDC. The temperature of PDCs is more important than the particle concentrations (0.6-0.8) for entrainment efficiencies but both particle concentration and temperature of the PDC affects current structure. A hotter current is more efficient at entraining ambient air, expansion, and formation of billows, whereas a colder current is more likely to remain a ground-hugging gravity current at these lower velocities. For concentrated, slow PDCs, the temperature at the base of the current is likely a function of the temperature at the genesis of the PDC and not from entrainment and mixing of ambient air as the current propagates. The initial PDC temperature could be cooler than magmatic from entrainment of ambient air during column collapse.

3.6 Conclusion

Pyroclastic density currents can be efficient at entrainment of ambient air in the upper dilute portion of a PDC where mixing and cooling can occur. However, stable density stratification in the basal portion of the PDC does not allow for efficient mixing and cooling. The spatial and temporal heterogeneities of a PDC suggest the Juive Grande pyroclastic density currents ranged from a dense flow to a dilute surge in one single current with a warm (>600 to <1,000 K) bed load region and a dilute, cooler overlying region. The currents likely initiated with temperatures less than 1,000 K and a bed load region that stayed sufficiently hot for the travel time of the current. This scenario is corroborated with modeled pyroclast depositional temperatures and rind thicknesses that match the Juive Grande PDC deposits and other observations.

CHAPTER 4

CONCLUSION AND FUTURE DIRECTIONS

The entrainment efficiency and thermal history of PDCs has been shown to influence certain PDC dynamics and hazards, such as runout distance [*Bursik and Woods*, 1996; *Andrews*, 2014]. However, previous work has been limited to dilute regions and has not been able to evaluate the full thermal history of PDCs. The ability to constrain the thermal history from deposits or dilute models is complicated by the complex and unknown dynamics of PDCs such as concentration of particles, particle concentration gradients, mixing efficiency, temperature, and entrainment efficiency [*Druitt*, 1998; *Branney and Kokelaar*, 2002; *Dufek and Bergantz*, 2007a; *Andrews*, 2014]. Additionally, there are few thermal proxies or in-situ measurements of PDCs to constrain the thermal history or dynamics. In order to further our fundamental understanding of the internal physical processes of PDCs, numerical models validated with observations and deposits are needed.

The numerical models presented here seek to use in-situ secondary thermal proxies, field data, and three-dimensional multiphase models to better understand PDC dynamics, entrainment efficiency, and thermal history. In Chapter 2, numerical models were developed to test the hypothesis that breadcrust bombs develop rinds as results of the cooling and transport history. Brief overviews of the models results are:

- Water concentration, transport path, and thermal history of a juvenile pyroclast has a first order influence on rind thickness,
- Models suggest majority of the rind developed in transport and before deposition,

- The surface of pyroclasts can have cooling rates >> 30 K/min and therefore might have a different glass transition temperature than has been found through experiments with 10 K/min cooling rates, and
- The rind thickness of pyroclasts can be a useful secondary thermal proxy to constrain the thermal history of PDCs.

With the development of a useful secondary thermal proxy to study PDCs, the models were expanded to constrain the entrainment efficiency and thermal state of PDCs from the 2006 Tungurahua eruption using three-dimensional multiphase (EEL) models. Three separate continua (one gas, two particle) phases were modeled to elucidate particle concentration gradient, entrainment efficiency, and thermal evolution of PDCs down the canyons of Tungurahua. The simulations show that hypothesized inhibited mixing of the bed load region did occur. The PDCs developed a stable density stratification in the bed load region that limited mixing and allowed the basal part of the PDC to maintain a roughly constant temperature. However, the results also show that the PDCs down Juive Grande likely varied in concentration, concentration gradients, density stratification stability, and temperature. The simulations illustrate that the PDCs are heterogeneous and that particle concentration gradients affect entrainment, mixing ability, and the thermal evolution of the current. Brief reviews of the results are:

- PDC bed load region at Juive Grande was likely >600 K and <1,000 K due to:
    - Modeled 1,000 K PDCs had pyroclasts develop 0 to 2.4 mm rinds (for all variations of modeled pyroclast size and water concentration) and 1 cm rim depositional temperatures greater than 940 K

    - Modeled 800 K PDCs had pyroclasts develop 1.36 to 2 mm and 3.12 to 4.64 mm rinds (for water concentration of 0.8, 1, and 2 wt% for 8 cm pyroclasts and 1 wt% for 5 cm pyroclasts) and 1 cm rim depositional temperatures greater than 850 K,
    - Modeled 600 K PDCs had pyroclasts develop 1.68 to 2.08 mm and 3.68 to 5.36 mm rinds (for water concentration of 0.8, 1, and 2 wt% for 8 cm pyroclasts and 1 wt% for 5 cm pyroclasts) and depositional temperatures greater than 800 K,
    - Paleomagnetic data gives emplacement temperatures greater than 773, 833, and 848 K and the average rind thickness of collected pyroclasts is 3.72 mm,
- PDCs develop a stable, dense bed load that is greater than 1 vol% of particles and maintain a similar temperature to the original PDC temperature,
- Dilute upper portion efficient at entraining ambient air with efficiency fluctuating around ~ -0.2,

  and
- Temperature of the current has a greater effect on entrainment efficiency of ambient air in the dilute region of the current than the initial concentration of the PDC.

In conclusion, this thesis has shown through developed multiscale models and three-dimensional multiphase models that the PDCs at Tungurahua were likely >600 K and <800 K at the bed load region and the upper dilute portion of the PDC approached ambient air temperatures. This works used first principle physical models to show that a

single PDC can vary in particle concentration, density stratification, mixing efficiencies, and temperature.

Though this research quantified the thermal history and dynamics of PDCs, it also revealed additional questions, such as:

- *How does entrainment in PDCs affect the final runout distance?*
- *How does the initiation of PDCs through boiling-over, column collapse, or spatter collapse affect PDC formation and temperature?*
- *Does column collapse entrain enough air to cause PDCs to initiate at temperatures less than magmatic?*

Due to computational limitations, the simulations performed here were unable to study the full scale of a volcanic eruption. The future direction for this work is to expand the simulation domain in order to simulate eruptive plume entrainment, collapse, PDC formation, and runout distance. This will be accomplished through scaling our simulations from 64-256 processors up to 500 – 1000 processors. Proposals for supercomputer hours have been submitted to the National Science Foundation XSEDE cluster, as our cluster at Georgia Tech is not large enough to accomplish these simulations.

The model of breadcrust bomb formation indicates that the water content (i.e. degree of degassing) and cooling rate of the juvenile pyroclasts control bubble growth at atmospheric pressure and may cause the necessary growth delay to form dense, non-vesicular rinds [*Benage et al.*, 2014]. Additional studies have shown that breadcrust bombs provide a detailed record of magma stored at shallow-intermediate depths in the conduit [*Hoblitt and Harmon*, 1993; *Wright et al.*, 2007; *Giachetti et al.*, 2010].

Therefore, because the rinds of breadcrust bombs quench shortly after fragmentation, the textures and volatile contents of these pyroclasts provide a unique dataset with which to explore (1) pre-fragmentation conduit stratigraphy [*Wright et al.*, 2007; *Giachetti et al.*, 2010] and (2) post-fragmentation processes of vesiculation, cooling, and eruptive partitioning into ballistic or pyroclastic flows [*Benage et al.*, 2014]. Further textural analysis of breadcrust bombs at various volcanoes can be used to reconstruct the pre-eruptive conduit stratigraphy and the eruptive processes necessary to form breadcrust bombs. Textural and geochemical characterization of erupted pyroclasts can be used to quantify pre- and syn-eruptive conduit parameters, such as decompression (ascent) rates and durations of shallow magma storage [*Cashman*, 1992; *Blundy and Cashman*, 2005; *Cashman and McConnell*, 2005], through comparisons with experiments [*Geschwind and Rutherford*, 1995; *Hammer and Rutherford*, 2002] and the intervals between eruptive events (e.g., [*Hammer et al.*, 2000]). The further analysis of breadcrust bombs through textural analysis and numerical models can elucidate the eruptive processes that result in the generation of the unique breadcrust bombs.

Lastly, one of the largest uncertainties in PDCs is the depositional process and matching numerical models to deposit lithofacies [*Branney and Kokelaar*, 2002]. Further work through experimental and numerical models is needed to understand how the steadiness, uniformity, particle concentration, and bed shear stress affects the type of lithofacies so models can be more quantitatively compared to deposits [*Branney and Kokelaar*, 2002].

APPENDIX A

NUSSELT NUMBER

The empirical equation to calculate the Nusselt number for Reynolds numbers greater than 4×10^5 is found through experiments on spheres (Achenbach 1978). The value of coefficient, *a,* for that empirical equation in *Achenbach* (1978) does not match their data. The value for *a* is stated as 5×10^{-3} in *Achenbach* (1978), and we will refer to it from now on as a_2. Our own polynomial fit of the experimental data reveals that the correct coefficient value is $a_1 = 5 \times 10^{-4}$ (Figure A1). The use of coefficient a_2 results in over 5 times larger Nusselt numbers than were found experimentally for $Re > 4 \times 10^5$. We use the value of a_2 reported by *Achenbach* (1978) and the value of a_1 in our coupled model to compare the impact of a_2 on cooling calculations. We will focus here on the Projectile 1 model. With a_2, the heat transfer coefficient is up to 6 times larger than the heat transfer coefficient for $a_1 = 5 \times 10^{-4}$. The surface temperature when using a_2 is up to 250 K lower than the surface temperature for a_1 in the first 30 seconds. The rapid cooling changes the time it takes the rind to form or the time it takes a pyroclast to reach the glass transition temperature by a factor of 2. For example, the average τ_{rind} for Projectile 1 is 28.00 seconds but with a_2 it is 15.73 seconds. The average τ_{Tg} for Projectile 1 is 129.01 seconds but with a_2 it is 64.89 seconds. The use of a_2 increased the average rind thickness by approximately 1 mm.

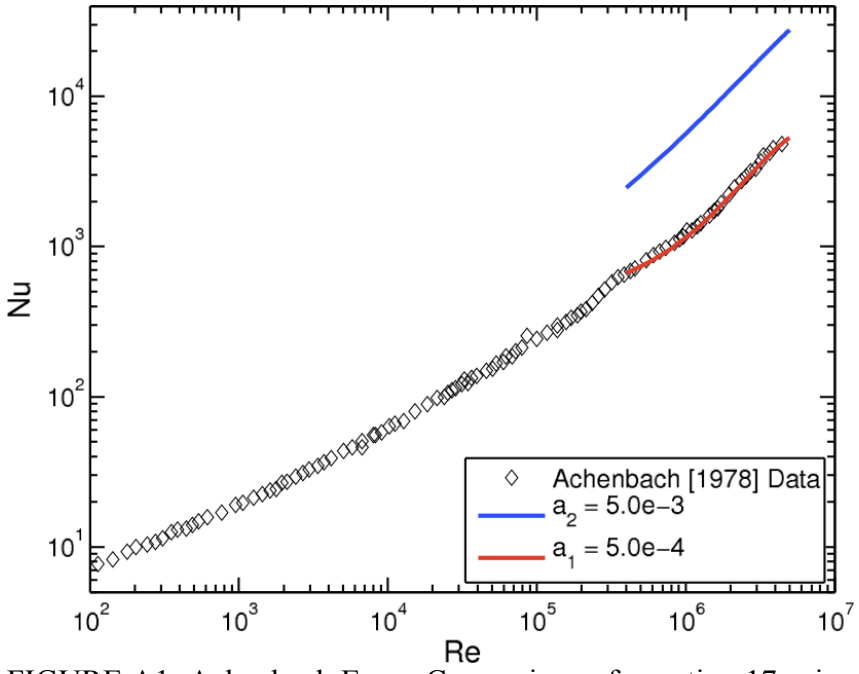

FIGURE A1: Achenbach Error. Comparison of equation 17 using a_2 = 5.0e-3 as reported in Achenbach (1978) and a_1 = 5.0e-4 with the replotted experimental data from *Achenbach* (1978).

APPENDIX B

WATER AND VISCOSITY AFFECT ON RIND

The decrease in rind thickness with increasing water concentration from the simulations is similar to the trend (Figure A2) of the ballistic breadcrust bombs at Guagua Pichincha. The breadcrust bombs at Pichincha have an increase in rind thickness that correlates to decreasing water content trapped in the glass of the rinds [*Wright et al.*, 2007]. The trends are not the exact same and the compositions are different so an exact comparison is not applicable. However, this illustrates the multiscale model produces similar trends in water concentration and rind thickness as volcanic deposits.

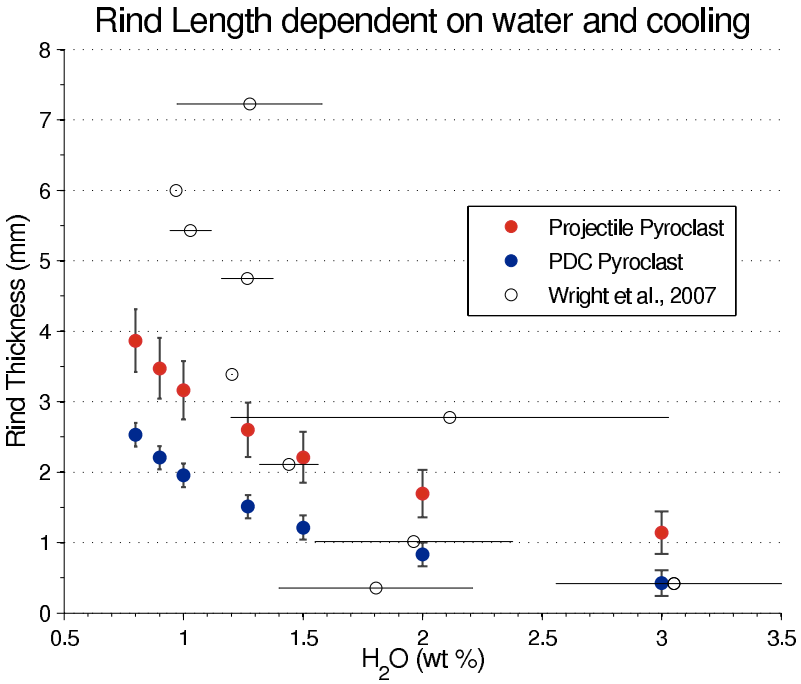

FIGURE A2: Water concentration affect on rind thickness. The figure shows the model produces a similar trend as breadcrust bombs from Wright et al. (2007) where rind thickness increases with decreasing dissolved water concentration.

Additionally, one hypothesis on the influence of breadcrust rind thickness is also the composition (i.e. viscosity) of the pyroclast. Shown here is a comparison of how

composition could affect rind thickness. Here the exact same transport path (PROJ 4) and dissolved water concentration of 1 wt% is used. Only the composition of the pyroclast is changed from andesite (TUNG-PS-48A) to dacite (GP6). See Table A1 (Appendix C) for compositions.

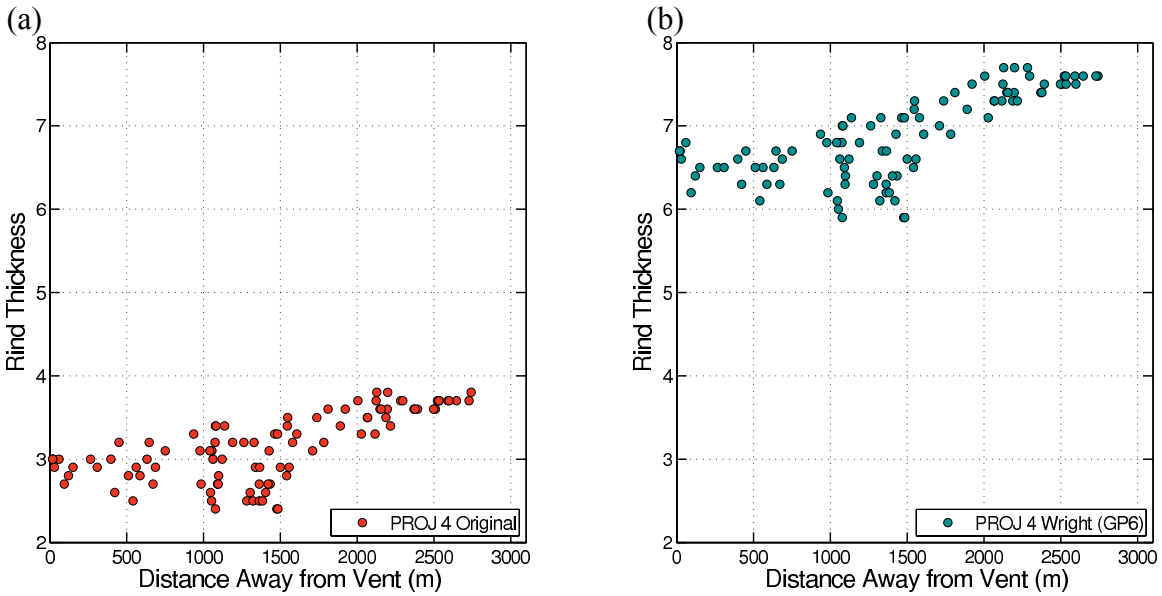

FIGURE A3: Compositional affect on modeled rind thickness. (a) Rind thickness for simulation PROJ 4 with TUNG-PS-48A (Appendix 3) composition and 1 wt% water. (b) Rind thickness for the same trajectory and thermal history (PROJ 4) but with GP6 (Appendix 3) composition. The higher silica content and thus higher viscosity creates a thicker rind.

APPENDIX C

WHOLE-ROCK MAJOR ELEMENTAL (WT%) COMPOSITIONS

TABLE A1: Whole-rock major elemental (wt%) compositions used in models

Sample Name	TUNG-PS-48A	GP6	TU10-06PJ
Sample Type	Scoriae Bomb	Breadcrust Bomb	Scoriae Bomb
Eruption Year	16 Ago 2006	1999	2006
SiO_2	58.2	64.11	58.45
TiO_2	0.88	0.389	0.91
Al_2O_3	16.75	16.78	16.7
FeO*	7.35[§]	4.83	6.76
MnO	0.11	0.084	0.11
MgO	4.2	2.35	4.31
CaO	6.85	5.35	6.85
Na_2O	3.92	4.18	3.91
K_2O	1.71	1.79	1.76
P_2O_5	0.24	0.13	0.25
	[*Samaniego et al.*, 2011]	[*Wright et al.*, 2007]	[*Myers et al.*, 2014]

[§]Fe_2O_3*

REFERENCES

Achenbach, E. (1978), Heat transfer from spheres up to Re = 6 x 10^6, *Proc Sixth Int Heat Transfer Conference*, *5*, 341–346.

Anderson, S. W., D. H. Krinsley, and J. H. Fink (1994), Criteria for recognition of constructional silicic lava flow surfaces, *Earth Surf. Process. Landforms*, *19*(6), 531–541.

Andrews, B. J. (2014), Dispersal and air entrainment in unconfined dilute pyroclastic density currents, *Bulletin of Volcanology*, *76*(9), 852, doi:10.1007/s00445-014-0852-4.

Andrews, B. J., and M. Manga (2011), Effects of topography on pyroclastic density current runout and formation of coignimbrites, *Geology*, doi:10.1130/G32226.1.

Andrews, B. J., and M. Manga (2012), Experimental study of turbulence, sedimentation, and coignimbrite mass partitioning in dilute pyroclastic density currents, *Journal of Volcanology and Geothermal Research*, doi:10.1016/j.jvolgeores.2012.02.011.

Bacon, C. R. (1977), High temperature heat content and heat capacity of silicate glasses: experimental determination and a model for calculation, *American Journal of Science*, *277*(2), 109–135.

Banks, N. G., and R. P. Hoblitt (1981), Summary of temperature studies of 1980 deposits, in *The 1980 Eruptions of Mount St. Helens, Washington*, edited by P. W. Lipman and D. R. Mullineaux, pp. 295–313, US Geol Surv Prof Paper 1250.

Barba, D., P. Samaniego, J.-L. Le Pennec, M. Hall, C. Robin, P. Mothes, H. Yepes, P. Ramon, S. Arellano, and G. Ruiz (2008), The 2006 eruptions of the Tungurahua volcano (Ecuador) and the importance of volcano hazard maps and their diffusion, *7th International Symposium on Andean Geodynamics*, 67–70.

Behrens, H., Y. Zhang, and Z. Xu (2004), H_2O diffusion in dacitic and andesitic melts, *Geochimica et Cosmochimica Acta*, *68*(24), 5139–5150, doi:10.1016/j.gca.2004.07.008.

Benage, M. C., J. Dufek, W. Degruyter, D. Geist, K. Harpp, and E. Rader (2014), Tying textures of breadcrust bombs to their transport regime and cooling history, *Journal of Volcanology and Geothermal Research*, *274*, 92–107, doi:10.1016/j.jvolgeores.2014.02.005.

Blower, J. D., H. M. Mader, and S. Wilson (2001), Coupling of viscous and diffusive controls on bubble growth during explosive volcanic eruptions, *Earth and Planetary Science Letters*, *193*(1), 47–56.

Blundy, J., and K. Cashman (2005), Rapid decompression-driven crystallization recorded by melt inclusions from Mount St. Helens volcano, *Geology*, *33*(10), 793–796,

doi:10.1130/G21668.1.

Bonnecaze, R. T., H. E. Huppert, and J. R. Lister (1993), Particle-driven gravity currents, *J. Fluid Mech.*, *250*, 339–339.

Brand, B. D., C. Mackaman-Lofland, N. M. Pollock, S. Bendaña, B. Dawson, and P. Wichgers (2014), Journal of Volcanology and Geothermal Research, *Journal of Volcanology and Geothermal Research*, *276*(C), 189–214, doi:10.1016/j.jvolgeores.2014.01.007.

Branney, M. J., and P. Kokelaar (1992), A reappraisal of ignimbrite emplacement: progressive aggradation and changes from particulate to non-particulate flow during emplacement of high-grade ignimbrite, *Bulletin of Volcanology*, *54*(6), 504–520.

Branney, M. J., and P. Kokelaar (1997), Giant bed from a sustained catastrophic density current flowing over topography: Acatlan ignimbrite, Mexico, *Geology*, *25*(2), 115–118.

Branney, M. J., and P. Kokelaar (2002), *Pyroclastic density currents and the sedimentation of ignimbrites*, Memoirs Geological Society, London. 143 pages.

Burgisser, A., and G. W. Bergantz (2002), Reconciling pyroclastic flow and surge: the multiphase physics of pyroclastic density currents, *Earth and Planetary Science Letters*, *202*(2), 405–418.

Burgisser, A., G. W. Bergantz, and R. E. Breidenthal (2005), Addressing complexity in laboratory experiments: the scaling of dilute multiphase flows in magmatic systems, *Journal of Volcanology and Geothermal Research*, *141*(3-4), 245–265, doi:10.1016/j.jvolgeores.2004.11.001.

Burgisser, A., S. Poussineau, L. Arbaret, T. H. Druitt, T. Giachetti, and J.-L. Bourdier (2010), Pre-explosive conduit conditions of the 1997 Vulcanian explosions at Soufrière Hills Volcano, Montserrat: I. Pressure and vesicularity distributions, *Journal of Volcanology and Geothermal Research*, *194*(1-3), 27–41, doi:10.1016/j.jvolgeores.2010.04.008.

Burnham, C. W. (1975), Water and magmas; a mixing model, *Geochimica et Cosmochimica Acta*, *39*(8), 1077–1084.

Bursik, M. I., and A. W. Woods (2000), The effects of topography on sedimentation from particle-laden turbulent density currents, *Journal of Sedimentary Research*, *70*, 53–63.

Bursik, M. I., and A. W. Woods (1996), The dynamics and thermodynamics of large ash flows, *Bulletin of Volcanology*, *58*(2-3), 175–193.

Calder, E. S., P. D. Cole, W. B. Dade, T. H. Druitt, R. P. Hoblitt, H. E. Huppert, L. Ritchie, R. Sparks, and S. R. Young (1999), Mobility of pyroclastic flows and surges

at the Soufriere Hills Volcano, Montserrat, *Geophys. Res. Lett.*, *26*(5), 537–540.

Calder, E. S., R. Sparks, and M. C. Gardeweg (2000), Erosion, transport and segregation of pumice and lithic clasts in pyroclastic flows inferred from ignimbrite at Lascar Volcano, Chile, *Journal of Volcanology and Geothermal Research*, *104*(1), 201–235.

Capaccioni, B., and F. Cuccoli (2005), Spatter and welded air fall deposits generated by fire-fountaining eruptions: Cooling of pyroclasts during transport and deposition, *Journal of Volcanology and Geothermal Research*, *145*(3-4), 263–280, doi:10.1016/j.jvolgeores.2005.02.001.

Carey, S., H. Sigurdsson, C. Mandeville, and S. Bronto (1996), Pyroclastic flows and surges over water: an example from the 1883 Krakatau eruption, *Bulletin of Volcanology*, *57*(7), 493–511.

Caricchi, L., L. Burlini, P. Ulmer, T. Gerya, M. Vassalli, and P. Papale (2007), Non-Newtonian rheology of crystal-bearing magmas and implications for magma ascent dynamics, *Earth and Planetary Science Letters*, *264*(3), 402–419.

Cashman, K. V. (1992), Groundmass crystallization of Mount St. Helens dacite, 1980–1986: a tool for interpreting shallow magmatic processes, *Contrib Mineral Petrol*, *109*(4), 431–449.

Cashman, K. V., and S. M. McConnell (2005), Multiple levels of magma storage during the 1980 summer eruptions of Mount St. Helens, WA, *Bulletin of Volcanology*, *68*(1), 57–75, doi:10.1007/s00445-005-0422-x.

Choux, C. M., and T. H. Druitt (2002), Analogue study of particle segregation in pyroclastic density currents, with implications for the emplacement mechanisms of large ignimbrites, *Sedimentology*, *49*(5), 907–928.

Cioni, R. (2004), Temperatures of the A.D. 79 pyroclastic density current deposits (Vesuvius, Italy), *Journal of Geophysical Research*, *109*(B2), B02207, doi:10.1029/2002JB002251.

Clarke, A. B., A. Neri, B. Voight, G. Macedonio, and T. H. Druitt (2002), Computational modelling of the transient dynamics of the August 1997 Vulcanian explosions at Soufriere Hills Volcano, Montserrat: influence of initial conduit conditions on near-vent pyroclastic dispersal, *Geological Society, London, Memoirs*, *21*(1), 319–348, doi:10.1144/GSL.MEM.2002.021.01.15.

Clauser, C., and E. Huenges (1995), Thermal conductivity of rocks and minerals, in *Rock Physics & Phase Relations: A Handbook of Physical Constants*, vol. 3, edited by T. J. Ahrens, pp. 105–126, American Geophysical Union, Washington, D.C.

Cole, P. D., E. S. Calder, R. Sparks, Clarke, AB, T. H. Druitt, S. R. Young, R. A. Herd, C. L. Harford, and G. E. Norton (2002), Deposits from dome-collapse and fountain-collapse pyroclastic flows at Soufrière Hills Volcano, Montserrat, *Geological*

Society, London, Memoirs, *21*(1), 231–262.

Dade, W. B. (2003), The emplacement of low-aspect ratio ignimbrites by turbulent parent flows, *Journal of Geophysical Research*, *108*(B4), 2211, doi:10.1029/2001JB001010.

Dade, W. B., and H. E. Huppert (1995a), Runout and fine‐sediment deposits of axisymmetric turbidity currents, *Journal of Geophysical Research*, *100*, 18597–18609.

Dade, W. B., and H. E. Huppert (1995b), A box model for non‐entraining, suspension‐driven gravity surges on horizontal surfaces, *Sedimentology*, *42*(3), 453–470.

Dade, W. B., J. R. Lister, and H. E. Huppert (1994), Fine-sediment deposition from gravity surges on uniform slopes, *Journal of Sedimentary Research*, *64*(3a), 423–432.

Dobran, F. (2001), *Volcanic Processes: Mechanisms in Material Transport*, Kluwer Academic/Plenum Publishers, Norwell, Mass.

Douillet, G. A. et al. (2013a), Sedimentology and geomorphology of the deposits from the August 2006 pyroclastic density currents at Tungurahua volcano, Ecuador, *Bulletin of Volcanology*, *75*(11), 765, doi:10.1007/s00445-013-0765-7.

Douillet, G. A., D. A. Pacheco, U. Kueppers, J. Letort, È. Tsang-Hin-Sun, J. Bustillos, M. Hall, P. Ramón, and D. B. Dingwell (2013b), Dune bedforms produced by dilute pyroclastic density currents from the August 2006 eruption of Tungurahua volcano, Ecuador, *Bulletin of Volcanology*, *75*(11), 762, doi:10.1007/s00445-013-0762-x.

Druitt, T. H. (1998), Pyroclastic density currents, *Geological Society, London, Special Publications*, *145*(1), 145–182.

Druitt, T. H., G. Avard, G. Bruni, P. Lettieri, and F. Maez (2007), Gas retention in fine-grained pyroclastic flow materials at high temperatures, *Bulletin of Volcanology*, *69*(8), 881–901, doi:10.1007/s00445-007-0116-7.

Dufek, J. (2016), The Fluid Mechanics of Pyroclastic Flows, *Annual Review of Fluid Mechanics*, *48*(1), null, doi:10.1146/annurev-fluid-122414-034252.

Dufek, J., and G. W. Bergantz (2007a), Suspended load and bed-load transport of particle-laden gravity currents: the role of particle–bed interaction, *Theoretical and Computational Fluid Dynamics*, *21*(2), 119–145, doi:10.1007/s00162-007-0041-6.

Dufek, J., and G. W. Bergantz (2007b), Dynamics and deposits generated by the Kos Plateau Tuff eruption: Controls of basal particle loss on pyroclastic flow transport, *Geochem. Geophys. Geosyst.*, *8*(12), doi:10.1029/2007GC001741.

Dufek, J., and M. Manga (2008), In situ production of ash in pyroclastic flows, *Journal of Geophysical Research: Solid Earth (1978–2012)*, *113*(B9), doi:10.1029/2007JB005555.

Dufek, J., C. Huber, and L. Karlstrom (2013), Magma chamber dynamics and thermodynamics, in *Modeling volcanic processes*, edited by S. A. Fagents, T. K. P. Gregg, and R. M. C. Lopes, pp. 5–31, Cambridge.

Dufek, J., J. Wexler, and M. Manga (2009), Transport capacity of pyroclastic density currents: Experiments and models of substrate‐flow interaction, *Journal of Geophysical Research: Solid Earth*, *114*(B11), doi:10.1029/2008JB006216.

Dufek, J., T. Esposti Ongaro, and O. Roche (2015), Pyroclastic Density Currents: Processes and Models, in *The encyclopedia of volcanoes*, edited by H. Sigurdsson, B. Houghton, S. McNutt, H. Rymer, and J. Stix, pp. 631–648, Elsevier.

Eckert, E. R. G., and R. M. Drake (1987), *Analysis of heat and mass transfer*, Hemisphere Pub. Corp, Washington.

Eichelberger, J. C., and F. G. Koch (1979), Lithic fragments in the Bandelier Tuff, Jemez Mountains, New Mexico, *Journal of Volcanology and Geothermal Research*, *5*(1), 115–134.

Ellison, T. H., and J. S. Turner (1959), Turbulent entrainment in stratified flows, *J. Fluid Mech.*, 423–448.

Esposti Ongaro, T., A. B. Clarke, A. Neri, B. Voight, and C. Widiwijayanti (2008), Fluid dynamics of the 1997 Boxing Day volcanic blast on Montserrat, West Indies, *Journal of Geophysical Research*, *113*(B3), B03211, doi:10.1029/2006JB004898.

Esposti Ongaro, T., A. B. Clarke, B. Voight, A. Neri, and C. Widiwijayanti (2012), Multiphase flow dynamics of pyroclastic density currents during the May 18, 1980 lateral blast of Mount St. Helens, *Journal of Geophysical Research*, *117*(B6), B06208, doi:10.1029/2011JB009081.

Estep, J., and J. Dufek (2012), Substrate effects from force chain dynamics in dense granular flows, *Journal of Geophysical Research*, *117*(F1), F01028, doi:10.1029/2011JF002125.

Fisher, R. V. (1966), Mechanism of deposition from pyroclastic flows, *American Journal of Science*, *264*, 350–363.

Fisher, R. V. (1983), Flow transformations in sediment gravity flows, *Geology*.

Fisher, R. V. (1979), Models for pyroclastic surges and pyroclastic flows, *Journal of Volcanology and Geothermal Research*, *6*(3), 305–318.

Forestier-Coste, L., S. Mancini, A. Burgisser, and F. James (2012), Numerical resolution of a mono-disperse model of bubble growth in magmas, *Applied Mathematical Modelling*, *36*(12), 5936–5951.

Freundt, A. (2003), Entrance of hot pyroclastic flows into the sea: experimental

observations, *Bulletin Volcanologique*, *65*(2-3), 144–164, doi:10.1007/s00445-002-0250-1.

Fujii, T., and S. Nakada (1999), The 15 September 1991 pyroclastic flows at Unzen Volcano (Japan): a flow model for associated ash-cloud surges, *Journal of Volcanology and Geothermal Research*.

Geschwind, C.-H., and M. J. Rutherford (1995), Crystallization of microlites during magma ascent: the fluid mechanics of 1980–1986 eruptions at Mount St Helens, *Bulletin of Volcanology*, *57*(5), 356–370.

Giachetti, T., T. Druitt, A. Burgisser, L. Arbaret, and C. Galven (2010), Bubble nucleation, growth and coalescence during the 1997 Vulcanian explosions of Soufrière Hills Volcano, Montserrat, *Journal of Volcanology and Geothermal Research*, *193*(3-4), 215–231, doi:10.1016/j.jvolgeores.2010.04.001.

Giordano, D., A. Nichols, and D. B. Dingwell (2005), Glass transition temperatures of natural hydrous melts: a relationship with shear viscosity and implications for the welding process, *Journal of Volcanology and Geothermal Research*, *142*(1), 105–118, doi:10.1016/j.jvolgeores.2004.10.015.

Giordano, D., J. K. Russell, and D. B. Dingwell (2008), Viscosity of magmatic liquids: a model, *Earth and Planetary Science Letters*, *271*(1), 123–134, doi:10.1016/j.epsl.2008.03.038.

Gottsmann, J., D. Giordano, and D. B. Dingwell (2002), Predicting shear viscosity during volcanic processes at the glass transition: a calorimetric calibration, *Earth and Planetary Science Letters*, *198*(3), 417–427.

Hall, M. L., A. L. Steele, P. A. Mothes, and M. C. Ruiz (2013), Pyroclastic density currents (PDC) of the 16–17 August 2006 eruptions of Tungurahua volcano, Ecuador: Geophysical registry and characteristics, *Journal of Volcanology and Geothermal Research*, *265*, 78–93, doi:10.1016/j.jvolgeores.2013.08.011.

Hall, M. L., C. Robin, B. Beate, P. Mothes, and M. Monzier (1999), Tungurahua Volcano, Ecuador: structure, eruptive history and hazards, *Journal of Volcanology and Geothermal Research*, *91*(1), 1–21.

Hall, M. L., P. Samaniego, J.-L. Le Pennec, and J. B. Johnson (2008), Ecuadorian Andes volcanism: A review of Late Pliocene to present activity, *Journal of Volcanology and Geothermal Research*, *176*(1), 1–6, doi:10.1016/j.jvolgeores.2008.06.012.

Hall, M., and P. Mothes (2008), The rhyolitic–andesitic eruptive history of Cotopaxi volcano, Ecuador, *Bulletin of Volcanology*, *70*(6), 675–702, doi:10.1007/s00445-007-0161-2.

Hallworth, M. A., H. E. Huppert, J. C. Phillips, and R. S. J. Sparks (1996), Entrainment into two-dimensional and axisymmetric turbulent gravity currents, *J. Fluid Mech.*,

308, 289–311.

Hallworth, M. A., J. C. Phillips, H. E. Huppert, and R. S. J. Sparks (1993), Entrainment in turbulent gravity currents, *Nature*, *362*(6423), 829–831.

Hammer, J. E., and M. J. Rutherford (2002), An experimental study of the kinetics of decompression‐induced crystallization in silicic melt, *Journal of Geophysical Research: Solid Earth (1978–2012)*, *107*(B1), ECV 8–1–ECV 8–24, doi:10.1029/2001JB000281.

Hammer, J. E., K. V. Cashman, and B. Voight (2000), Magmatic processes revealed by textural and compositional trends in Merapi dome lavas, *Journal of Volcanology and Geothermal Research*, *100*(1), 165–192.

Hoblitt, R. P., and R. S. Harmon (1993), Bimodal density distribution of cryptodome dacite from the 1980 eruption of Mount St. Helens, Washington, *Bulletin of Volcanology*, *55*(6), 421–437.

Hort, M., and J. Gardner (2000), Constraints on cooling and degassing of pumice during Plinian volcanic eruptions based on model calculations, *Journal of Geophysical Research*, *105*(B11), 25981–26001.

Houghton, B. F., and C. Wilson (1989), A vesicularity index for pyroclastic deposits, *Bulletin of Volcanology*, *51*(6), 451–462.

Huppert, H. E., and J. E. Simpson (1980), The slumping of gravity currents, *J. Fluid Mech.*, *99*(4), 785–799.

Hurwitz, S., and O. Navon (1994), Bubble nucleation in rhyolitic melts: Experiments at high pressure, temperature, and water content, *Earth and Planetary Science Letters*, *122*(3), 267–280.

Incropera, F. P., and D. P. DeWitt (1996), *Introduction to heat transfer*, 3rd ed., Wiley, New York.

Iverson, R. M., and J. W. Vallance (2001), New views of granular mass flows, *Geology*, *29*(2), 115–118.

Iverson, R. M., and R. P. Denlinger (2001), Flow of variably fluidized granular masses across three‐dimensional terrain: 1. Coulomb mixture theory, *Journal of Geophysical Research: Solid Earth (1978–2012)*, *106*(B1), 537–552.

Kaminski, É., and C. Jaupart (1997), Expansion and quenching of vesicular magma fragments in Plinian eruptions, *Journal of Geophysical Research*, *102*(B6), 12187–12203.

Kelfoun, K., P. Samaniego, P. Palacios, and D. Barba (2009), Testing the suitability of frictional behaviour for pyroclastic flow simulation by comparison with a well-

constrained eruption at Tungurahua volcano (Ecuador), *Bulletin of Volcanology*, *71*(9), 1057–1075, doi:10.1007/s00445-009-0286-6.

Koyaguchi, T. (2005), An analytical study for 1-dimensional steady flow in volcanic conduits, *Journal of Volcanology and Geothermal Research*, *143*(1-3), 29–52, doi:10.1016/j.jvolgeores.2004.09.009.

Lacroix, A. (1904), *La Montagne Pelée et ses éruptions*, Masson.

Le Pennec, J.-L., D. Jaya, P. Samaniego, P. Ramon, S. Moreno Yánez, J. Egred, and J. Van Der Plicht (2008), The AD 1300–1700 eruptive periods at Tungurahua volcano, Ecuador, revealed by historical narratives, stratigraphy and radiocarbon dating, *Journal of Volcanology and Geothermal Research*, *176*(1), 70–81, doi:10.1016/j.jvolgeores.2008.05.019.

Llewellin, E. W., and M. Manga (2005), Bubble suspension rheology and implications for conduit flow, *Journal of Volcanology and Geothermal Research*, *143*(1-3), 205–217, doi:10.1016/j.jvolgeores.2004.09.018.

Lun, C., S. B. Savage, D. J. Jeffrey, and N. Chepurniy (1984), Kinetic theories for granular flow: inelastic particles in Couette flow and slightly inelastic particles in a general flow field, *J. Fluid Mech.*, *140*, 223–256.

Mandeville, C. W., S. Carey, H. Sigurdsson, and J. King (1994), Paleomagnetic evidence for high‐temperature emplacement of the 1883 subaqueous pyroclastic flows from Krakatau Volcano, Indonesia, *Journal of Geophysical Research: Solid Earth (1978–2012)*, *99*(B5), 9487–9504.

Marti, J., J. L. Diez Gil, and R. Ortiz (1991), Conduction model for the thermal influence of lithic clasts in mixtures of hot gases and ejecta, *Journal of Geophysical Research*, *96*(B13), 21879–21885.

Maxey, M. R., and J. J. Riley (1983), Equation of motion for a small rigid sphere in a nonuniform flow, *Physics of Fluids*, *26*, 883–889, doi:10.1063/1.864230.

Moore, J. G., and W. G. Melson (1969), Nuees ardentes of the 1968 eruption of Mayon volcano, Philippines, *Bulletin Volcanologique*, *33*(2), 600–620.

Morrissey, M. M., and L. G. Mastin (2000), Vulcanian Eruptions, in *Encyclopedia of Volcanoes*, edited by H. Sigurdsson, pp. 463–475, Academic Press, San Diego.

Morton, B. R., G. Taylor, and J. S. Turner (1956), Turbulent Gravitational Convection from Maintained and Instantaneous Sources, *Proceedings of the Royal Society A: Mathematical, Physical and Engineering Sciences*, *234*(1196), 1–23, doi:10.1098/rspa.1956.0011.

Myers, M. L., D. J. Geist, M. C. Rowe, K. S. Harpp, P. J. Wallace, and J. Dufek (2014), Replenishment of volatile-rich mafic magma into a degassed chamber drives mixing

and eruption of Tungurahua volcano, *Bulletin of Volcanology*, *76*(11), 872, doi:10.1007/s00445-014-0872-0.

Neri, A., and G. Macedonio (1996), Numerical simulation of collapsing volcanic columns with particles of two sizes, *Journal of Geophysical Research: Solid Earth*, *101*(B4), 8153–8174.

Neri, A., T. E. Ongaro, G. Macedonio, and D. Gidaspow (2003), Multiparticle simulation of collapsing volcanic columns and pyroclastic flow, *Journal of Geophysical Research*, *108*(B4), 2202, doi:10.1029/2001JB000508.

Neri, A., T. E. Ongaro, G. Menconi, M. D. Vitturi, C. Cavazzoni, G. Erbacci, and P. J. Baxter (2007), 4D simulation of explosive eruption dynamics at Vesuvius, *Geophys. Res. Lett.*, *34*(4), L04309, doi:10.1029/2006GL028597.

Patankar, S. V. (1980), *Numerical heat transfer and fluid flow*, Hemisphere Pub. Corp, Washington.

Patrick, M. R. (2007), Dynamics of Strombolian ash plumes from thermal video: Motion, morphology, and air entrainment, *Journal of Geophysical Research*, *112*(B6), B06202, doi:10.1029/2006JB004387.

Peterson, D. W. (1988), Volcanic hazards and public response, *Journal of Geophysical Research: Solid Earth*, *93*, 4161–4170.

Pistolesi, M., M. Rosi, R. Cioni, K. V. Cashman, A. Rossotti, and E. Aguilera (2011), Physical volcanology of the post–twelfth-century activity at Cotopaxi volcano, Ecuador: Behavior of an andesitic central volcano, *Geological Society of America Bulletin*, *123*(5-6), 1193–1215, doi:10.1130/B30301.1.

Plourde, F., M. V. Pham, S. D. Kim, and S. Balachandar (2008), Direct numerical simulations of a rapidly expanding thermal plume: structure and entrainment interaction, *J. Fluid Mech.*, *604*, 99–123, doi:10.1017/S0022112008001006.

Pollock, N., K. S. Harpp, D. Geist, J. Dufek, and P. A. Mothes (2010), Vegetation damage as a proxy for physical characteristics of PDCs, *AGU Fall Meeting Abstracts*, *1*, 2337.

Prousevitch, A. A., D. L. Sahagian, and A. T. Anderson (1993), Dynamics of diffusive bubble growth in magmas: Isothermal case, *Journal of Geophysical Research*, *98*(B12), 22283–22307.

Proussevitch, A. A., and D. L. Sahagian (1996), Dynamics of coupled diffusive and decompressive bubble growth in magmatic systems, *Journal of Geophysical Research*, *101*(B8), 17447–17455.

Rader, E., D. Geist, J. W. Geissman, J. Dufek, and K. Harpp (2015), Hot clasts and cold blasts: thermal heterogeneity in boiling-over pyroclastic density currents, *Geological*

Society, London, Special Publications, *396*(1), 67–86, doi:10.1144/SP396.16.

Raju, N., and E. Meiburg (1995), The accumulation and dispersion of heavy particles in forced two-dimensional mixing layers. Part 2: The effect of gravity, *Physics of Fluids*, *7*(6), 1241–1264, doi:10.1063/1.868581.

Roche, O. (2004), Experimental study of gas-fluidized granular flows with implications for pyroclastic flow emplacement, *Journal of Geophysical Research*, *109*(B10), B10201, doi:10.1029/2003JB002916.

Roche, O. (2012), Depositional processes and gas pore pressure in pyroclastic flows: an experimental perspective, *Bulletin of Volcanology*, *74*(8), 1807–1820, doi:10.1007/s00445-012-0639-4.

Roche, O., S. Montserrat, Y. Niño, and A. Tamburrino (2010), Pore fluid pressure and internal kinematics of gravitational laboratory air‐particle flows: Insights into the emplacement dynamics of pyroclastic flows, *Journal of Geophysical Research: Solid Earth*, *115*(B9), 1–18, doi:10.1029/2009JB007133.

Roche, O., T. H. Druitt, and R. Cas (2001), Experimental aqueous fluidization of ignimbrite, *Journal of Volcanology and Geothermal Research*, *112*(1), 267–280.

Roperch, P., A. Chauvin, J.-L. Le Pennec, and L. E. Lara (2014), Physics of the Earth and Planetary Interiors, *Physics of the Earth and Planetary Interiors*, *227*(C), 20–29, doi:10.1016/j.pepi.2013.11.008.

Saffaraval, F., S. A. Solovitz, D. E. Ogden, and L. G. Mastin (2012), Impact of reduced near-field entrainment of overpressured volcanic jets on plume development, *Journal of Geophysical Research*, *117*(B5), B05209, doi:10.1029/2011JB008862.

Samaniego, P., J.-L. Le Pennec, C. Robin, and S. Hidalgo (2011), Petrological analysis of the pre-eruptive magmatic process prior to the 2006 explosive eruptions at Tungurahua volcano (Ecuador), *Journal of Volcanology and Geothermal Research*, *199*(1-2), 69–84, doi:10.1016/j.jvolgeores.2010.10.010.

Savage, S. B. (1998), Analyses of slow high-concentration flows of granular materials, *J. Fluid Mech.*, *377*, 1–26.

Schneider, C. A., W. S. Rasband, and K. W. Eliceiri (2012), NIH Image to ImageJ: 25 years of image analysis, *Nature Methods*, *9*(7), 671–675, doi:10.1038/nmeth.2089.

Scott, A. C., and I. J. Glasspool (2005), Charcoal reflectance as a proxy for the emplacement temperature of pyroclastic flow deposits, *Geology*, *33*(7), 589, doi:10.1130/G21474.1.

Scott, A. C., R. S. J. Sparks, I. D. Bull, H. Knicker, and R. P. Evershed (2008), Temperature proxy data and their significance for the understanding of pyroclastic density currents, *Geology*, *36*(2), 143–146, doi:10.1130/G24439A.1.

Sigurdsson, H., B. Houghton, H. Rymer, J. Stix, and S. McNutt (1999), Encyclopedia of volcanoes,

Simpson, J. E., and R. E. Britter (1979), The dynamics of the head of a gravity current advancing over a horizontal surface, *J. Fluid Mech.*, *94*(03), 477–495.

Sparks, R. (1978), The dynamics of bubble formation and growth in magmas: a review and analysis, *Journal of Volcanology and Geothermal Research*, *3*(1), 1–37.

Sparks, R. (1986), The dimensions and dynamics of volcanic eruption columns, *Bulletin of Volcanology*, *48*(1), 3–15.

Sparks, R. S. J. (1976), Grain size variations in ignimbrites and implications for the transport of pyroclastic flows, *Sedimentology*, *23*(2), 147–188.

Steffke, A. M., D. Fee, M. Garces, and A. Harris (2010), Eruption chronologies, plume heights and eruption styles at Tungurahua Volcano: Integrating remote sensing techniques and infrasound, *Journal of Volcanology and Geothermal Research*, *193*(3-4), 143–160, doi:10.1016/j.jvolgeores.2010.03.004.

Stroberg, T. W., M. Manga, and J. Dufek (2010), Heat transfer coefficients of natural volcanic clasts, *Journal of Volcanology and Geothermal Research*, *194*(4), 214–219, doi:10.1016/j.jvolgeores.2010.05.007.

Suzuki, Y. J. (2005), A numerical study of turbulent mixing in eruption clouds using a three-dimensional fluid dynamics model, *Journal of Geophysical Research*, *110*(B8), B08201, doi:10.1029/2004JB003460.

Suzuki, Y. J., and T. Koyaguchi (2009), A three-dimensional numerical simulation of spreading umbrella clouds, *Journal of Geophysical Research*, *114*(B3), B03209, doi:10.1029/2007JB005369.

Suzuki, Y. J., and T. Koyaguchi (2010), Numerical determination of the efficiency of entrainment in volcanic eruption columns, *Geophys. Res. Lett.*, *37*(5), doi:10.1029/2009GL042159.

Syamlal, M., W. Rogers, and T. J. O'Brien (1993), MFIX documentation: Theory guide, *Technical Note, DOE/METC-94/1004, NTIS/DE94000087, National Technical Information Service, Springfield, VA*.

Tait, S., R. Thomas, J. Gardner, and C. Jaupart (1998), Constraints on cooling rates and permeabilities of pumice in an explosive eruption jet from colour and magnetic mineralogy, *Journal of Volcanology and Geothermal Research*, *86*(1), 79–91.

Tanguy, J. C., C. Ribière, A. Scarth, and W. S. Tjetjep (1998), Victims from volcanic eruptions: a revised database, *Bulletin of Volcanology*, *60*, 137–144.

Thomas, R., and R. Sparks (1992), Cooling of tephra during fallout from eruption

columns, *Bulletin of Volcanology*, *54*(7), 542–553.

Turner, J. S. (1986), Turbulent entrainment: the development of the entrainment assumption, and its application to geophysical flows, *J. Fluid Mech.*, *173*, 431–471.

Valentine, G. A. (1987), Stratified flow in pyroclastic surges, *Bulletin of Volcanology*, *49*(4), 616–630.

Valentine, G. A., and K. H. Wohletz (1989), Numerical models of Plinian eruption columns and pyroclastic flows, *Journal of Geophysical Research: Solid Earth (1978–2012)*, *94*(B2), 1867–1887.

Van Bemmelen, R. W. (1949), Report on the volcanic activity and volcanological research in Indonesia during the period 1936–1948, *Bulletin of Volcanology*.

Vanderkluysen, L., A. J. L. Harris, K. Kelfoun, C. Bonadonna, and M. Ripepe (2012), Bombs behaving badly: unexpected trajectories and cooling of volcanic projectiles, *Bulletin of Volcanology*, *74*(8), 1849–1858, doi:10.1007/s00445-012-0635-8.

Walker, D., and O. Mullins Jr (1981), Surface tension of natural silicate melts from 1,200–1,500 C and implications for melt structure, *Contrib Mineral Petrol*, *76*(4), 455–462.

Walker, G. (1969), The breaking of magma, *Geological Magazine*, *106*(2), 166–173.

Walker, G. (1982), Eruptions of andesitic volcanoes, in *Andesites: orogenic andesites and related rocks*, edited by R. S. Thorpe, pp. 403–413, Wiley, New York.

Wells, M., C. Cenedese, and C. P. Caulfield (2010), The Relationship between Flux Coefficient and Entrainment Ratio in Density Currents, *J. Phys. Oceanogr.*, *40*(12), 2713–2727, doi:10.1175/2010JPO4225.1.

Whittington, A. G., A. M. Hofmeister, and P. I. Nabelek (2009), Temperature-dependent thermal diffusivity of the Earth's crust and implications for magmatism, *Nature*, *458*(7236), 319–321, doi:10.1038/nature07818.

Wilson, C. (1984), The role of fluidization in the emplacement of pyroclastic flows, 2: experimental results and their interpretation, *Journal of Volcanology and Geothermal Research*, *20*, 55–84.

Wilson, C., and B. F. Houghton (2000), Pyroclast Transport and Deposition, in *Encyclopedia of Volcanoes*, edited by H. Sigurdsson, pp. 545–554, Academic Press, San Diego.

Wohletz, K. H., and M. F. Sheridan (1979), A model of pyroclastic surge, *Geological Society of America Special Paper*, *180*, 177–194.

Wright, H. M. N., C. B. Folkes, R. A. F. Cas, and K. V. Cashman (2011), Heterogeneous

pumice populations in the 2.08-Ma Cerro Galán Ignimbrite: implications for magma recharge and ascent preceding a large-volume silicic eruption, *Bulletin of Volcanology*, *73*(10), 1513–1533, doi:10.1007/s00445-011-0525-5.

Wright, H. M. N., K. V. Cashman, M. Rosi, and R. Cioni (2007), Breadcrust bombs as indicators of Vulcanian eruption dynamics at Guagua Pichincha volcano, Ecuador, *Bulletin of Volcanology*, *69*, 281–300, doi:10.1007/s00445-006-0073-6.

Zheng, G., and R. List (1996), Convective heat transfer of rotating spheres and spheroids with non-uniform surface temperatures, *International Journal of Heat and Mass Transfer*, *39*(9), 1815–1826.